THE PENNSYLVANIA STATE UNIVERSITY

THE GRADUATE SCHOOL

COLLEGE OF THE LIBERAL ARTS

THE INFLUENCE OF ANGIOGENESIS ON CRANIOFACIAL DEVELOPMENT AND EVOLUTION

A DISSERTATION IN

ANTHROPOLOGY

BY

CHRISTOPHER J. PERCIVAL

SUBMITTED IN PARTIAL FULFILLMENT
OF THE REQUIREMENTS
FOR THE DEGREE OF

DOCTOR OF PHILOSOPHY

MAY 2013

The dissertation of Christopher J. Percival was reviewed and approved* by the following:

Joan T. Richtsmeier
Professor of Anthropology
Dissertation Advisor
Chair of Committee

Kenneth M. Weiss
Evan Pugh Professor of Anthropology and Genetics
and Science, Technology, and Society

Timothy M. Ryan
Assistant Professor of Anthropology, Geosciences,
and Information Sciences and Technology

Patrick J. Drew
Assistant Professor of Engineering Science
and Mechanics and Neurosurgery

Kazuhiko Kawasaki
Research Associate in Anthropology

George Milner
Professor of Anthropology
Head of the Department of Anthropology

*Signatures are on file in the Graduate School

ABSTRACT

Studies of the developmental bases of phenotypic variation are critical for a deep understanding of the evolutionary origins of traits that define the primate clade and the human lineage. This work focuses on the poorly studied role that blood-vessel branching and growth (angiogenesis) plays during craniofacial bone formation and mineralization (osteogenesis). We hypothesized that angiogenesis dysregulation can produce evolutionarily relevant variation of the craniofacial complex. Measurements of bone volume and relative density, derived from high resolution computed tomography images of an *Fgfr2*$^{+/P253R}$ mouse model of Apert syndrome, defined the "normal" pattern of craniofacial bone growth and maturation across the late embryonic period and suggested several hypotheses about the cellular basis of skeletal dysmorphology associated with the *Fgfr2* P253R mutation. 3D images of blood vessels and other soft tissue layers associated with the initial intramembranous mineralization of the frontal bone of these mice were generated with a hybrid optical coherence tomography and photoacoustic microscopy system in order to investigate the relationship between invading blood vessels and mineralizing bone. Although the resulting images did not resolve microvasculature or mineralizing frontal bone as we had expected, the results of this work provide the foundation for future studies and suggest that the *Fgfr2* P253R mutation may reduce the length of large superficial embryonic blood vessels of the head. Finally, the craniofacial skeletal phenotypes of mice that conditionally express this mutation in endothelial cells were quantified in order to determine if endothelial expression is associated with the craniofacial dysmorphology noted in the *Fgfr2*$^{+/P253R}$ mice. A combination of landmark based and volume/relative density based analyses suggested that endothelial expression of the mutation is associated with overall reduced scale of the skull. We hypothesized that this reduction is based on reduced endothelial sprouting during the angiogenesis associated with initial mineralization of craniofacial bones. In total, this work introduces refined methods to quantify important phenotypic aspects of the craniofacial complex and provides evidence that dysregulation of angiogenesis can serve as the indirect basis of craniofacial skeletal dysmorphology. This, in turn, suggests the importance of angiogenesis regulation in producing evolutionarily relevant skeletal variation found in our evolutionary past.

TABLE OF CONTENTS

LIST OF FIGURES

LIST OF TABLES

ACKNOWLEDGEMENTS

I owe thanks to all the people that helped me grow as a researcher and who collaborated with me to complete the research projects described in this dissertation. In particular, I owe a great debt to my graduate advisor, Joan Richtsmeier, who has been incredibly supportive, generous, and thoughtful throughout my graduate career. I am also grateful for the advice, support, and time provided by all of my committee members. I have learned a lot from each of you and I'm honored that you have agreed to serve on my dissertation committee. Sorry for the long dissertation, I swear that it's mostly figures.

I have been incredibly lucky to be a part of the Anthropology Department at Penn State, because of its congenial atmosphere, spirit of collaboration, and faculty support. In particular, each member of the Richtsmeier Lab have been excellent colleaques, collaborators, and friends throughout my tenure in the lab. The influence and work of several members of the lab can be seen in the research contained in this dissertation. This is especially true of Tiffany Kim, who managed our mouse colony, and Talia Pankratz, who completed a significant portion of the semiautomatic segmentation of the *Fgfr2*$^{+/P253R}$ mice and littermates, as well as the manual segmentation of the teeth of the Tek-cre crosses.

I first became aware of the idea that angiogenesis might significantly influence craniofacial bone variation when it was mentioned by Alan Walker during a "hominid research group meeting" in the Mook Room. Further inspiration for my pursuit of a connection between angiogenesis and osteogenesis stemmed from conversations with other attendees of these meetings including, but not limited to, Ken Weiss, Anne Buchanan, Brian Lambert, Kazuhiko Kawasaki, Alan Walker, Nina Jablonski, Tim Ryan, and Joan Richtsmeier. Thanks to all of you for including graduate students in these types of meetings and for allowing me to run with this research idea.

I have had the good fortune to collaborate with great researchers on campus and elsewhere. Many thanks to Tim Ryan and Tim Stecko at PSU CQI for the technical expertise and care in producing the computed tomography images used in my research. I appreciate your patience, as I can be very picky about the quality of my images. I owe thanks to Runze Li and Yuan Huang of the PSU Statistics Department, who have provided indespensible assistance in developing and executing multivariate functional regression analysis of bone density curves. I also owe a debt to Lihong Wang, Amy Winkler, and everyone else at the Optical Imaging Lab at Washinton University in St. Louis for collaborating with me and allowing the use of your facilities for my research. Finally, this research would not have been possible without the kind donation of Apert mouse model specimens by Ethylin Wang Jabs at the Mount Sinai School of Medicine to Joan Richtsmeier.

This work was supported in part by grants from the National Science Foundation to Christopher J. Percvial (BCS-1061554), to the Genomics of Craniofacial Biology Consortium (BCS-0725227), and from the National Institute of Dental and Craniofacial Research and the American Recovery and Reinvestment act to Joan T. Richtsmeier (R01DE018500; 3R01DE018500-02S1; R01DE022988). The image within Fig 1.5 was reproduced with kind permission of Springer Science+Business Media (p.65, Brookes and Revell, 1998).

CHAPTER 1:
REVIEW OF ANGIOGENESIS AND INTRAMEMBRANOUS SKELETOGENESIS

INTRODUCTION

The craniofacial skeleton reflects many important evolutionary trends of primates, including derived orbit morphology (Ross, 1995; Ravosa et al., 2000), cranial base shape (Lieberman et al., 2000), and increased relative cranial vault size (Isler et al., 2008). Differences in dentition (Lambert et al., 2004) and the morphology of the semicircular canal system (Spoor et al., 2007), respectively, provide evidence of diet and locomotion, while the degree of sexual dimorphism provides hints about social behavior (Plavcan, 2001). In particular, the human skull is highly derived in many unique ways and cranial elements are useful for determining phylogenetic relationships among hominids (Lahr, 1996; Schwartz and Tattersall, 2003). The skull houses many important functions associated with the human condition, including cognition (Falk, 1992; Holloway, 1969; Sherwood et al., 2008), vocalization (Kay et al., 1998; MacLarnon and Hewitt, 1999), and thermoregulation (Beals et al., 1984; Weaver, 2009), making questions about craniofacial evolution particularly intriguing (Lieberman, 2008). Morphology of the cranial vault, including cranial volume and relative neurocranial height are important characters that help to distinguish different primate clades (Fleagle et al., 2010). Vault morphology is recognized as an important diagnostic feature in operational definitions of Pleistocene hominid species and descriptions of new fossils (Athreya, 2009).

Developmental analysis of fossil and extant primates allows anthropologists to explore the developmental bases of morphological variation, the functional implications of derived morphology,

and subsequent evolutionary patterns (Lieberman et al., 2002; Lovejoy et al., 2003; Zollikofer and Ponce de León, 2010). Since Stephen J. Gould's discussion of ontogeny and phylogeny (Gould, 1977), ontogenetic shifts have been used to explain morphological differences between modern humans and other hominid species including chimpanzees (Leigh, 2004; Robson and Wood, 2008), *Ardipithecus ramidus* (Suwa et al., 2009), *Homo erectus* (Dean et al., 2001; Smith, 2004), and Neanderthals (Tillier, 1995; Ponce de León and Zollikofer, 2001); often using postnatal morphological data.

Morphological integration (Olson and Miller, 1958), measured as covariation between traits, occurs when traits share functional, evolutionary, and/or developmental bases (Klingenberg, 2008). Using this relationship, evolution can be modeled as the changes in the developmental units that make up a particular morphological unit or the developmental relationships between morphological units (Cheverud, 1995; Cheverud, 1996). Recent studies of integration have served to highlight potential developmental relationships that serve as the basis of evolutionary changes in vault size, midfacial prognathism, and cranial base angle among human ancestors (Aiello and Dean, 2002; Ross and Ravosa, 1993; Richtsmeier et al., 2006; Hallgrímsson and Lieberman, 2008; Lieberman et al., 2008; Mitteroecker et al., 2008; Martínez-Abadías et al., 2009). For instance, increases in relative brain size have been associated with increased flexion of the cranial base (Hallgrímsson and Lieberman, 2008; Lieberman et al., 2008), providing broad support for the hypothesis that differences in cranial base angle between modern humans and earlier hominids reflects an accommodation of increased brain volume and may be related to midfacial retraction.

While studies of postnatal craniofacial development are important, studies of prenatal developmental mechanisms are necessary to elucidate the developmental bases of many important craniofacial features. Diagnostic differences in craniofacial morphology exist between hominids (Cobb and O'Higgins, 2004) including modern humans and Neanderthals (Ponce de León and Zollikofer,

2001) during the earliest postnatal years and are likely to arise during prenatal development. The early appearance of taxon specific features has also been demonstrated in other studies (Lieberman et al., 2008; Richtsmeier and Walker, 1993; Krovitz, 2000), highlighting the importance of prenatal development in producing important craniofacial variation. Diagnostic human craniofacial features, including cranial base angle are known to develop prenatally (Jeffery and Spoor, 2002; Lieberman et al., 2008) and fetal growth patterns of macaques and humans are significantly different (Zumpano and Richtsmeier, 2003). The prenatal appearance of diagnostic morphology should not be surprising given that phenotypic novelties are often found to result from changes in gene regulation during the earliest stages of development (Raff, 1996; Hall, 1999; Carroll et al., 2001; Hall, 2003). Although studies of prenatal specimens are necessary to identify the developmental mechanisms responsible for many evolutionarily relevant craniofacial traits, primate fetal specimens are rare and relatively difficult to study. Studies utilizing other animal models provide an excellent alternative for anthropologists (Reno et al., 2008; Serrat et al., 2008; Menegaz et al., 2010; Carmody et al., 2011; Young and Devlin, 2012), because of the high degree of conservation of developmental processes across mammalian taxa (Reeves et al., 2001) and because samples of any fetal age can be analyzed.

In addition, the use of animal models in laboratory environments allows for the degree of control necessary to investigate the role of specific developmental pathways in producing craniofacial variation. Animal models can illuminate the genetic networks and developmental pathways that may have been modified to produce known evolutionary changes found in the fossil record. The palimpsest concept, first introduced by Gregory (Gregory, 1947), and now being championed by Hallgrímsson and colleagues (Hallgrímsson et al., 2009) provides a conceptual framework within which studies of the developmental determinants of variation in complex traits can be placed. In highly complex structures like the skull, it is probable that developmental processes underlying variation are sufficiently

complex that it is not possible to divide the structure into definitive morphological modules (Roseman et al., 2009). Instead, the palimpsest model suggests that we focus on how the combination of semi-independent developmental processes acting at different times and on different anatomical regions lead to patterns of variation and covariation in the adult structure (Hallgrímsson et al., 2009). One possible way to accomplish this is to focus on the spatial associations and developmental interactions between cell populations or tissues that are traditionally studied independently (Chapter 3). Another strategy is to modify gene expression and/or a developmental process associated with a specific tissue (or cell population) in order to see what secondary phenotypic effects occur across the head (Chapter 4). Both strategies are designed to measure how modifications in particular developmental pathways, such as blood vessel growth, brain growth, cell condensation, or ossification, produce phenotypic variation in the skull.

The purpose of the research described in this dissertation is to illuminate the association of craniofacial bone phenotypes with blood vessel branching and growth (angiogenesis), as well as to investigate how modifications to angiogenesis influence the development of craniofacial bone size, shape, and relative density. By focusing on how perturbations in the development of a specific tissue (e.g. vascular) are associated with phenotypic variation across the skull, these studies shed light on fundamental relationships between two developing tissues. The combination of this and similar studies will allow researchers to make more precise and testable hypotheses about the basis of novel evolutionarily relevant variation that serves as the basis of evolutionary change in the human lineage and others.

Most facial and cranial vault bones form intramembranously by ossifying directly from condensations of mesenchymal precursor cells, while most bones of the cranial base form endochondrally through the ossification of cartilaginous precursors. Studies of the mechanisms

of bone formation have primarily focused on endochondral ossification, leaving intramembranous ossification, particularly of craniofacial bones, poorly understood (Abzhanov et al., 2007; Karaplis, 2008). Although it is clear that angiogenesis and osteogenesis are tightly coupled in both intramembranous and endochondral bone formation (Marks and Odgren, 2002), further research on the specific process of angiogenesis and its association with early intramembranous bone formation is needed to provide currently unknown fundamental information about a process thought to be critical to craniofacial ossification. The current state of knowledge on initial intramembranous bone formation and ossification, with a focus on the association with angiogenesis, is reviewed in this chapter. Throughout the paper, the word skeletogenesis is used to refer to the process of the initial ossification and growth of an ossified skeletal element, while the word osteogenesis is used more generally to refer to the formation of new ossified material within a bone.

BONE CONDENSATIONS

Condensations of mesenchymal cells, which serve as the basis of vertebrate skeletal morphogenesis, form through cell migration towards a center and cell proliferation at that center (Hall and Miyake, 1992; Hall and Miyake, 2000). Mesenchyme is a loose connective tissue composed of multipotent cells, potentially from a variety of tissue layer origins and with varying differentiation potential (Aubin, 2008), and a loose matrix. Signals from the epithelium initiate formation of dense condensations of mesenchymal stem cells (Hall, 1988) and later play a role in initiating mesenchymal cell differentiation (Hall, 1992).

Skeletal mesenchymal condensations of the mouse associated with the frontonasal process and the first four pharyngeal arches are derived from cells that originate at the dorsal aspect of the neural tube as cells of the neuroectoderm. These cephalic neural crest cells transition into mesenchymal cells and migrate along specific paths to particular craniofacial locations (Le Lièvre and Le Douarin,

1975; Cordero et al., 2011). Cell staining in mice suggests that mesodermally derived endothelial cells invade newly formed populations of neural crest derived mesenchymal cells found throughout the developing face, becoming the only mesodermally derived cells located centrally within them (Yoshida et al., 2008). It has been suggested that signals from these endothelial cells might help to direct the migration of neural crest cells (Dietrich and Antoniades, 2012), although signaling from other tissues, including ectoderm (Tavares et al., 2012), are known to be important (reviewed by Bronner, 2012). Cells from neural crest derived mesenchymal populations contribute to the formation of all facial bones, the squamous temporal, the jugal, and the frontal bone (Fig 1.1) in mouse and presumably in all mammals. Mesenchymal cells derived from paraxial mesoderm provide the basis for the other vault elements and the bones of the cranial base (Fig 1.1) (Jiang et al., 2002; Noden and Trainor, 2005; McBratney-Owen et al., 2008; Yoshida et al., 2008). Associated with the borders of multiple ossification centers (Koyabu et al., 2012), the central portion of the interparietal is derived from neural crest cells (Yoshida et al., 2008). The sphenoid may either be derived from neural crest cells (McBratney-Owen et al., 2008) or mesodermal cells (Noden and Trainor, 2005).

A minimum number of cells (cell density) is necessary before differentiation of prechondrogenic condensations can occur (Ahrens et al., 1977; Solursh et al., 1978). Reaching the appropriate size earlier or increased pressure on the region of a condensation can lead to premature differentiation of the mesenchymal stem cells within it, while failure to reach an appropriate condensation size can prevent skeletogenesis (Hall and Miyake, 1992). The shape of a long bone's prechondrogenic condensation resembles the shape of its fully differentiated cartilage model, which establishes the basic initial shape for an endochondrally ossified bone (Caplan et al., 1983; Colnot et al., 2004). While associated muscles, tendons, and other skeletal elements are required for completely normal mouse limb bone morphogenesis, the rough shape of *ex vivo* embryonic bone anlages remain conserved for a few days

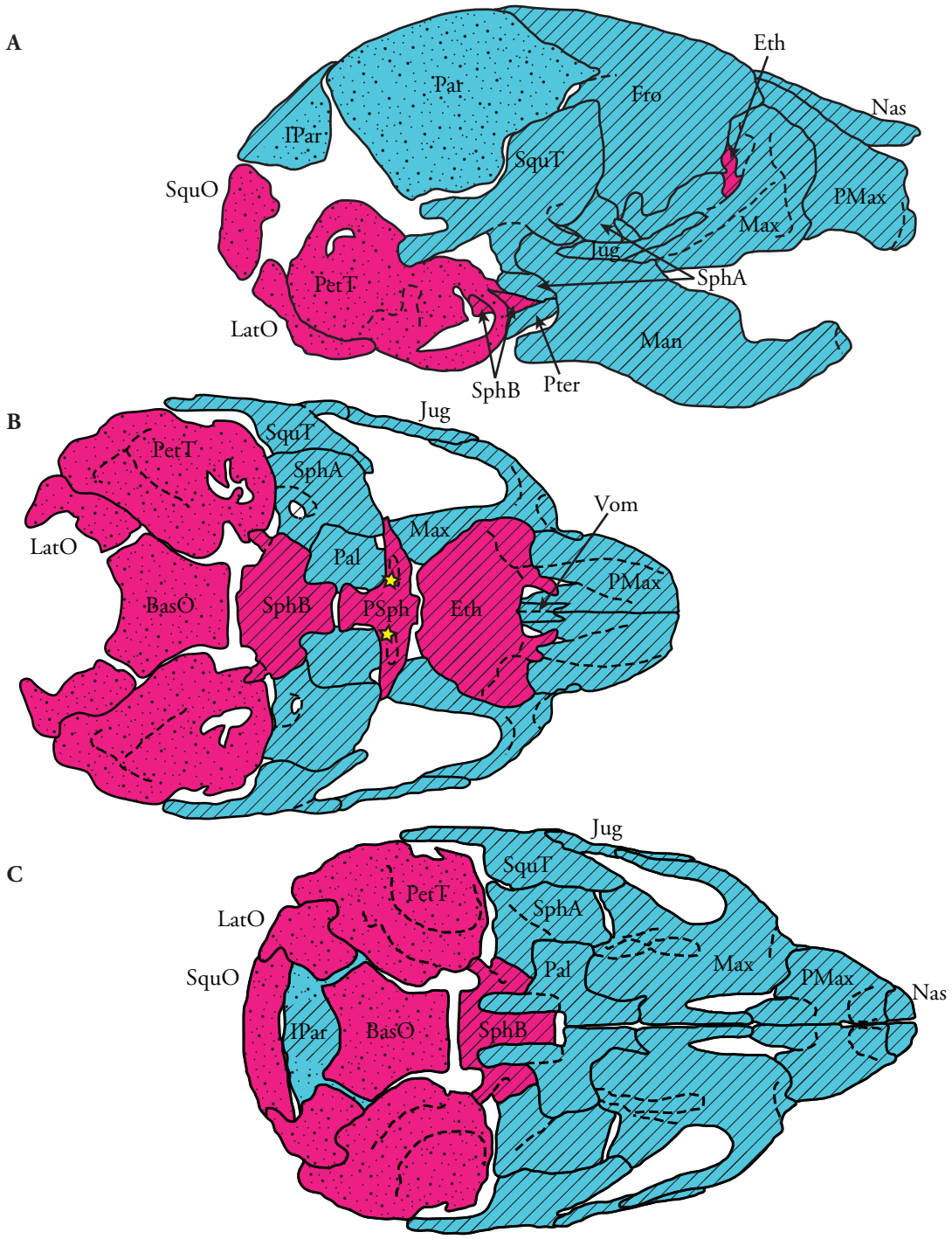

Fig 1.1 Ossification type and cellular origin of postnatal day eight (P8) mouse craniofacial bones from (A) a lateral view, (B) a superior interior view lacking calvaria, nasals, and mandibles, and (C) an interior view lacking mandibles. Red: endochondral ossification; Blue: intramembranous ossification; Diagonal lines: neural crest derived cellular origin; Dots: mesoderm derived cellular origin. Stars identify small portions of medosderm derived bone within the mostly neural crest derived presphenoid. Bone abbreviations defined in Table 1.1. Ossification identification from (Depew et al., 2002). Cellular origin of cranial base from (McBratney-Owen et al., 2008). Calvarial cellular origin from (Jiang et al., 2002). Other cellular origin from (Noden and Trainor, 2005).

Table 1.1 Bone abbreviation definitions for Fig 1.1.

Abbreviation	Bone Name
BasO	BasiOccipital
Eth	Ethmoid
Fro	Frontal
IPar	Interparietal
Jug	Jugal
LatO	Lateral Occipital
Man	Mandible
Max	Maxilla
Nas	Nasal
Pal	Palatine
Par	Parietal
PetT	Petrous Temporal
PMax	Premaxilla
PSph	Presphenoid
Pter	Pterygoid
SphA	Sphenoid Ala
SphB	Sphenoid Body
SquO	Squamous Occipital
SquT	Squamous Temporal
Vom	Vomer

while ossification is induced (Colnot et al., 2004). For intramembranously formed vault bones, a relatively high mesenchymal cell density may be necessary for the initiation of osteoblast differentiation (Thompson et al., 1989) and there is evidence that the rate of calvarial bone growth is determined by the size of osteoprogenitor cell population at the edge of condensations early in skeletogenesis and at bone fronts later on (Lana-Elola et al., 2007). However, significant cell proliferation and outward expansion of the condensation continues as initial ossification occurs in mouse vault bones (Yoshida et al., 2008). This suggests that while a mesenchymal condensation serves as the cellular basis for a vault bone, it does not necessarily resemble the adult shape of the bone at the point of initial ossification.

Although mesodermal and neural crest derived mesenchymal populations contain vasculature early on, the prechondrogenic and preosteogenic condensations formed from these populations appear to be avascular from their first formation until initial ossification (Eames et al., 2003). In the chick limb bud, the core region becomes avascular, which includes the forming mesenchymal condensation and a thin layer of avascular loose mesenchyme (Drushel et al., 1985). Artificial retention of vascularization in an area prevents mesenchymal condensation and chondrogenesis (Yin and Pacifici, 2001). Normally developing avascular limb condensations differentiate into cartilage,

while the surrounding vascularized tissues differentiate into muscle and other tissues, suggesting that vasculature could provide a positional signal for cell differentiation (Caplan et al., 1983; Drushel et al., 1985). In addition to anti-angiogenic properties responsible for the creation of a surrounding avascular zone, the limb bud may produce signals that pattern vasculature throughout the rest of the developing limb (Eshkar-Oren et al., 2009). After the differentiation of prechondrogenic condensations, the resulting cartilage models remain avascular through expression of an anti-angiogenic factor that prevents vascular invasion, although they may contain vascular canals (Kuettner et al., 1983). We are currently unaware of comparable studies of mammalian limb condensation vascularization.

Sites of intramembranous bone formation have also been associated with avascular zones (Eames and Helms, 2004), but are far less well studied. An avascular zone surrounds chick mesenchymal scleral condensations at their initial formation (Jourdeuil and Franz-Odendaal, 2012), chick frontal bone mesenchymal condensations prior to their ossification (Thompson et al., 1989), chick mandibular condensations (Eames and Helms, 2004), and rat mandibular condensations prior to ossification (Zernik et al., 1990). The chick frontal bone mesenchymal condensations are surrounded by a thin avascular layer of loose mesenchyme (Thompson et al., 1989), as seen in limb bud condensations. Even though few studies mention the association of vasculature and preosteogenic mesenchymal condensations, it appears that avascular regions are likely to surround preosteogenic condensations in avian and mammalian species. However, even in the case of prechondrogenic condensations, the mechanism underlying the establishment of avascular zones remains unclear (Eshkar-Oren et al., 2009).

Epithelial signals play a major role in regulating the initiation of cell migration and proliferation to form a mesenchymal condensation as well as initiating mesenchymal stem cell differentiation (Hall, 1992). A great number of signaling factors, including fibroblast growth factors (FGFs) are known

to be involved in the condensation and maintenance of mesenchymal cell populations that form the basis of skeletal elements (Hall and Miyake, 2000), although it is unknown what signals cue the first aggregation of cells (Colnot et al., 2004). Members of the TGFβ superfamily, including GDFs and BMPs, are critical for the growth of these condensation as they promote cell-cell and cell-extracellular matrix interactions (Chimal-Monroy and Diaz de Leon, 1999; Hall and Miyake, 1995). Integrin cell-surface receptors, which link extracellular and intracellular signaling, influence gene expression within these condensations (Karaplis, 2008).

Once differentiation begins, divergence in patterns of gene expression are noted between prechondrogenic and preosteogenic condensations (Eames and Helms, 2004). These differences in gene expression are likely necessary to direct mesenchymal precursors to the correct cell fate, because they retain a degree of pluripotency (Hall, 2005; Karaplis, 2008). For instance, in the presence of Wnt signaling, mesenchymal cells will differentiate into osteoblasts rather than chondrocytes (Karaplis, 2008). Because of clear differences in mesenchymal cell differentiation and ossification, we discuss endochondral and intramembranous ossification separately. However, similarities in the role of angiogenesis during both types of osteogenesis suggest significant parallels.

ENDOCHONDRAL SKELETOGENESIS

In addition to every postcranial mouse bone except the clavicle, bones of the cranial base, the occipital, and the ethmoid are ossified from cartilaginous models (Fig 1.1) (Depew et al., 2002). The following descriptions of endochondral ossification come largely from studies of limb bone development. These provide an overview of endochondral skeletogenesis and a basis for comparing intramembranous ossification, for which relatively little is known. It is not completely clear how endochondral ossification of craniofacial bones might differ from that of long bones other than a lack of epiphyseal ossification plates. Gene expression patterns of skeletogenic transcription factors from

mesenchymal condensations destined for endochondral ossification in the head and limbs of chicks are similar (Eames and Helms, 2004), suggesting similar developmental processes.

After the formation of a prechondrogenic mesenchymal condensation, surrounding loose mesenchymal cells flatten and elongate to become an enveloping perichondrium. Mesenchymal cells within the condensation differentiate into chondrocytes that form the cartilage model of the bone (Eames et al., 2003; Hall and Miyake, 2000). Osteoid is deposited first in a collar near the mid-diaphysis, which is frequently described as being within the perichondrium (e.g. Mackie et al., 2008; Takimoto et al., 2009; Nakamura et al., 2010), although it has also been described as being separate (Caplan et al., 1983). Hypertrophy of mid-diaphyseal chondrocytes within the cartilage anlagen is noted, producing signals for the invasion of the cartilage by endothelial cells (Kronenberg, 2003; Colnot et al., 2004). Expression of vascular endothelial growth factor (VEGF), an important angiogenic factor, by perichondrium and tissues surrounding mouse long bones is important in signaling vasculature to approach the cartilaginous bone model in the day or two before initial ossification, with particularly high expression at E14.5 in a mesenchymal region that will soon undergo ossification (Zelzer et al., 2002). In this way, VEGF expression appears to be directly associated with attracting vasculature towards sites of future ossification.

The bone collar ossifies as vasculature makes contact with the perichondrial cells at the mid diaphysis (Takimoto et al., 2009), leading the perichondrium to become the periosteum (Eames et al., 2003). The perichondrium presents anti-angiogenic properties similar to the cartilage model itself until this time, when VEGF and TGF-β expression are associated with heavy vascularization of the perichondrium. The bone collar appears to play a key role in regulating the location of initial vascular invasion of the cartilage model, which leads to initial ossification at the mid-diaphysis (Takimoto et al., 2009). Vascularization of the periosteum is necessary for osteoblast differentiation within it and for

subsequent vascular invasion of the cartilage model (when the periosteum is removed, angiogenesis starts much later) (Colnot et al., 2004). Between E14.5 and E15.5, VEGF expression in peripheral mesenchyme disappears and expression within hypertrophic chondrocytes of the mouse cartilage is noted (Zelzer et al., 2002), along with the expression of other factors that promote angiogenesis. Epithelial sprouts derived from the vasculature within the perichondrium invade the hypertrophic regions of the cartilage model (Caplan et al., 1983) via angiogenesis. Chondroclasts, which may be the same as osteoclasts, are found preceding the tips of invading capillaries during osteogenesis, allowing the epithelial cells to make their way through the cartilage (Lewinson and Silbermann, 1992; Streeten and Brandi, 1990).

At the same time, the developmental cascade of chondrocyte hypertrophy, vascular invasion, osteoid formation, and calcification moves from the mid-diaphysis towards the ends of the bone (Caplan et al., 1983). After the formation of epiphyseal growth plates, the cascade continues postnatally as the basis for increasing long bone length, a process that has been well studied (Kronenberg, 2003; Mackie et al., 2008; Amizuka et al., 2012). There are several layers of tissue commonly noted at long bone growth plates. Closest to the epiphysis is a population of proliferating chondrocytes, which differentiate into hypertrophic chondrocytes, around which mineralization starts to occur, before local vascular invasion and ossification (Fig 1.2). As during initial endochondral ossification at the diaphysis, the hypertrophic chondrocytes near the epiphyses produce signals upregulating local angiogenesis, which leads to capillary invasion of the hypertrophic region from the currently mineralizing region (Gerber et al., 1999). In rat long bones, capillary sprouts of continuous epithelium move in parallel towards the epiphysis up to a distance of 350 microns away from the primary vessels that supply and drain them (Hunter et al., 1991).

At chick long bone epiphyseal plates, the first parts of the differentiated hypertrophic matrix

to mineralize are the portions closest to the invading vasculature (Boyde and Shapiro, 1987; Shapiro et al., 1988). During osteoid secretion, one of the first steps of ossification, osteoblasts become arranged as a highly polar monolayer along invading vessel endothelium, with their secretory face toward the osteoid front (Hansen, 1993). This association leads to bone struts being formed around invading vasculature. Osteoblasts mature and become embedded as osteocytes in the bone matrix, while new osteoblasts adjacent to the vessel secrete osteoid (Hansen, 1993). This typical process of bone formation from cells surrounding vascular endothelium leads to zones where poorly mineralized cartilage and highly mineralized bone co-occur, rather than a flat plane of mineralizing bone parallel to the epiphyseal plate (Boyde and Shapiro, 1987).

Relatively recent studies have illuminated some of the regulatory interactions that bring vasculature into preosteogenic epiphyseal cell populations and what effect these interactions have on ossification. VEGF expression by hypertrophic chondrocytes has been known to play a critical role in vascular invasion at the growth plate and subsequent ossification for more than a decade (Gerber et al., 1999). Deletion of a single VEGF allele leads to embryonic lethality, while the loss of certain isoforms can lead to serious skeletal defects of postcranial and calvarial bones , associated with delayed vascular invasion (Zelzer et al., 2002). VEGF expression in condensing limb

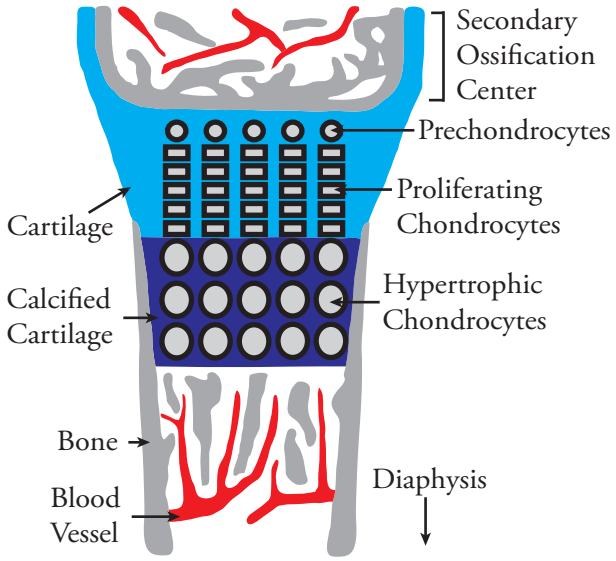

Fig 1.2 Schematic of epiphyseal ossification of endochondral long bones. Chondrocytes differentiate from proliferating prechondrocytes within the cartilage of the epiphysis, being pushed toward the diaphysis by the continuous process. The chondrocytes enlarge under hypoxia, leading to mineralization of the cartilage and subsequent mineralization of new bone by osteoblasts found apposed to blood vessels, which grow in the direction of the hypoxic cartilage. This figure was inspired by previously published figures (Kronenberg, 2003; Bloom and Fawcett, 1994).

bud mesenchyme plays an important role in regulating limb vasculature surrounding prechondrogenic condensations (Eshkar-Oren et al., 2009). Continued research has shown VEGF mediates not only angiogenesis, but chondrocyte differentiation, osteoblast differentiation, and osteoclast recruitment (Zelzer and Olsen, 2004; Dai and Rabie, 2007).

Hypoxia inducible factor (HIF), commonly upregulated in regions of hypoxia (Pugh and Ratcliffe, 2003), is a promoter of VEGF expression (Towler, 2008) and is known to directly regulate osteoblasts in endochondral bones. Increased expression of HIFα in osteoblasts of early postnatal mice is associated with increased VEGF expression, increased vascular density in their long bones as well as increased long bone growth rate, leading to increased femur bone volume and trabecular number (Wang et al., 2007). Although HIF is an important regulator, it has been shown that other factors, including bone morphogenetic proteins (BMPs) can also upregulate VEGF (Towler, 2008).

A number of genetic factors, independently respond to hypoxia in tissue culture, including angiopoietins, FGFs and their receptors, and genes involved in matrix metabolism (Pugh and Ratcliffe, 2003). Some FGF and FGF-receptor (FGFR) interactions directly increase VEGF expression (Saadeh et al., 2000; Takai et al., 2007), play a role in ossification at the growth plate (Liu et al., 2007), and promote angiogenesis as well as osteoblast recruitment during the endochondral process of fracture repair (Bolander, 1992; Kawaguchi et al., 2001; Komaki et al., 2006). Although FGF-FGFR signaling has been primarily associated with bone cell regulation during initial ossification and growth, some effects of FGFR mutations on long bone growth, including achondroplasia (Horton and Lunstrum, 2002), are likely to stem from changes in angiogenesis regulation.

There is evidence that several other factors regulate angiogenesis at growth plates. Delay of vascular invasion is noted at mouse growth plates lacking parathyroid hormone (PTH) / PTH-related peptide (PTHrP) signaling (Schipani et al., 1997), although this might be based on delayed chondrocyte

hypertrophy rather than direct regulation of angiogenesis. Injected FGF-6 at rabbit proximal tibial growth plates accelerates vascular invasion and ossification of the growth plate, although it might independently upregulate both angiogenesis and osteogenesis (Baron et al., 1994).

Non-genetic factors are also known to be critical to the normal association of vasculature and ossification at long bone epiphyses. Lack of vitamin D, commonly associated with rickets, a disorder of bone growth that leads to bone softening and bowing, has been associated with a lack of normal vascular invasion into hypertrophic cartilage (Hunter et al., 1991). A vitamin D deficient diet in rats leads to abnormal vascular invasion of the hypertrophic cartilage and dysmorphology associated with rickets, including reduced bone growth rate and lower levels of mineralization (Hunter et al., 1991).

While the focus of this chapter is on angiogenesis-osteogenesis interactions, genes that directly regulate chondrocyte proliferation, chondrocyte hypertrophy, matrix protein production, or osteoblast differentiation, are critical for proper long bone ossification. Further details on gene networks associated with endochondral ossification can be found in numerous existing review articles (e.g. Kronenberg, 2003; Mackie et al., 2008; Mackie et al., 2011).

INTRAMEMBRANOUS SKELETOGENESIS

Bones of the face including the vomer, and bones of the cranial vault including the sphenoid ala, but not the squamous occipital are ossified intramembranously from mesenchymal condensations (Fig 1.1). While the processes of intramembranous and endochondral ossification are similar in many ways, as evidenced by similar patterns of gene expression across skeletal tissues (Eames and Helms, 2004), there are a number of important differences between the two. The following description of initial intramembranous ossification is an attempt to include information from as many studies as possible. Studies of the intramembranous vault bones (e.g. frontal, parietal) are of particular interest, because these bones are a major focus of the research described in the following chapters, but also

because their ossification is likely to be most different from the endochondral long bones.

In mice, the mesenchymal condensations of the frontal and parietal bones develop at the baso-lateral portion of the future bones, which corresponds to the supraorbital ridge. Initial ossification of these condensations occurs as mesenchymally derived presumptive bone cells quickly proliferate outwards from condensation edges. Studies utilizing DiI staining provide evidence that the bone primordial cells proliferate and migrate outward from the condensations rather than being recruited from other mesenchymal populations surrounding the brain (Yoshida et al., 2008; Ting et al., 2009). Together, studies staining for osteopontin (Iseki et al., 1997), ALP expression (Ting et al., 2009), and BSP expression (Rice et al., 2000) suggest a pattern of presumptive bone cells expanding outward from bilateral mesenchymal condensations, particularly towards the apex of the head, and not meeting within presumptive sutures. During the earliest embryonic days of vault bone skeletogenesis, these expanding bone primordia provide the basis for ossification. Subsequent embryonic expansion of ossified bone is driven by proliferation of preosteogenic mesenchymal cells at osteogenic fronts along fibrous sutures (Iseki et al., 1997; Liu et al., 1999; Rice et al., 2003). In calvarial cultures of the mouse sagittal suture, implantation experiments indicated that mesenchymal cells being incorporated into the parietal bones are recruited from the osteogenic front and do not migrate from within the developing bone, although a small minority may come from the suture mesenchyme (Lana-Elola et al., 2007).

At the same time that the ossifying bones are expanding outward, earlier ossified portions are thickening and forming a trabecular structure (Yoshida et al., 2008). Differentiated osteoblasts first form bone spicules, which develop and eventually fuse together to form trabeculae, which become interconnected to form woven bone (Kanczler and Oreffo, 2008). As first described decades ago (e.g. Murray, 1985; Thoma, 1913) and supported by images from recent studies (Fig 1.3), the initial woven bone of flat intramembranous bones can be described as a bone lattice or network that is filled in as

ossification progresses.

Distinct from endochondral ossification, where initial mineralization occurs within a cartilage model possessing the rough shape of the adult bone that delineates the shape of future ossification; during intramembranous vault bone formation, the initial expansion of bone primordia serves to define the original extent of developing bone, representing an initial stage of skeletogenesis. Only after this stage is complete, at a point when ossification is well underway in some parts of the bone, vault bone growth begins to resemble more traditional descriptions of radial growth from a center, based on signaling at the suture margins (Lana-Elola et al., 2007; Yoshida et al., 2008).

Intramembranous ossification of non-vault bones is not well described. Initial ossification of the rat dentary is noted as an arch surrounding, although probably not touching, meckel's cartilage (Zernik et al., 1990). It is not known whether the cartilage plays a regulatory role in the ossification of

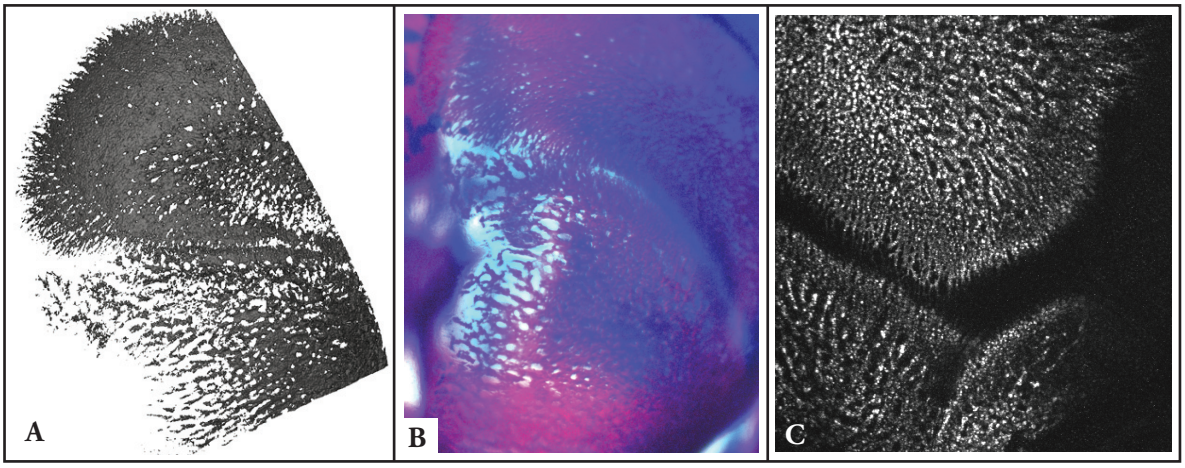

Fig 1.3 High resolution images of perinatal mouse frontal and parietal bones produced by multiple imaging modalities. Note the lattice-like pattern at the edges of ossification, with bone filling in the gaps in older areas of bone. All images are an oblique dorsal view for which caudal is towards the bottom of the image and the medial is to the left. A) Surface reconstruction around the medial coronal suture of a newborn Apert syndrome model mouse from an image produced at the High-Resolution X-ray Computed Tomography Facility at the University of Texas at Austin. The hard edges of the image represent the extent of the region of the bone that was imaged. B) Lightfield microscope image of the medial coronal suture of a whole-mount Ailzarin red/Alacian blue clear and stained E18.5 *Fgfr2*$^{+/P253R}$ Apert syndrome model mouse (Wang et al., 2010). Image courtesy of Mizuho Kawasaki and Kazuhiko Kawasaki . C) Two photon laser scanning microscopy image of the lateral coronal suture of an E19.5 C57BL/6 mouse. The bones have been marked with calcein. Image courtesy of Kevin Flaherty and Patrick Drew.

the intramembranous dentary or whether cells from an initial mandibular mesenchymal condensation expand outward as ossification begins.

Calvarial Suture Formation and Maintenance

Many genes associated with the initial expansion of cranial vault bone primordia and their ossification are also associated with later radial expansion at the edges of calvarial sutures. Given this fact, it is plausible that the same regulatory pathways are being utilized for both phases of vault bone ossification (Lana-Elola et al., 2007). If this is the case, what prevents the vault bones from continuing their primordial expansion until they abut? Instead, sutures made up of fibrous tissues are defined between bones of the skull and remain patent during early postnatal rapid bone formation (Opperman, 2000; Morriss-Kay and Wilkie, 2005). It is not clear whether signals for suture formation exist at the site of suture formation before bone primordia approach each other or whether emergent regulatory interactions of approaching bone primordia lead to the creation of a suture. If some outside signal, perhaps from gene expression of the underlying brain (Iseki et al., 1997) or dura (Opperman, 2000), prevents bone primordia from approaching each other, then variation in suture formation and associated cranial bone form would be based on regulation by other tissues. If primordia cease moving towards each other because of emergent properties of newly interacting regulatory networks at bone fronts, then calvarial variation associated with variation in suture formation would stem from gene expression of cells originating from intramembranous mesenchymal condensations. Known patterns of gene expression reveal some clues about the regulation of initial calvarial suture formation.

Near the future mouse coronal suture, the juxtaposition of neural crest derived cells associated with the future frontal bone and mesodermally derived cells associated with the future parietal bone is clear by E9.5 (Jiang et al., 2002), shortly after the beginning of neural crest migration. While it has been proposed that maintenance of the boundary between neural crest and mesodermal cells is

important for normal coronal and sagittal suture development (Morriss-Kay and Wilkie, 2005; Merrill et al., 2006; Deckelbaum et al., 2012), premature obliteration of the coronal suture can occur without aberrant migration of cells across the border (Holmes and Basilico, 2012). In mice at E13.5, just before initial frontal ossification, FGFR2 expression in mice reveals the frontal and parietal mesenchymal condensations separated by the presumptive coronal suture (Yoshida et al., 2008). In this case, the suture is defined by a lack of FGFR2 expression between the FGFR2 expressing mesenchymal condensations. At E10, TWIST1 is expressed within all cranial mesenchyme, but then is restricted to the border of mesenchymal condensations and near developing cartilages by E14 (Rice et al., 2000). In this case, the suture is defined by the retention of TWIST expression in calvarial mesenchyme between the calvarial bones, although it is also expressed by cells in the earliest stages of osteoblast differentiation. Studies of calvarial sutures, frequently focused on the coronal suture, illuminate a pattern of exclusive and often concentric gene expression domains that serve to define developing vault bones and sutures during the prenatal and early postnatal periods.

Studies of mice reveal that FGFR2 expression is associated with the proliferation of presumptive osteogenic cells. It is expressed throughout the frontal and parietal mesenchymal condensations at E13.5 (Yoshida et al., 2008), but becomes more scattered towards the apex of the head by E15.5, later becoming expressed at the outer edge of the expanding presumptive bone, then as the outer edge of the bone front at the sutures by birth (Iseki et al., 1997). Expression of osteopontin, an organic component of bone, is associated with regions of the presumptive bone that lack ossification, but which have low proliferation. Osteopontin expression seems to follow that of FGFR2, becoming a concentric ring within the borders of FGFR2 expression at the suture edge later in development (Iseki et al., 1997). This suggests its expression domain represents mesenchyal cells differentiating into osteoblasts. FGFR1 expression is also associated with osteoblast differentiation, being found

closer to the ossifying portions of the vault bones than FGFR2 expression and overlapping with the outer edge of osteopontin expression (Iseki et al., 1999). Both FGFR1 and osteopontin expression do not overlap with FGFR2 expression at the edge of the suture. FGFR3 is weakly expressed, partially overlapping FGFR1 and FGFR2 expression in E16 mice (Iseki et al., 1999).

ID and TWIST1 are expressed in undifferentiated mesenchyme, later delineating the outer edge of the osteogenic fronts and are thought to represent early osteoprogentior cell populations (Rice et al., 2000). TWIST1 appears to be expressed across regions of undifferentiated mesenchyme at E10, with restriction of its expression to the border of mesenchymal condensations by E14. At this time, both TWIST and ID appear to be expressed by osteoprogenitors, but not mature osteoblasts. After the bone fronts approach each other, they are strongly expressed in the mid-sutural mesenchyme along with FGF2. FGF2 is known to upregulate TWIST1 expression, while TWIST1 expression in the suture appears to prevent local FGFR expression. TWIST1 is involved in the maintenance of tissue boundaries at the suture (Ting et al., 2009), potentially by inhibiting factors associated with osteoblast differentiation including RUNX2 and MSX2 (Lana-Elola et al., 2007). In this way, TWIST1 plays an important role in keeping the suture patent, allowing for continued expansion of the surrounding bones.

Disruptions of the expression patterns of these and other genes at the sutures are known to lead to their obliteration through bone fusion; a process referred to as craniosynostosis (Cohen Jr and Maclean, 2000). Among others, mutations of FGFR1-3, TWIST1, EFNB1, MSX2, RAB23 have been associated with human craniosynostosis syndromes (Passos-Bueno et al., 2008) and are thought to primarily cause associated dysmorphology through regulatory effects on osteoblast proliferation, differentiation (Iseki et al., 1999; Rice et al., 2000), or migration (Ting et al., 2009). However, if angiogenesis plays as important a role during intramembranous ossification as it does

during endochondral ossification, the expression of known angiogenic factors including FGFs within sutural mesenchyme and FGFRs within the bone fronts suggest that some craniosynostosis associated mutations might influence craniofacial morphology via dysregulation of angiogenesis. Therefore, investigating the effect of angiogenesis regulation on intramembranous ossification, including FGF-FGFR signaling, may be important for understanding the basis of intramembranous bone variation.

Angiogenesis and Intramembranous Ossification

The importance of angiogenesis during endochondral long bone ossification has been well established and its importance during intramembranous ossification is generally assumed. While intusucceptive angiogenesis (Levin et al., 2007) may occur in vessels associated with craniofacial bone development, it is usually assumed that sprouting angiogenesis, a process based on the extension of vessel sprouts outward from existing vasculature, is the primary form of angiogenesis associated with osteogenesis. A single well cited study of chick frontal bone skeletogenesis outlines the association of angiogenesis with intramembranous ossification of vault bones (Thompson et al., 1989). As with the mouse frontal and parietal bones, the chick frontal bone initially ossifies within a condensation at the supraorbital ridge. In the developmental stage just prior to initial ossification of this bone, small bore capillaries move into the thin avascular layer of loose mesenchyme surrounding the mesenchymal condensation. These small vessels then invade the condensation at or near the site of initial ossification at the supraorbital ridge. After a short time, the earliest mineralized bone begins to develop marrow spaces and becomes associated with extensive internal and external vascularization, while the cascade of vascular invasion and ossification continues as a front moving outward in all directions. Within the earlier ossified and maturing bone of the chick frontal, the osteoblast layer and large bore capillaries are apposed (Thompson et al., 1989).

Assuming this association of growing capillaries and the bone front exists for mice, we

anticipate capillaries approaching the avascular mesenchymal condensation of the vault bone just prior to initial ossification at E14 or E14.5. Then, we expect vascular invasion at or near the site of initial ossification, at or around the time it occurs. Finally, we expect angiogenesis to continue, either from the center of ossification or from capillaries local to the expanding bone primordia, vascularizing the proliferating population of mesenchymal preosteoblasts (Fig 1.4). Radiographic images of Thorotrast filled calvarial capillaries in fetal humans show vessels radiating outward like spokes from a center of ossification towards the bone edges (Fig 1.5) (Brookes and Revell, 1998), supporting the idea that angiogenesis within developing intramembranous bones stem from central points of vascular invasion.

Although the association of angiogenesis and intramembranous skeletogenesis in early development has not been well studied, the results of distraction osteogenesis, for which

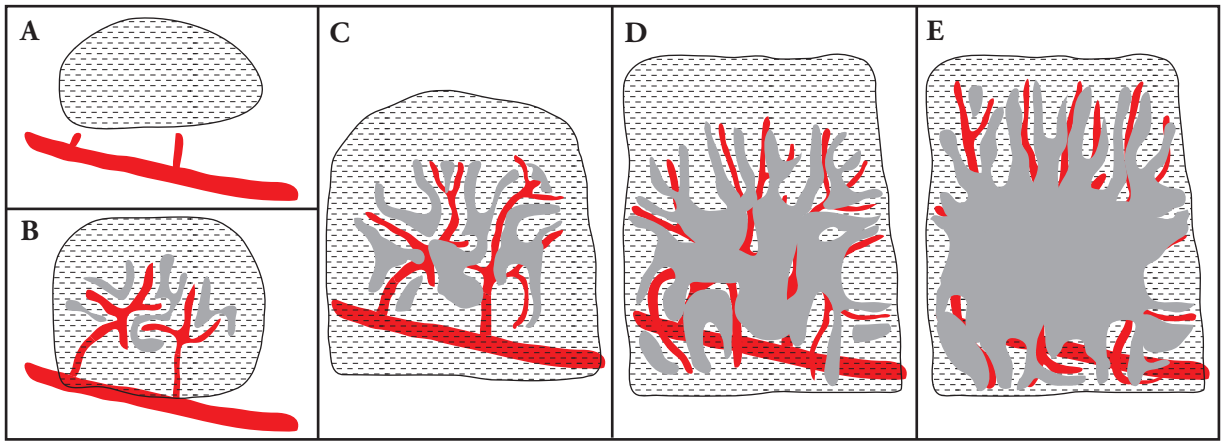

Fig 1.4 Hypothetical schematic of the association of mesenchymal precursors, invading blood vessels, and bone formation during the initial phase of intramembranous calvarial ossification. Note the change from a lattice-like ossification pattern near new vasculature sprouts to a more complete mature bone later in time. A) Blood vessels (solid red) approach the border of the avascular mesenchymal condensation (dashed region). B) As mesenchymal cells migrate outwards, blood vessels invade the condensation near the center of ossification at or around the time of initial ossification (solid grey), which occurs in proximity to invading vasculature. C,D) Mesenchymal migration continues outward until mesenchymal cells receive some signal to stop, often at sutures that form between the advancing mesenchymal fronts of two bones. Vessels continue to extend outward through the mesenchymal condensation, remaining proximate to new regions of bone formation, as previous sites of bone formation begin to merge and mature. E) As the blood vessels and regions of ossification approach the edge of the mesenchymal condensation, an ossification front forms at the suture margins, which will allow for continued calvarial growth.

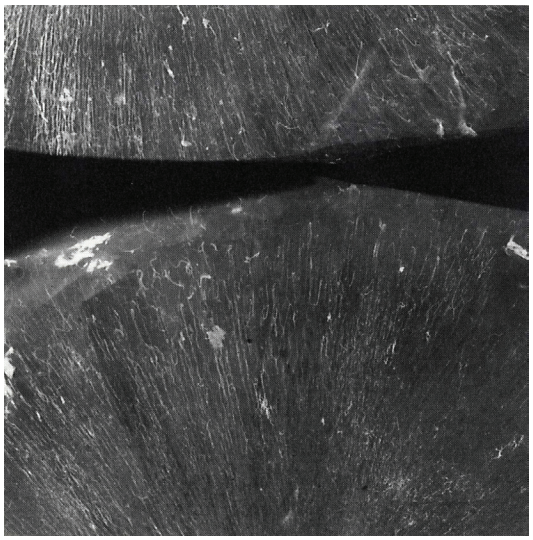

Fig 1.5 Radiographic image of the two parietal bones of a human fetal skull after vascular perfusion with radioactive Thorotrast. The vasculature within the developing parietal bones can be seen radiating outward from their centers. Source: Image reproduced with kind permission of Springer Science+Business Media (p.65, Brookes and Revell, 1998).

intramembranous ossification is the primary mode of ossification (Aronson et al., 1990; Delloye et al., 1990), provides important insight. Distraction osteogenesis is a surgical procedure designed to increase bone length by cutting the bone and slowly pulling the portions away from each other. After the initial separation, a bone callus of rigid connective tissue forms in response to tissue inflammation. After a time, tensile forces are applied to the callus at specific rates and rhythms, in a process called distraction. A central fibrous interzone made up of fibroblasts, chondrocyte-like cells, and cells of intermediate morphology forms (Fig 1.6) (Choi et al., 2002; Al-Aql et al., 2008). Vascular in-growth appears on either side of the fibrous interzone within which osteoblasts begin laying down osteoid along collagen bundles, forming the zone of microcolumn (linear bone features) formation. In between the zone of microcolumn formation and the fibrous interzone is a zone of proliferating cells called the primary mineralization front, which also overlaps with the encroaching vasculature. Vascular sinuses formed by the vascular in-growth are the sites from which bone formation begins (Choi et al., 2002). After distraction ceases, the microcolumns of osteoid and bone begin to move towards each other, filling the fibrous interzone. Remodeling of the bony region is the last step in the process. In a sense, the zones associated with distraction osteogenesis are similar to the sutures connecting intramembranous bones of postnatal calvaria, where tension supplied by the expanding brain across a fibrous suture is purported to be associated with osteoblast precursor proliferation and differentiation close to the

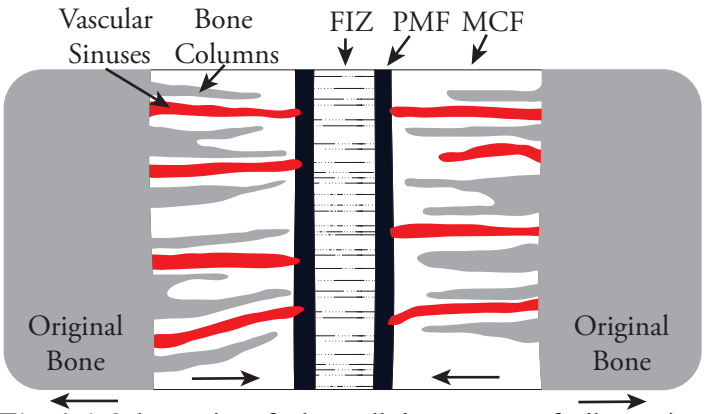

Fig 1.6 Schematic of the cellular zones of distraction osteogenesis. The fibrous interzone (FIZ) forms first and is composed of a variety of cells, including osteoblasts that deposit osteoid along parallel collagen bundles. The zone of microcolumn formation (MCF) includes invading vascular sinuses and vessels, from the original bone portions, in parallel with tension across the FIZ and in association with microcolumns of mineralizing bone along the previously formed collagen bundles. Between the FIZ and MCF is the primary mineralization front (PMF), which is a thin zone of high cellular proliferation. The MCF continues expanding as the portions of the original bone are pulled apart, while the FIZ remains a constant width.

suture (Opperman and Rawlins, 2005). But, it is unclear whether distraction osteogenesis is a good analogue for initial vault bone skeletogenesis (Choi et al., 2002; Al-Aql et al., 2008).

During distraction osteogenesis, there is a significant increase in blood supply and rates of blood flow at sites of bone formation. Vessels of uniform diameter extend from the surfaces of the cut bone toward each other along the collagenous fibers, but do not enter the fibrous interzone (Aronson et al., 1990; Delloye et al., 1990; Aronson, 1994; Choi et al., 2000). Just ahead of the mineralization front in the fibrous interzone are parallel capillaries that have a close temporal and spatial relationship with sites of new mineralization at the distraction gap. After distraction ceases, these vessels aligned along collagen fibers grow towards each other and meet before the gap is completely filled with osteogenic tissue (Choi et al., 2002). In rats undergoing distraction osteogenesis, treatment with an angiogenic inhibitor led to non-union of the separated bones, a lack of ossified bone and blood vessels between the original cut bone portions, and reduced expression of a number of genes, including those associated with osteogenesis. Additional experiments where mechanical tension was not introduced led to fibrous tissue lacking evidence of vasculature between the separated bones (Fang et al., 2005). This suggests that the expression of angiogenic factors and subsequent vascular invasion towards

the fibrous interzone are necessary for intramembranous ossification to occur during distraction osteogenesis. It also suggests that tension is a necessary part of ossification; when tension is not present, low levels of angiogenesis and bone mineralization occur. This is similar to studies indicating that tension across sutures upregulates certain gene products, including angiogenic (and osteogenic) factor FGF-2, leading to the addition of bone at the sutural edge of vault bones (Yu et al., 2001; Opperman and Rawlins, 2005). During distraction osteogenesis, angiogenesis is critical and directly precedes, in time and space, the appearance of differentiated osteoblasts and mineralization, as it does at epiphyseal growth plates of endochondral long bones. This supports the idea that angiogenesis likely precedes osteogenesis during early vault bone intramembranous ossification as well.

While hypoxic cartilage cells within cartilage bone models serve to upregulate angiogenesis during endochondral bone growth, there doesn't appear to be a similar thick mass of hypoxic cells near sites of initial vault bone formation. Hypoxia may not play as significant a role in promoting angiogenesis and subsequent osteogenesis during intramembranous bone formation as it does during endochondral bone formation. While increased osteoblast expression of hypoxia inducible factor alpha (HIFα) is associated with increased vasculature of murine long bones, murine calvarial bones are reportedly unaffected (Wang et al., 2007), although images of calvarial bones associated with this study suggest reduced linear scale. Comparison of HIFα expression patterns between fetal pig forelimb and palate revealed that the HIF-α1 isoform was detected only in endochondral bones, while isoform HIF-α2 and HIF associated factors angiopoietin and VEGF were expressed in both (De Spiegelaere et al., 2010). While similar angiogenesis factors are expressed during intramembranous and endochondral ossification, there may be significant differences in the regulatory pathways that upregulate these angiogenic factors.

THE IMPORTANCE OF BLOOD VESSEL PROXIMITY

There is strong evidence that the process of angiogenesis is as important during intramembranous ossification as it is during endochondral ossification. In both cases, abrupt angiogenesis into a previously avascular cellular population is associated with ossification of bone within that population as well a host of other cellular activities and gene expression patterns. Regardless of how angiogenesis is initiated at these times and locations, it is clear that close proximity to blood vessels is necessary for normal bone formation. There are several reasons why this might be the case.

Proximity to the vascular network can provide access to the variety of electrolytes, proteins, gasses, lipids, minerals, and pluripotent cells found in the blood supply. In addition, vasculature can provide a sink for cellular waste products. One of the major roles of blood is to transport oxygen and carbon dioxide, which is mostly bound to the hemoglobin of erythrocytes (Thiriet, 2008). Given that angiogenesis tends to occur in regions of increased hypoxia, the delivery of oxygen to hypoxic cells is clearly an important role of new capillary systems. Calcium and phostphate ions must also be transferred to sites of ossification (Heaney, 2008), probably via blood vessels. Additionally, the relatively high levels of oxidative metabolism associated with cells near regions of ossification at the chick endochondral limb growth plate, suggest that access to oxygen and other factors is necessary for increased cell activity associated with normal ossification (Shapiro et al., 1988).

Access to the correct combination of circulating hormones is necessary for non-dysmorphic skeletal development (Karaplis, 2008). However, it is not completely clear whether access to these factors is critical at the earliest stages of skeletogenesis. Factors that are integral for bone growth postnatally may not be necessary for initial ossification. For instance, mice lacking the receptor for growth hormone (GH), which is necessary for the growth of limbs to expected lengths, do not display modified bone growth before three weeks of age (Sims et al., 2000). Other blood circulating factors

including a variety of electrolytes are likely to play a role in the normal activity of cells local to sites of initial ossification, but it is unclear whether these factors are also available at sufficient concentrations in local extracellular fluid. Similarly, some blood circulating proteins (serum proteins) are likely to be utilized by osteoblasts in the production of the bone matrix, but most of matrix proteins are probably produced locally. While the transport role of blood vessels are likely critical to the earliest stages of bone formation, further study will be necessary to determine exactly why proximity to vasculature is associated with sites of initial bone formation. However, recent work may reveal answers to the issue of whether vasculature provides access to osteoblast precursors during initial ossification.

Cell Precursor Origin

Vessels may provide an important route for preosteogenic cells to reach regions where ossification is occurring. A population of circulating osteoblast lineage cells in humans has been identified (Eghbali-Fatourechi et al., 2005) and shown to contribute to vasculogenesis and osteogenesis during fracture healing of a rat experimental model (Matsumoto et al., 2006), although whether these circulating cells are the principal bone forming cells in normal bone remodeling and fracture repair remains unknown (Parfitt, 2001; Eghbali-Fatourechi et al., 2007; Eriksen et al., 2007). Even if circulating cells are the primary source of osteoblasts during postnatal growth and development, this does not necessarily mean that they assume the same role during prenatal skeletogenesis. Several sources of osteogenic cells for the earliest stages of bone mineralization have been proposed over the years.

During the earliest stages of endochondral bone mineralization, including bone collar formation and mid-diaphyseal ossification, it has been proposed that osteoblasts differentiate from mesenchymal cells surrounding the mid-diaphysis (Caplan et al., 1983) and/or adjacent perichondrium (Kronenberg, 2003). As ossification begins to move deeper into the bone and towards the future

epiphyses, blood borne cells have been implicated as osteoblast precursors (Collin-Osdoby, 1994), although local chondrocytes (Boyde and Shapiro, 1987) and local endothelial cells have also been suggested (Trueta, 1963; Hansen, 1993). Osteoblast origin may differ from site to site along with differences in the ability or likelihood of cells to dedifferentiate or transform (Hall, 2005).

Recent advances in cellular staining have allowed researchers to investigate the cellular populations from which osteoblasts are recruited during initial ossification. Using X-gal staining on renal explants of mouse limb cartilage bone models, it was demonstrated that perichondrium of an explanted bone is the source of both cortical and trabecular osteoblasts in the earliest stages of endochondral bone ossification, although associated endothelial cells originate outside of the explanted bone (Colnot et al., 2004). While perichondrium is the primary source of osteoblasts in this case and local endothelial cells appear to have a different origin than osteoblasts, this study does not rule out the possibility that some osteoblasts come from local chondrocytes.

During initial intramembranous ossification, it has been proposed that local mesenchymal cells differentiate into the osteogenic cells that produce woven bone, which is later remodeled (Collin-Osdoby, 1994). Until recently, it wasn't clear which mesenchymal population osteogenic cells originated from or whether circulating stem cells played a role in osteogenesis. DiI staining of frontal bone mesenchymal condensations at E13.5, before their rapid expansion and ossification, indicates that cells derived from the condensation populated the whole frontal bone domain at E17.5 and E18.5 (Yoshida et al., 2008). Therefore, the cellular expansion superiorly from the basi-lateral region of the future bone utilizes cells from the original mesenchymal condensation rather than recruiting significant numbers of cells from circulation or from the underlying mesenchymal populations as the primordia expands. As discussed in a previous section, osteoblasts contributing at calvarial bone fronts appears to be derived from the original mesenchymal condensation. However, a small amount of suture

mesenchyme becomes incorporated into the ossifying bone (Lana-Elola et al., 2007), suggesting that a small number of circulating osteoblast progenitors might also contribute to the ossifying calvarial bones.

Although circulating osteoblast precursors may serve as a primary source of osteoblasts during postnatal bone remodeling and fracture healing, the original mesenchymal condensations are likely to provide the primary cellular basis for osteoblasts during endochondral and intramembranous skeletogenesis. On the other hand, osteoclasts found during initial endochondral bone morphogenesis are likely to arise from blood-borne monocytes (Caplan et al., 1983). Osteoclast precursors, which have a hematopoietic origin, are known to circulate in the blood supply with monocytes (Fujikawa et al., 1996), providing the primary pool of osteoclasts for bone resorption associated with bone remodeling (Eriksen et al., 2007). Osteoclasts are critical during early bone remodeling, because changes in shape are neccessary to maintain normal morphology during growth. For instance, calvarial bone curvature can only expand with the help of osteoclasts absorbing bone on endocranial surfaces while new bone is laid down on the ectocranial surface (Enlow, 2000). Supporting this idea, a relatively large number of osteoclasts are found on the endocranial surface of the calvarial bones during the earliest days of calvarial bone ossification and development (Rice et al., 2000). Assuming that chondroclasts and osteoclasts stem from the same precursor population, circulating monocyte precursors also provide the source for chondroclasts that precede endothelial cells during angiogenesis into the cartilage model of endochondrally formed bones (Lewinson and Silbermann, 1992; Streeten and Brandi, 1990).

Regulatory Interactions Between Epithelial and Osteogenic Cells

Blood vessels do not just provide a conduit through which necessary factors and cell precursors within the circulating blood are delivered to ossification sites, but their endothelial cells are an active part of the regulatory network underlying bone formation and remodeling. This regulatory

network includes endothelial cells, osteoblasts, osteoclasts, macrophages, stromal cells, among other cell types (Collin-Osdoby, 1994; Brandi and Collin-Osdoby, 2006). Previous sections of this paper have introduced factors (e.g. VEGF, HIF) that serve to upregulate endothelial cell migration during angiogenesis, towards populations of hypoxic chondrocytes and into other regions of ongoing osteogenesis. This section focuses on a few regulatory signals that pass from endothelial cells to the osteoblasts and osteoclasts associated with vasculature in these regions.

Endothelial cells, with known proximity to differentiating osteoblasts in newly ossifying bone, produce factors that can regulate differentiation, metabolism, survival, and function of osteoblastic lineage cells (Collin-Osdoby, 1994; Brandi and Collin-Osdoby, 2006). Many of the potential regulatory interactions between these factors and bone cells remain untested, although the addition of endothelial cells into mesenchymal stem cells enhances tissue-engineered bone formation, presumably because of factors expressed by the endothelial cells (Usami et al., 2009). There is also evidence that the production of endothelin-1 may influence osteoprogenitor cell proliferation and differentiation (Von Schroeder et al., 2003). Hypoxia, VEGF, and oscillatory shear stress are known to upregulate BMP-2 in vascular endothelial cells (Bouletreau et al., 2002; Sorescu et al., 2003), which can induce osteoblast differentiation (Yamaguchi et al., 2000), as well as upregulate VEGF expression and angiogenesis during endochondral ossification (Towler, 2008). Further tests of the effects of these and other factors produced by endothelial cells on osteoblast differentiation and behavior of osteoblasts during initial bone formation are necessary to verify their importance.

Endothelial cells are likely to regulate osteoclasts during early skeletogenesis as well. Active time and location dependent regulation of osteoclast movement through the endothelial cell layer is likely necessary for the delivery of osteoclasts to appropriate locations (Parfitt, 2000; Brandi and Collin-Osdoby, 2006). Endothelial cells are known to produce factors that can regulate cells of the

osteoclast lineage, including macrophage-colony stimulating factor and a host of other molecules (Brandi and Collin-Osdoby, 2006). Regardless of the exact ways in which endothelial cells participate in the intercellular regulatory network of skeletogenesis, the close proximity they have to osteoblasts and osteoclasts virtually guarantees that they interact with these cells, beyond allowing for the delivery of factors from the blood supply.

SUMMARY

The craniofacial skeleton houses many important functions associated with the human condition; including cognition, speech, sight, and thermoregulation. Evolutionary modifications associated with changes in these functions and changes in the skull that supports and protects the functioning organs provide important information about our evolutionary history. Evolutionary change of the craniofacial skeleton can only be fully known by understanding the developmental bases of these changes. Here, I specifically examine the role that blood vessel growth (angiogenesis) plays during prenatal intramembranous ossification in an effort to provide new information about the developmental bases of craniofacial evolution. While it is clear that angiogenesis is critical for intramembranous skeletogenesis, studies about the relationship between variation in angiogenesis and variation in the craniofacial skeleton are necessary to elucidate one facet of the palimpsest of craniofacial development.

The following research chapters represent an attempt to document the earliest processes of craniofacial bone ossification, growth, and maturation, with particular emphasis on the role of angiogenesis, in a mouse model with known craniofacial skeletal dysmorphology. Chapter 2 introduces the Apert syndrome *Fgfr2*$^{+/P253R}$ mouse model (Wang et al., 2010) and describes its craniofacial ossification and maturation between embryonic day 15.5 and postnatal day 2, relative to unaffected littermates. Comparisons between individual bone volume and relative density measurements of affected and

unaffected littermates are made in an effort to reveal the earliest stage at which bone development is affected by this mutation. Chapter 3 describes the effort to simultaneously image the blood vessels, bone, and other tissue layers surrounding the developing frontal bone within embryos of Apert syndrome *Fgfr2*$^{+/P253R}$ mice and unaffected littermates. High resolution photoacoustic microscopy and optical coherence tomography images show large embryonic blood vessels and distinguish many major soft tissue layers during the earliest period of frontal bone ossification. Our comparisons represent an attempt to identify associations between known cranial bone dysmorphology and variation in nearby vessels. Chapter 4 introduces a cross of mice that conditionally express the FGFR2 P253R mutation in endothelial cells. These mice were bred to determine what aspects of the known craniofacial dysmorphology of the *Fgfr2*$^{+/P253R}$ mouse model are associated with the expression of the mutation in endothelial cells. Given that Fgf-Fgfr signaling is associated with angiogenesis regulation (Suhardja and Hoffman, 2003; Javerzat et al., 2002), including Fgfr2 (Nakamura et al., 2001), we expect that the process of angiogenesis and therefore osteogenesis are likely to be influenced by this missense mutation. Chapter 5 completes this work by summarizing the important findings of the three studies and discussing their impact within a developmental, evolutionary, and anthropological framework.

CHAPTER 2:
BONE VOLUME AND DENSITY ANALYSIS OF *Fgfr2*$^{+/P253R}$ APERT MODEL MICE

INTRODUCTION

FGF-FGFR Signaling and Development

Fibroblast growth factors (FGF) and receptors (FGFR) are highly pleiotropic, playing critical roles during normal morphogenesis, development, and tissue maintenance. Among many roles, FGF-FGFR signaling is important during the development of limbs (Xu et al., 1999), bone (Hurley et al., 2008), brain (Saarimäki-Vire et al., 2007), kidney (Bates, 2007), lungs (Warburton et al., 2000), lens (Robinson, 2006), and the regulation of the male reproductive system (Cotton et al., 2008). Modifications to FGF-FGFR signaling have been associated with many medical conditions.

In humans, the *FGF* family contains at least twenty-two (although, see Fukumoto, 2008) highly conserved genes, some of which are exclusively expressed prenatally and others which are also expressed postnatally (Ornitz et al., 1996; Chen and Deng, 2005). The *FGFR* gene family consists of four membrane bound receptor tyrosine kinases (*FGFR 1-4*), although *FGFRL1* has been proposed as a fifth member (Trueb, 2011). Alternative splicing leads to two common isoforms for FGFR 1-3 (IIIb and IIIc) (Hou et al., 1991; Werner et al., 1992). For FGFR2, expression of the IIIb isoform is restricted to epithelially derived cells, while IIIc is preferentially expressed in mesenchymally derived cells (Orr-Urtreger et al., 1993; Shi et al., 1994). The FGFRs and their isoforms also tend to be activated by specific FGF ligands. Mesenchymally expressed FGF7 and FGF10 activate only epithelially expressed FGFR2b, while FGF2, 4, 6, 8, and 9 activate FGFR2c (Ornitz et al., 1996;

Igarashi et al., 1998). Cell lineage specific expression of FGFR2 isoforms and FGF ligands, combined with ligand binding specificity of the receptor isoforms gives rise to a system of paracrine signaling between epithelial and mesenchymal tissues, which is critical for normal tissue development (Yu et al., 2000). Many mutations of FGFR receptors have been associated with a breakdown of this signaling system, leading to skeletal dysplasias, including chondroplasias (Ornitz and Marie, 2002; Horton and Lunstrum, 2002) and craniosynostosis syndromes (Wilkie, 1997; Cohen Jr and Maclean, 2000; Passos-Bueno et al., 2008).

Craniosynostosis and Apert Syndrome

FGF-FGFR signaling at calvarial sutures has been associated with the regulation of proliferation of osteoprogenitor cells and their differentiation into osteoblasts (Chapter 1). An appropriate balance of proliferation and differentiation allows for the maintenance of a fibrous suture between adjacent bones, even as they expand (Opperman, 2000; Morriss-Kay and Wilkie, 2005). A change in this balance can lead to premature fusion of sutures, referred to as craniosynostosis; a not uncommon condition with a birth incidence of approximately 300-500 out of 100,000 live births (Cohen Jr and Maclean, 2000). Craniosynostosis occurs as part of over one hundred syndromes and in isolation. Some craniosynostosis syndromes are associated with mutations of *FGFR*, particularly *FGFR2* (Wilkie, 1997; Cohen Jr and Maclean, 2000; Passos-Bueno et al., 2008). Most of the known *FGFR1* and *2* craniosynostosis syndrome mutations lead to constitutive activation of the receptors, although through different mechanisms (Chen and Deng, 2005). These mutations are associated with primary dysmorphology across the body, not just at calvarial sutures, because of the pleiotropic expression of FGFRs.

Apert syndrome, which has a birth incidence of 15.5 in 1,000,000 (Cohen Jr and Maclean, 2000), is primarily associated with two missense mutations of *FGFR2* (Wilkie, 1997). A Ser252Trp

mutation is associated with approximately 66% of Apert syndrome cases, while a Pro253Arg mutation is associated with 32% (Wilkie, 1997; Cohen Jr and Maclean, 2000). These mutations increase the affinity of FGFR2 for FGF ligands (Anderson et al., 1998), although probably by allowing the FGFR2 isoforms to be activated by additional FGFs, allowing autocrine signaling where there had previously only been paracrine signaling (Yu et al., 2000). Patients with Apert syndrome commonly display megalencephaly, coronal craniosynostosis, widely patent midline calvarial defect, and syndactyly of the digits, in addition to a number of less common features. The heads of these patients tend to be shortened along the anteroposterior axis, sometimes slightly widened, and extremely tall (Cohen Jr and Maclean, 2000).

Apert syndrome mouse models with *Fgfr2* mutations orthologous to those associated with Apert syndrome have been produced. All mouse models heterozygous for the Ser252Trp mutation (Chen et al., 2003; Wang et al., 2005) and the Pro253Arg mutation (Yin et al., 2008; Wang et al., 2010; Du et al., 2010) display significantly shortened skulls (rostral-caudal), brachiocephaly, midfacial hypoplasia associated with malocclusion, and premature coronal craniosynostosis. By the first few postnatal days, mouse model skull dysmorphology grossly resembles that of humans with Apert syndrome, while digit syndactyly was only noted in three older $Fgfr2^{+/P253R}$ specimens (Yin et al., 2008). At birth, the coronal, maxillary-zygomatic, and premax-maxillary sutures are commonly fused in mice with both mutations, while the inter-premaxillary suture appears abnormally patent (Wang et al., 2010). The bone fronts bordering the lambdoid and sagittal sutures appear unusually proximate at P0 with ectopic cartilage noted within the posterior sagittal suture (Wang et al., 2005; Wang et al., 2010), while abnormally patent interfrontal sutures (metopic) have been noted in some of the mouse models (Wang et al., 2005; Yin et al., 2008).

Breeding both Apert syndrome mutations on the same inbred C57BL/6J background has

allowed for the identification of precise differences in their influence on development (Wang et al., 2010). At birth, *Fgfr2*$^{+/S252W}$ mice have a more severe reduction in palatal length, particularly for the posterior palate, that leads to greater midfacial hypoplasia and mandibular prognathism than the *Fgfr2*$^{+/P253R}$ mice. On the other hand, the nasal region appears more reduced in *Fgfr2*$^{+/P253R}$ and its cranial base length is significantly reduced compared to littermates, while this is not the case for *Fgfr2*$^{+/S252W}$ (Wang et al., 2010; Martínez-Abadías et al., 2010).

Because calvarial craniosynostosis has historically been considered the primary dysmorphology of Apert syndrome, mesencymal and osteoblast cell activity at the calvarial sutures of these mouse models has been studied in detail. Although increased apoptosis was initially suggested as the basis for coronal synostosis in a *Fgfr2*$^{+/S252W}$ model (Chen et al., 2003), further studies have suggested that early increases in mesenchymal cell proliferation, followed by a decrease in osteoprogenitor proliferation and an increase in osteoblast differentiation leads to unusually proximate osteogenic fronts at the basal coronal suture by E13.5 and osteoid fusion by E15.5-E16.5, while apoptosis at the coronal suture is a result rather than a cause of synostosis (Holmes et al., 2009; Wang et al., 2010). Coronal fusion towards the apex of the head occurs at a slower rate and may occur at the expense of cell proliferation (Holmes et al., 2009). Increased proliferation and abnormal differentiation at the sagittal suture lead to more proximate parietal bone fronts at the sagittal suture, while increased proliferation and an altered distribution of proliferating cells leads to more distant frontal bone fronts at the interfrontal suture (Wang et al., 2005). That the influence of these *Fgfr* mutations might vary by suture suggests that their influence on cell activity may vary across the skull. Additionally, variation is noted in the timing and level of coronal fusion (Holmes et al., 2009; Martínez-Abadías et al., 2010), which highlights the stochastic nature of the cellular processes being modified and the fact that the dysmorphology associated with these mutations are not accurately represented as binary traits.

Although coronal craniosynostosis is commonly cited as the primary dysmorphology of the Apert mutations, the facial skeleton (Martínez-Abadías et al., 2010) and brain are also primarily affected (Aldridge et al., 2010; Hill et al., 2013). In addition to the influence of these mutations on cranial intramembranous osteogenic processes, long bone epiphyseal ossification (Wang et al., 2005; Yin et al., 2008; Wang et al., 2010) and endochondral ossification of the cranial base (Yin et al., 2008; Wang et al., 2010) are also affected by the mutations. A recent study has suggested that the primary influence of the Apert mutation on cranial base chondrogenesis might actually lead to craniosynostosis secondarily (Nagata et al., 2011; although see Holmes and Basilico, 2012). Clearly, to understand the broad influence of these *Fgfr2* mutations on craniofacial phenotypes requires looking at developmental processes across the skull and other tissues. The results of a study on early postnatal bone maturation of a mouse model of FGFR2 associated Beare-Stevenson craniosynostosis syndrome (Percival et al., 2012) highlights the importance of data obtained by quantifying skeletal phenotypes across the skull.

Study Introduction

In this study, we quantify the volume and relative bone density of individual craniofacial bones from late embryonic and early postnatal *Fgfr2*$^{+/P253R}$ mouse specimens (Wang et al., 2010) and their unaffected littermates. The measurements from the unaffected littermates define the baseline "normal" pattern of bone growth and maturation. Comparison with measurements of *Fgfr2*$^{+/P253R}$ mice were used to determine how the growth of individual craniofacial bones is affected between E15.5 and P2. Previous analysis of *Fgfr2*$^{+/P253R}$ embryos indicate that mutants can be identified as early as E16.5 by their relatively domed heads (Yin et al., 2008), that coronal fusion is evident along with changes in cell activity during the embryonic period and that skull size is smaller by birth (Holmes et al., 2009; Wang et al., 2010). Therefore, we hypothesize that the individual bones of *Fgfr2*$^{+/P253R}$ mice will display reduced bone volume and relative bone mineral density during the embryonic period.

Although dysmorphology may be more apparent in the facial skeleton, dysmorphology appears across the skull of *Fgfr2*$^{+/P253R}$ mice (Martínez-Abadías et al., 2010; Du et al., 2010). Additionally, both intramembranous and endochondral ossification processes are known to be influenced by the P253R mutation (Yin et al., 2008; Wang et al., 2010). For these reasons, and because of evidence that early postnatal cell activity is similarly affected in all craniofacial bones of *Fgfr2*$^{+/Y394C}$ Beare Stevenson cutis gyrata mice (Percival et al., 2012), we expected the P253R mutation to similarly influence the maturation of all craniofacial bones during late prenatal and early postnatal development.

METHODS

Sample and Imaging

Mouse heterozygotes with neo (+/P253Rneo) (Wang et al., 2010) were mated with EIIA promoter Cre transgenic mice (EIIA-Cre, The Jackson Laboratory) to remove the neo cassette and allow heterozygous expression of the *Fgfr2* P253R mutation in all tissues from the preimplantation stage onward. Resulting litters were composed of approximately half *Fgfr2*$^{+/P253R}$ heterozygote mutant mice and half *Fgfr2*$^{+/+}$ unaffected littermate controls. Based upon timed matings and evidence of pregnancy, litters were sacrificed at prenatal days E14.5, E15.5, E16.5, E17.5 and postnatal days P0 and P2. Many of the E14.5-E16.5 embryos were also used to study the association between angiogenesis and osteogenesis near the ossifying frontal bone (Chapter 3), while the E17.5, P0, and P2 mice used here are included in the samples used in previous landmark based morphometric analyses (Wang et al., 2010; Martínez-Abadías et al., 2010; Hill et al., 2013; Motch et al., 2012). After sacrifice, specimens were fixed in 4% paraformaldehyde and stored in 0.01 M phosphate buffered saline with sodium azide as an antibacterial agent. Care and use of mice for this study were in compliance with relevant animal welfare guidelines approved by Johns Hopkins University, Mount Sinai School of Medicine, and Pennsylvania State University Animal Care and Use Committees.

High resolution micro-computed tomography (HRCT) images of mouse heads (Table 2.1) were acquired in air at the Center for Quantitative X-Ray Imaging at Pennsylvania State University (www.cqi.psu.edu) using an OMNI-X Universal HD600 industrial x-ray computed tomography system (Varian Medical Systems, Palo Alto CA). Solid hydroxyapatite phantoms (QRM GmbH, Möehrendorf, Germany) scanned with each set of skulls allowed us to linearly associate relative x-ray attenuation values with bone mineral density estimates (Fig 2.1).

Because C57BL/6 mice, the background of our mouse model, first exhibit craniofacial ossification in cleared and Alizarin red stained specimens at E14.5, we attempted to identify mineralized cranial tissue in the HRCT images of E14.5 specimens, but no bone was detected. This is likely because the Alizarin red staining identifies early calcium deposition, while the HRCT requires a relatively high level of ossification before bone can be identified. So, we quantified the craniofacial development of mice aged E15.5 and older (Table 2.1).

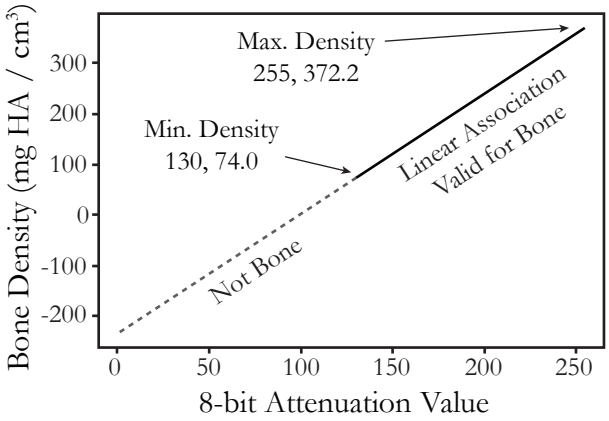

Fig 2.1 The linear association between 8-bit voxel attenuation values and estimated bone mineral density (partial density of hydroxyapatite), based on regression from HRCT images of solid hydroxyapatite phantoms. This association is invalid for voxels that do not actually represent bone (below our minimum threshold). The voxels with the highest attenuation values may include portions of bone with density above the value of 372.2 mg HA/cm^3, because of image saturation.

Table 2.1 Sample sizes of *Fgfr2*$^{+/P253R}$ and *Fgfr2*$^{+/+}$ mice for all five age categories and the associated resolution of their HRCT images.

Age	# of Fgfr2$^{+/+}$ Specimens	# of Fgfr2$^{+/P253R}$ Specimens	voxel width (mm)	slice thickness (mm)
E15.5	7	7	0.011	0.013
E16.5	16	9	0.011	0.013
E17.5	7	9	0.014	0.015
P0	14	11	0.015	0.016
P2	8	5	0.015	0.016

Bone Volume and Density Histograms

Using tools within Avizo 3D analysis software (Visualization Sciences Group, Burlington, MA, USA), craniofacial bones with a minimum of 74.0 mg/mm^3 partial density of hydroxyapatite were manually identified (segmented) from HRCT images of E15.5, E16.5, and E17.5 skulls. Manual segmentation minimizes segmentation error associated with the relatively low levels of ossification within embryonic bones. Craniofacial bones of the larger and more highly ossified P0 and P2 specimens were segmented using a modified version of a previously described semi-automatic segmentation method (Percival et al., 2012). After removing postcranial bones and patches of noise from P0 and P2 HRCT images, we manually identified the individual craniofacial bones of reference specimens for each of the four postnatal age and genotype combinations. Reference specimen bone labels, representing the theoretical space that a bone from any specimen of the same age-genotype category might occupy in a standard orientation, were registered to each associated target specimen in order to identify the extent of each individual craniofacial bone. After segmentation of specimens of all ages, a histogram of all bone density values above the minimum bone threshold was calculated for each identified bone, instead of volume measurements based on three minimum bone densities as studied previously (Percival et al., 2012). The resulting histograms span 126 density values from 74.0 to 372.2 mg/mm^3 partial density of hydroxyapatite (Fig 2.2). Because of image saturation for some bones of the older specimens, the highest density values may include volumes of bone above the maximum density value. The sum of all histogram values of a single bone multiplied by voxel size is an estimate of bone volume, while a curve derived from the histogram represents bone mineral density.

Measurements from 16 bones serve as the basis of our analysis (Fig 2.3); interparietal (IPar), squamous occipital (SquO), lateral occipital (LatO), basioccipital (BasO), parietal (Par), squamous temporal (SquT), frontal (Fro), maxilla including lacrimal (Max), nasal (Nas), premaxilla (PMax), palatine

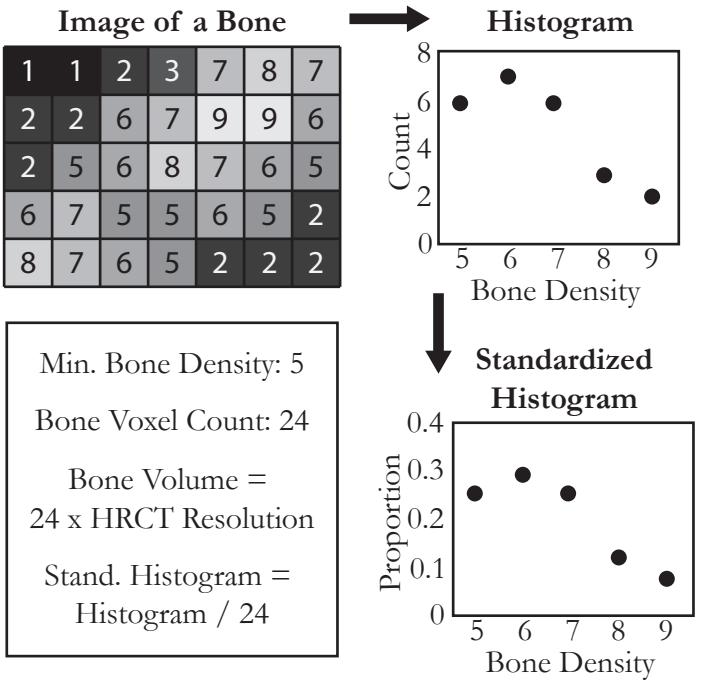

Fig 2.2 Based on a minimum bone density value, a bone density histogram (histogram) is calculated from the number of voxels of each bone density value in an HRCT image of a bone. A standardized bone density histogram (standardized histogram) is calculated by dividing the histogram by the total number of voxels above the minimum bone density value. Total bone volume is calculated as the total number of voxels multiplied by the resolution of the HRCT image. All values in this figure were chosen arbitrarily for the purposes of this hypothetical example.

including pterygoid (Pal), presphenoid (PSph), sphenoid ala (SphA), sphenoid body (SphB), petrous temporal (PetT), and mandible (Man). Because of variation in systematic semiautomatic segmentation error associated with the use of specific reference specimens and because bilateral bones display very similar bone density histograms within specimens, measurements used for analysis may come from the left side of specimens sharing one age-genotype combination and from the right side of specimens sharing another. Teeth were not segmented during manual segmentation of embryonic specimens to avoid confounding them with surrounding bone. For older specimens, teeth were manually segmented independently and their density histograms were subtracted from associated bone density histograms before analysis.

Total individual bone volumes, the sum of histogram values for all densities multiplied by the HRCT image resolution, were compared between the genotypes for each age category with 2-sample Wilcoxian (Mann-Whitney) tests (α=0.05), including Bonferroni correction for multiple testing, in R (R Developmental Core Team, 2008). Mean total bone volumes, calculated for each age-genotype combination, serve as a proxy for bone size, while differences in volume between ages represent bone

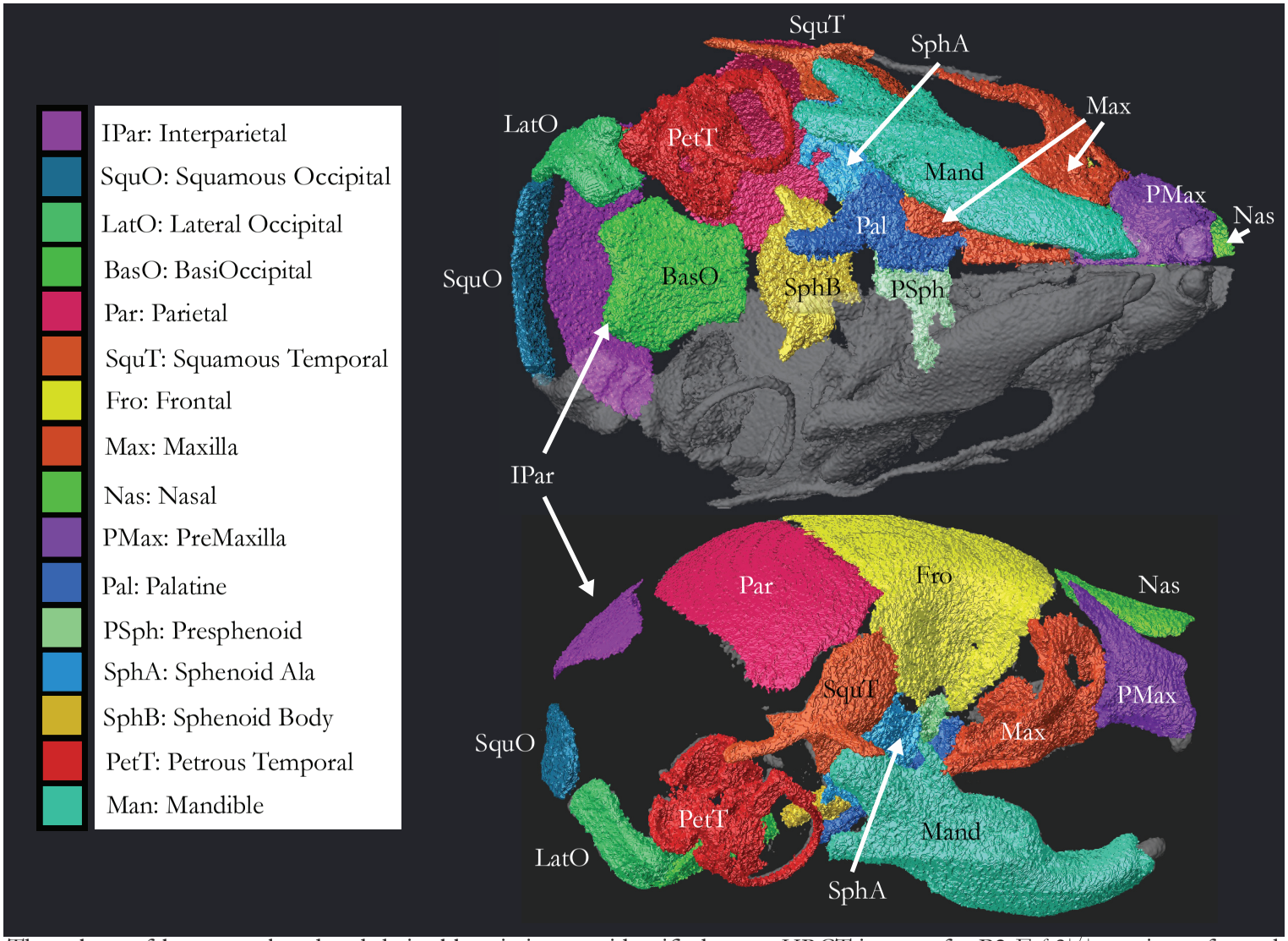

Fig 2.3 The subset of bones analyzed and their abbreviations, as identified on an HRCT image of a P2 *Fgfr2*$^{+/+}$ specimen from the inferior view (top) and the right lateral view (bottom). Bones being analyzed are brightly colored, while the rest of the skull is transparent grey. Bone abbreviations and associated colors defined here will be used throughout the text and figures of this chapter. Although the right side of each pair of bilateral bones is highlighted here, the left side of some of these bones were chosen for analysis of some age-genotype categories.

growth. Mean volumes standardized by the total bone volume of the 16 bones under study represent relative bone development for each age-genotype combination.

Standardized bone density histograms were calculated for each specimen by dividing each entry of the voxel count filled bone density histograms by the total number of voxels associated with that bone (Fig 2.2). This standardizes voxel counts by total bone volume, removing variation associated with differences in scale. Mean standardized bone density histograms were calculated for the bones of each age-genotype combination. The changes in *Fgfr2*$^{+/+}$ mean standardized histograms for a bone across ages represent the expected "normal" pattern of bone maturation. Mean standardized bone density histograms were plotted to compare the speed and nature of bone maturation between the bones.

Using the *Fgfr2*$^{+/+}$ standardized bone density histograms as a baseline, functional analysis was performed, using the fda library in R (Ramsay et al., 2009), to determine the influence of the P253R mutation on bone maturation across the earliest stages of craniofacial ossification. Because image saturation in some bones of the older specimens would have a strong artificial influence on functions estimated from histograms, the five highest bone density values were not included in functional analysis. Using the remaining 121 values from the standardized histograms, cubic spline functions were estimated for each bone using 5 knots. A functional multivariate regression was computed for each bone with age as a numerical covariate, genotype as a binary covariate, and with an optional age*genotype interaction term.

Regressions completed for each bone:

$$E[y_i(d)) = \beta_0(d) + \beta_1(d)\, Genotype + \beta_2(d)\, Age$$

$$E(y_i(d)) = \beta_0(d) + \beta_1(d)\, Genotype + \beta_2(d)\, Age + \beta_3(d)\, Int_{Genotype,\, Age}$$

Table 2.2 Bones for which ossified portions can be identified from HRCT images of all specimens at a given age (white), some specimens (grey), or no specimens (black). Bone abbreviation definitions defined in Fig 2:3.

Bones	E15.5	E16.5	E17.5	P0	P2
IPar					
SquO					
LatO					
BasO					
Par					
SquT					
Fro					
Max					
Nas					
PMax					
Pal					
PSph					
SphA					
SphB					
PetT					
Man					

In these models, *d* refers to bone density values. Multivariate regressions of curves from all 5 ages, of prenatal curves (E15.5-P0), and of postnatal curves (P0, P2) were computed in order to identify differences in the effects of the P253R mutation before and after birth. For each individual bone regression, ages were only included when that bone was noted in all specimens of the sample for that age (Table 2.2). 95% confidence intervals of the resulting coefficient curves were computed to determine whether the effect of the associated covariate was significant. Plots displaying the standardized density curves for all specimens of single ages were produced for bones with significant genotype effects or close to significant effects to get a better idea of the influence of the P253R mutation on bone maturation.

RESULTS

Volume Analysis

Ossified portions of each bone were identified from HRCT images of each specimen to reveal the location of early ossification and patterns of bone expansion. Some bones display gross differences in extent and shape between *Fgfr2*$^{+/P253R}$ and *Fgfr2*$^{+/+}$ specimens (Figs 2.4-2.7). The ossified volume of the skull increases every day between E15.5 and P2 (Fig 2.8), with no significant difference

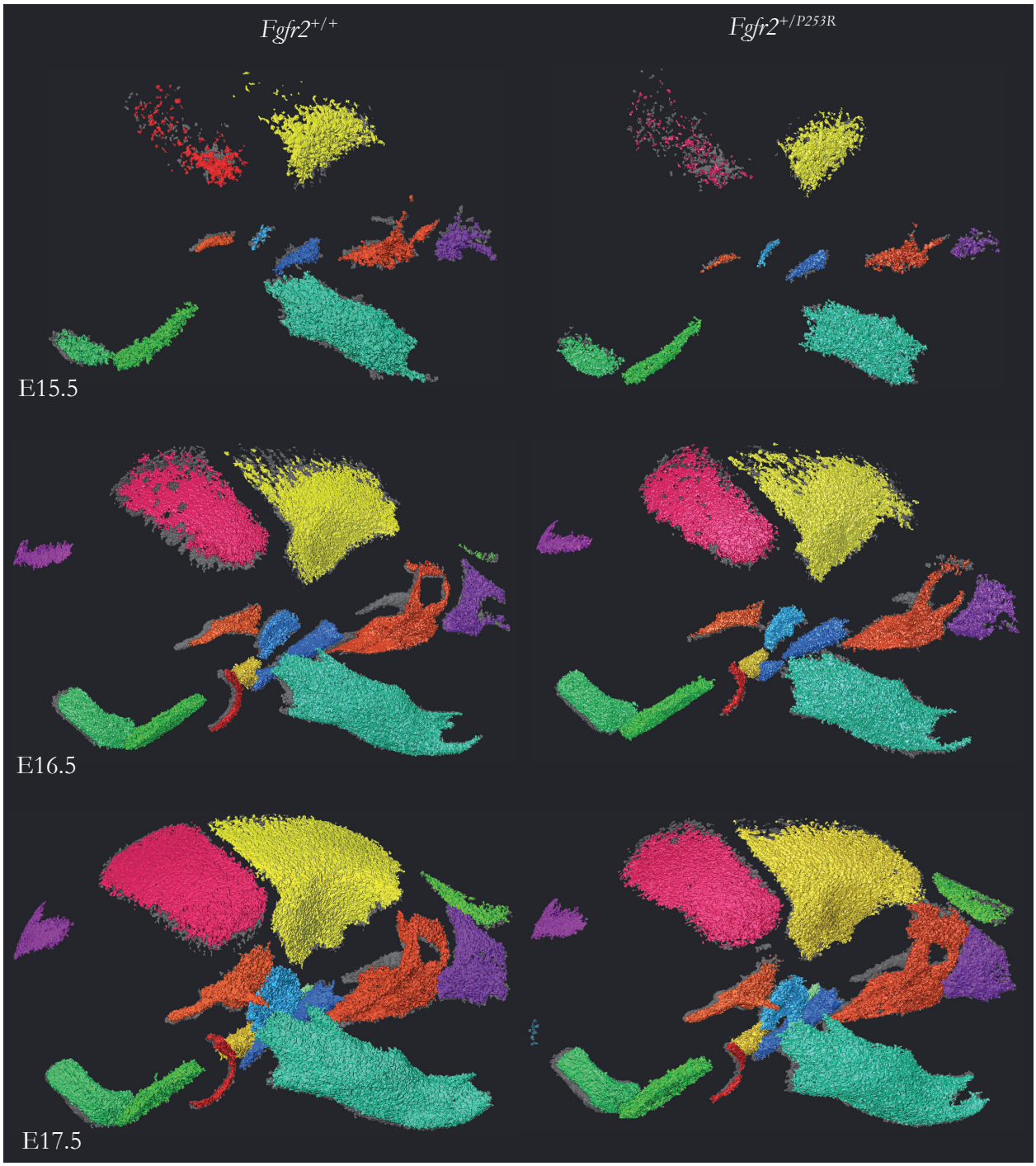

Fig 2.4 Bones of analysis identified from the right lateral view of HRCT images of representative specimens of each embryonic age-genotype category. Bones being analyzed are brightly colored, while the rest of the skull is transparent grey. There are some noticeable differences in individual bone volume and extent between the genotypes of a given age. See Fig 2.5 for identical images of postnatal specimens. Bones are identified in Fig 2.3. The anterior aspect of the skulls is to the right and the superior aspect is towards the top of the page. Images are not to scale.

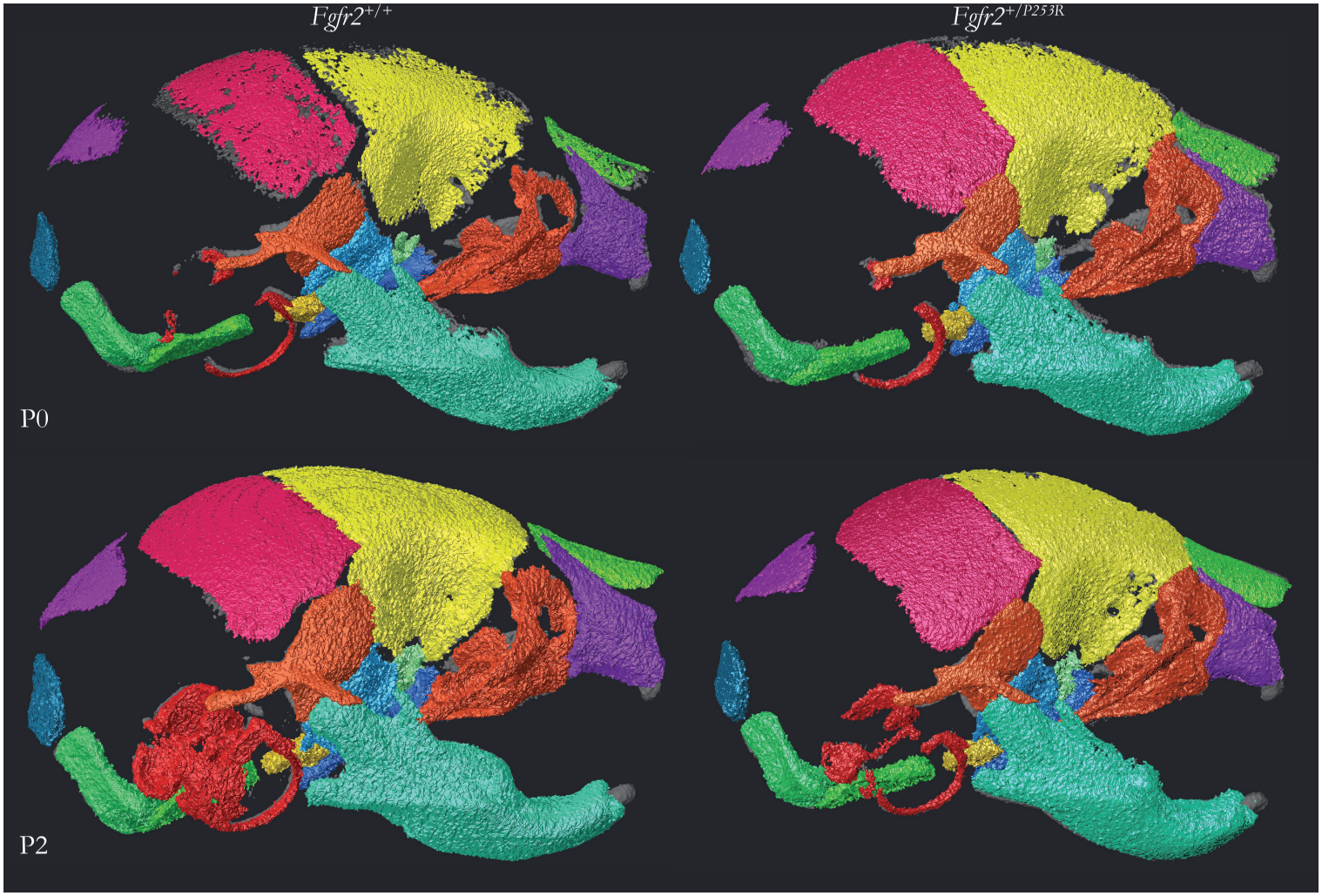

Fig 2.5 Bones of analysis identified from the right lateral view of HRCT images of representative specimens of each postnatal age-genotype category. Bones being analyzed are brightly colored, while the rest of the skull is transparent grey. There are some noticeable differences in individual bone volume and extent between the genotypes of a given age. In addition, there is evidence of midfacial hypoplasia as well as premature fusion of the coronal and various facial sutures in the $Fgfr2^{+/P253R}$ specimens. See Fig 2.4 for identical images of embryonic specimens. Bones are identified in Fig 2.3. The anterior aspect of the skulls is to the right and the superior aspect is towards the top of the page. Images are not to scale.

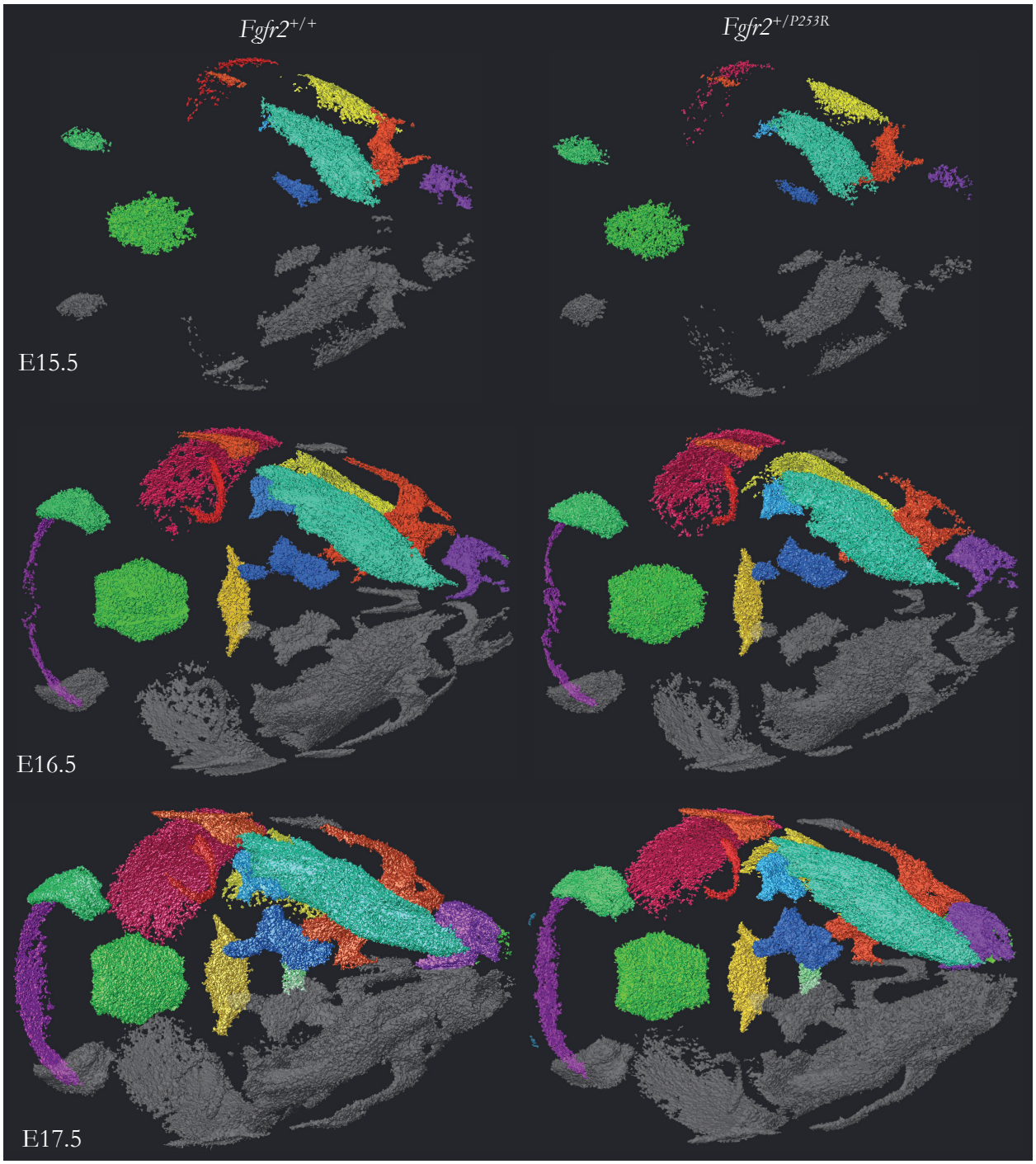

Fig 2.6 Bones of analysis identified from the inferior view of HRCT images of representative specimens of each embryonic age-genotype category. Bones being analyzed are brightly colored, while the rest of the skull is transparent grey. There are some noticeable differences in individual bone volume and extent between the genotypes of a given age. See Fig 2.7 for identical images of postnatal specimens. Bones are identified in Fig 2.3. The anterior aspect of the skulls is to the right and the right lateral aspect is towards the top of the page. Images are not to scale.

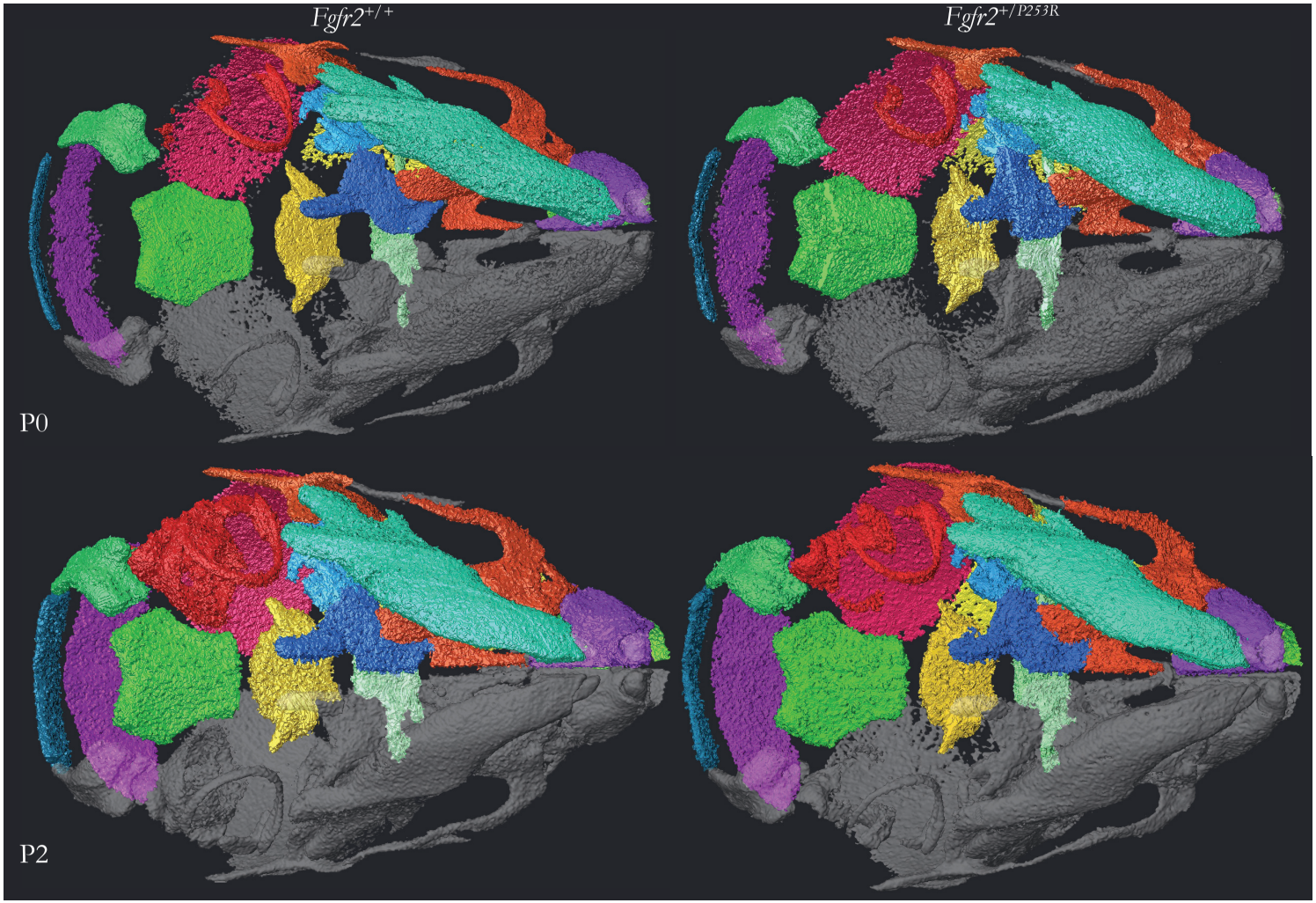

Fig 2.7 Bones of analysis identified from the inferior view of HRCT images of representative specimens of each postnatal age-genotype category. Bones being analyzed are brightly colored, while the rest of the skull is transparent grey. There are some noticeable differences in individual bone volume and extent between the genotypes of a given age. In addition, there is evidence of midfacial hypoplasia in the $Fgfr2^{+/P253R}$ specimens. See Fig 2.6 for identical images of embryonic specimens. Bones are identified in Fig 2.3. The anterior aspect of the skulls is to the right and the right lateral aspect is towards the top of the page. Images are not to scale.

in overall volume between the genotypes at any age. The proportional mean volume of individual elements varies between ages, representing a larger part of total ossified volume at some ages (Fig 2.9).

The volume of specific elements differ between genotypes at some ages, with differences that are significant before (*****) and after correction for multiple testing (******) reported separately, but together suggesting strong trends (Fig. 2.10). At E15.5, *Fgfr2*$^{+/P253R}$ mice display non-significantly lower mean volumes than *Fgfr2*$^{+/+}$ mice across all relatively well ossified bones (Fig 2.10A). Importantly, removing a single *Fgfr2*$^{+/P253R}$ mouse of particularly high ossification from the sample makes the volumes of SquT*****, Max*****, and PMax***** significantly lower for *Fgfr2*$^{+/P253R}$ mice, revealing the effects of strong intra group variation on analytical results. The bones of E16.5 *Fgfr2*$^{+/P253R}$ mice have lower or similar mean volumes compared to *Fgfr2*$^{+/+}$ (Fig 2.10A), with SquT******, PMax******, Max*****, PetT*****, and Man***** volumes being significantly lower. At E17.5, bone volumes are not significantly different between the genotypes (Fig 2.10A). P0 *Fgfr2*$^{+/P253R}$ mice display higher mean volumes than *Fgfr2*$^{+/+}$ for some bones and lower for others, with Max***** being significantly higher and SquO***** significantly lower (Fig 2.10B). At P2, IPar******, SquO*****, Par*****, SquT*****, SphA*****, and SphB***** volumes are significantly reduced in *Fgfr2*$^{+/P253R}$ mice (Fig 2.10B). The differences for SphA and SphB at P2 should be accepted with caution, because of acute error in the semiautomatic segmentation of the palate and rostral cranial base for P2

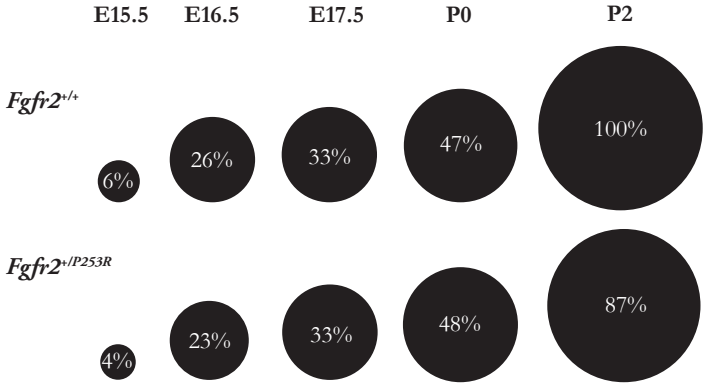

Fig 2.8 Circles illustrating the mean total bone volume of each age-genotype category in relation to the P2 *Fgfr2*$^{+/+}$ value. The area of the circle is proportional to mean total bone volumes and represent the relative scale of the pie charts found in Fig 2.9. These values differ strongly across ages, but also appear to differ between genotypes at some ages, suggesting a relatively lower degree of bone maturation for *Fgfr2*$^{+/P253R}$ mice at E15.6, E16.5, and P2.

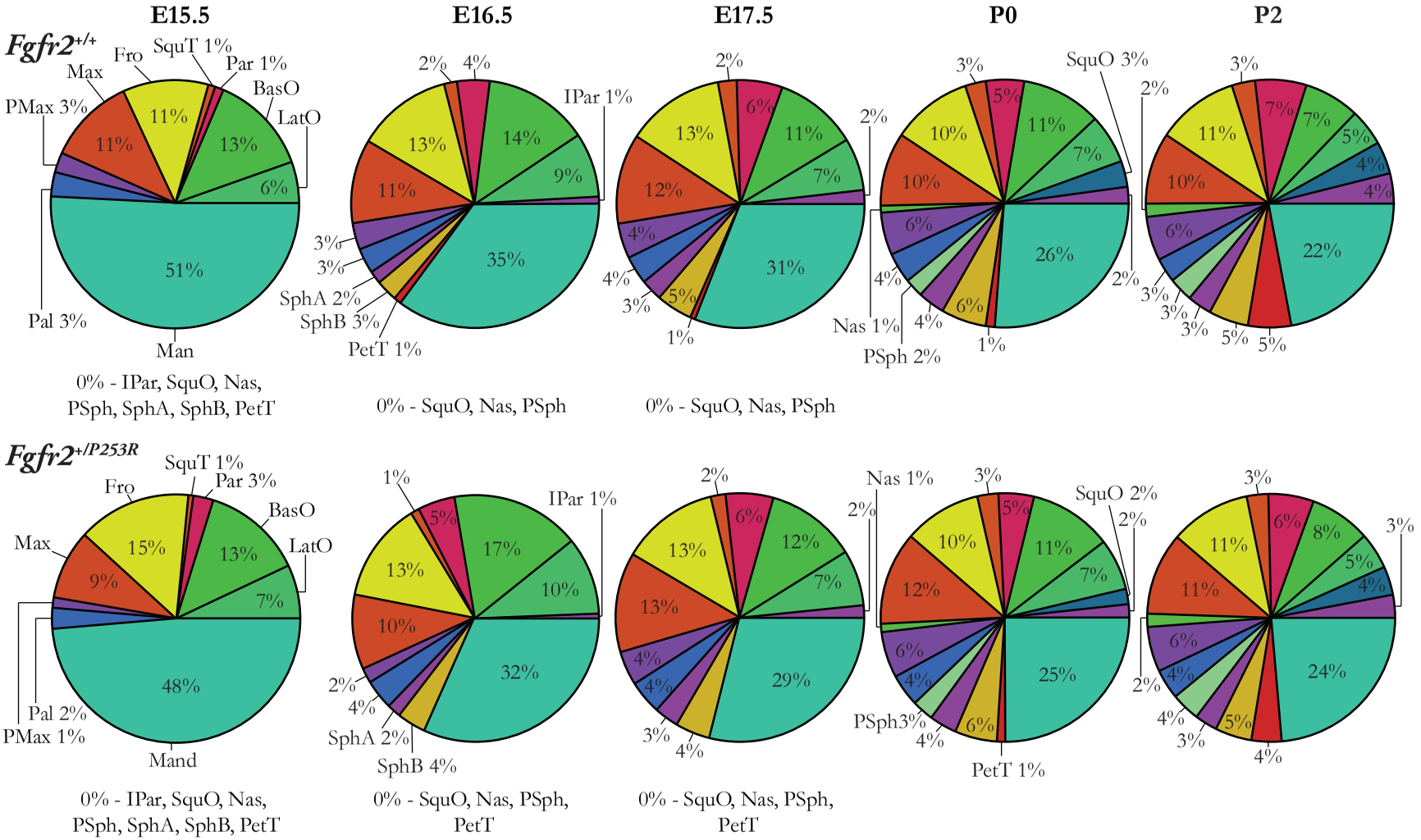

Fig 2.9 Pie charts illustrating the mean relative volume of each bone under analysis compared to the mean total volume of all bones under analysis for each age-genotype combination. The differences in relative individual bone volume are stronger between ages than between genotypes within an age category. See Fig 2.8 for an illustration of differences in scale of these pie charts. Percentage values are rounded, so some specimens may have a bone with small volume, although the bone is listed as zero percent. Bone abbreviations are defined in Fig 2.3.

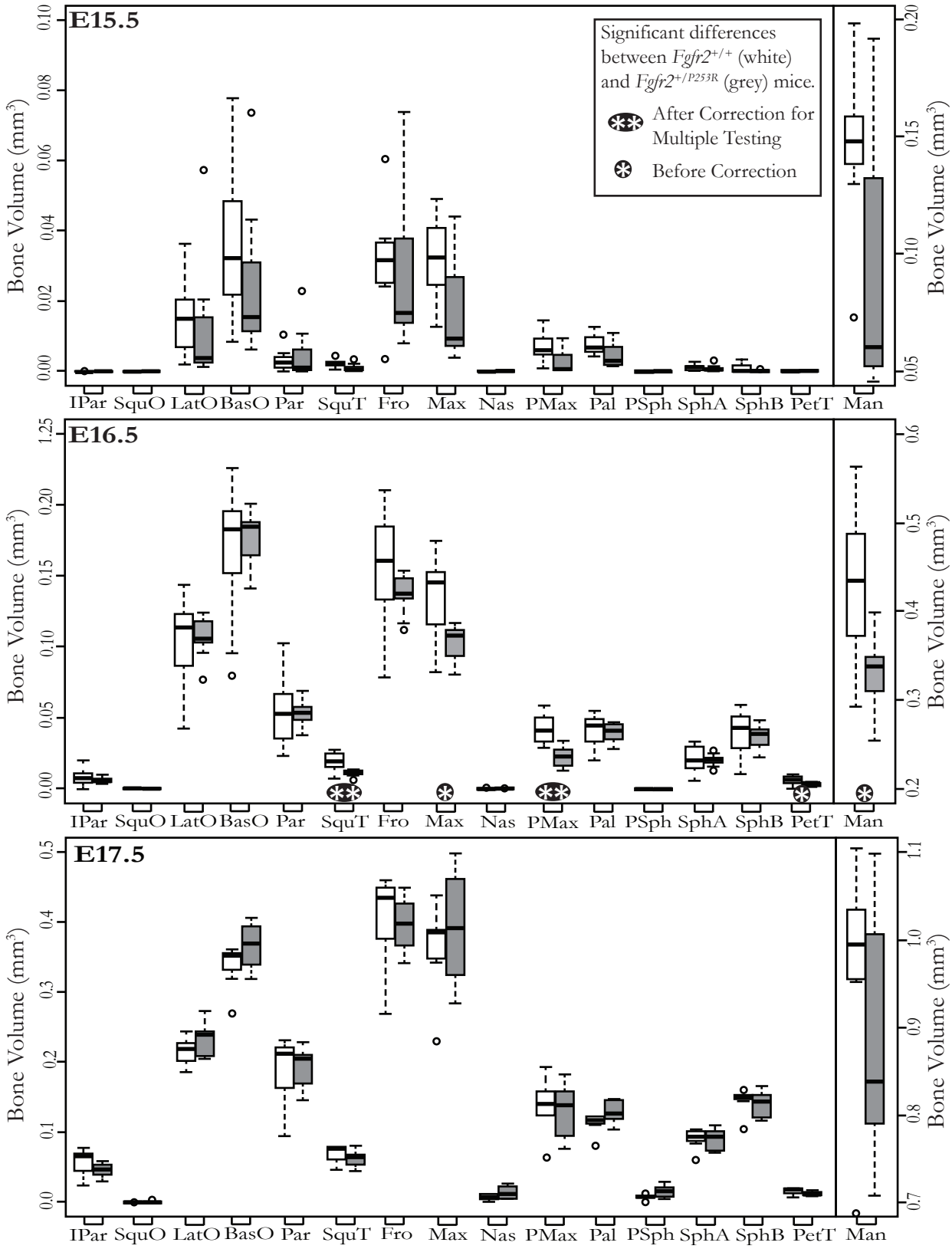

Fig 2.10A Caption on the next page

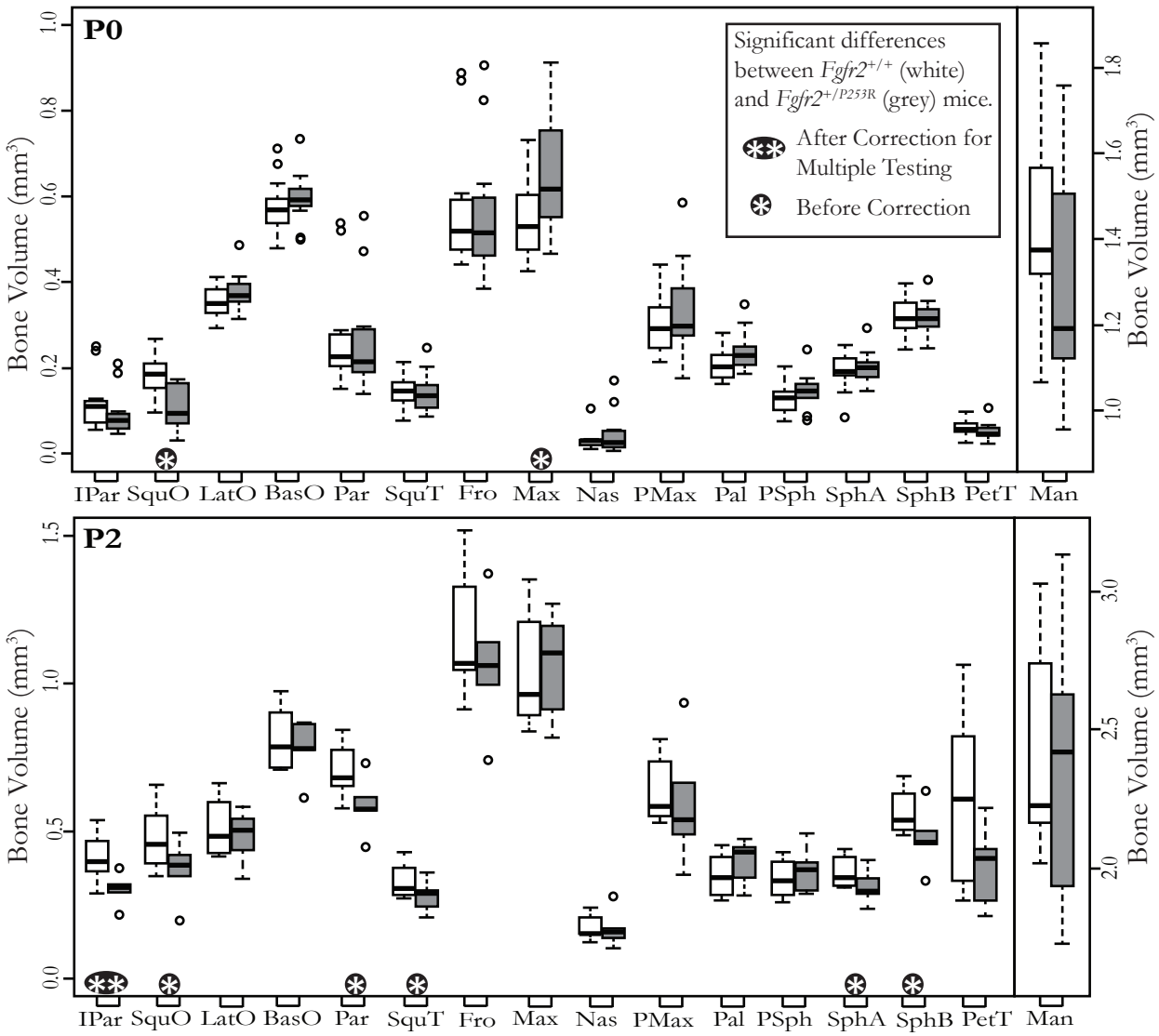

Fig 2.10B Boxplots of bone volumes by age, comparing the bone volume distributions for each bone between the two genotypes at (A; previous page) E15.5, E16.5, E17.5 and (B; this page) P0, P2. White boxes represent *Fgfr2*$^{+/+}$ and grey boxes represent *Fgfr2*$^{+/P253R}$. Dots represent outlier values that are more than 1.5 times the interquartile range from the box. The values for mandible (Man) are always at a different scale than the other bones within an age. ******Significant differences in two-sample Wilcoxon tests of volume values between mutant mice and unaffected littermates. *****Differences in the same tests that were significant prior to correction for multiple comparisons. Bone abbreviations are defined in Fig 2.3.

Fgfr2$^{+/P253R}$ specimens (see Discussion).

Histogram Analysis

Mean standardized bone density histograms of *Fgfr2*$^{+/+}$ mice, representing each age of a given bone, were plotted together to illustrate typical changes in relative bone mineral density. Most bones

display very low relative density at E15.5, but mature in one of three ways (Fig 2.11). Group 1 (continuous increase) bones display a consistent and continuous change from low relative bone density to higher density across the age range and include BasO, LatO, SphB, SquO, and PSph (Fig 2.12). Group 2 (medium density) bones, Fro, Pal, Max, Man, SquT, and SphA, display an intermediate relative bone density from E16.5 to P2, with limited change (Fig 2.13). Group 3 (low density) includes IPar, Par, PetT, Nas, and PMax, which retain a low relative bone mineral density until the postnatal period, when increase in relative density often occurs between P0 and P2 (Fig 2.14). A strong increase between P0 and P2 is particularly apparent for bones of group 3, but not limited to this group.

Functional multivariate regressions indicated that age and genotype are significant factors in influencing relative bone density, as measured from standardized histogram curves. The addition of an interaction term in the regressions did not have much of an effect, so we report the results of the regressions without

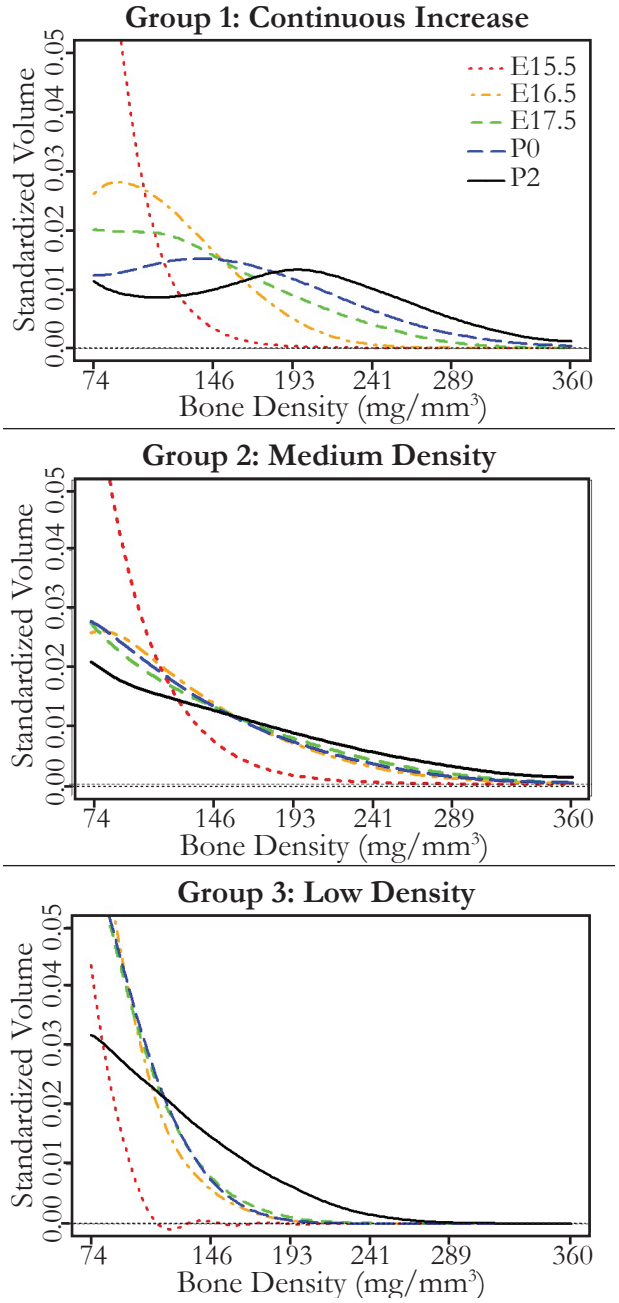

Fig 2.11 Mean standardized bone density curves for *Fgfr2*$^{+/+}$ specimens at each age, representing three patterns of bone maturation. The axis scales are standardized across plots to allow for easy comparison, but forcing high standardized volume values off the plots. Bone density is measured as mg/mm^3 partial density of hydroxyapatite. See Fig 2.12-2.14 for equivalent plots of all bones in the three groups.

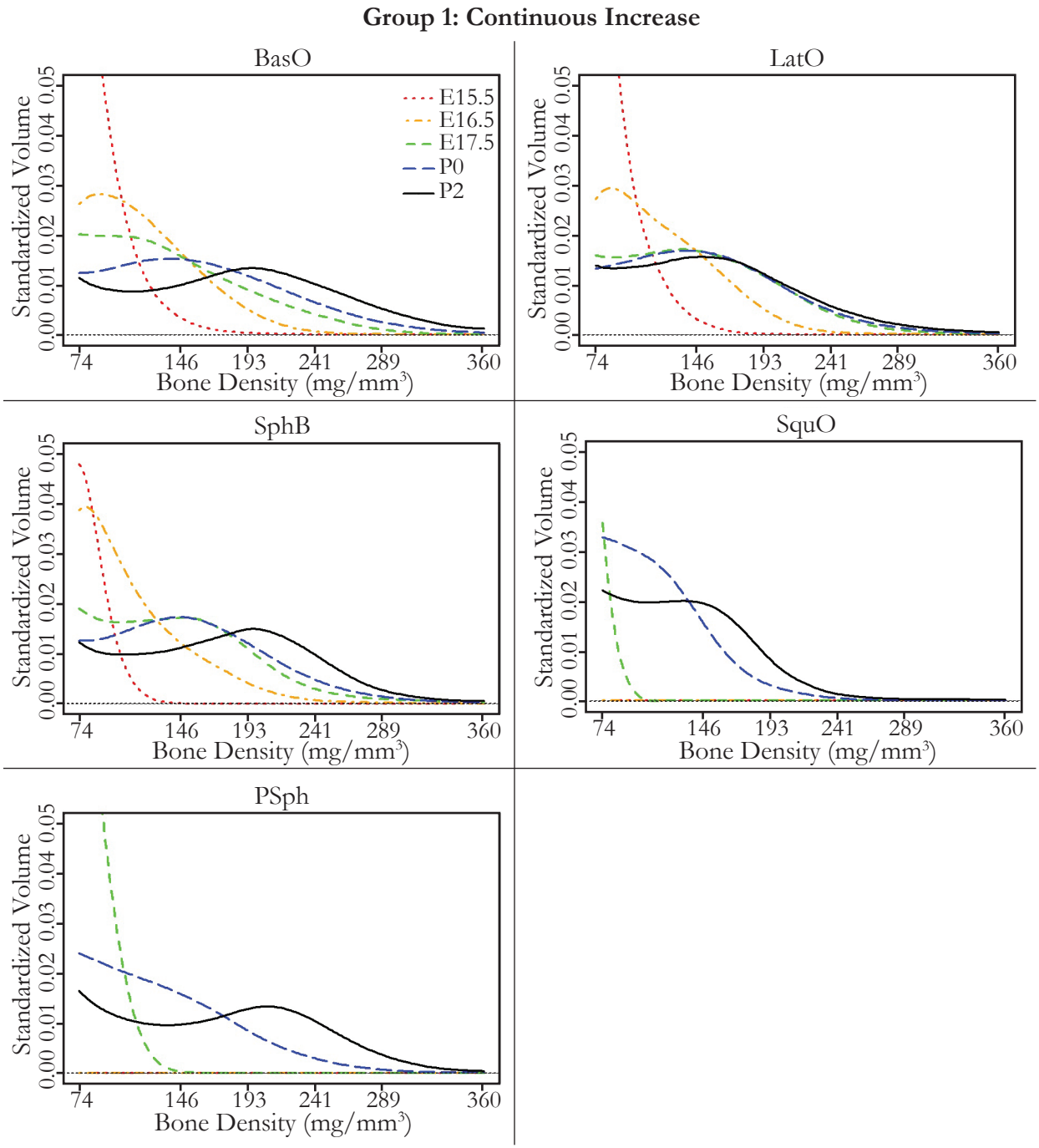

Fig 2.12 Mean standardized bone density curves for *Fgfr2*$^{+/+}$ specimens, representing bones that mature quickly through continuous relative density increase between E15.5 and P2 (Group 1). The axis scales are standardized across plots to allow for easy comparison, but forcing high standardized volume values off the plots. Bone density is measured as mg/mm^3 partial density of hydroxyapatite. Bone abbreviations defined in Fig 2.3.

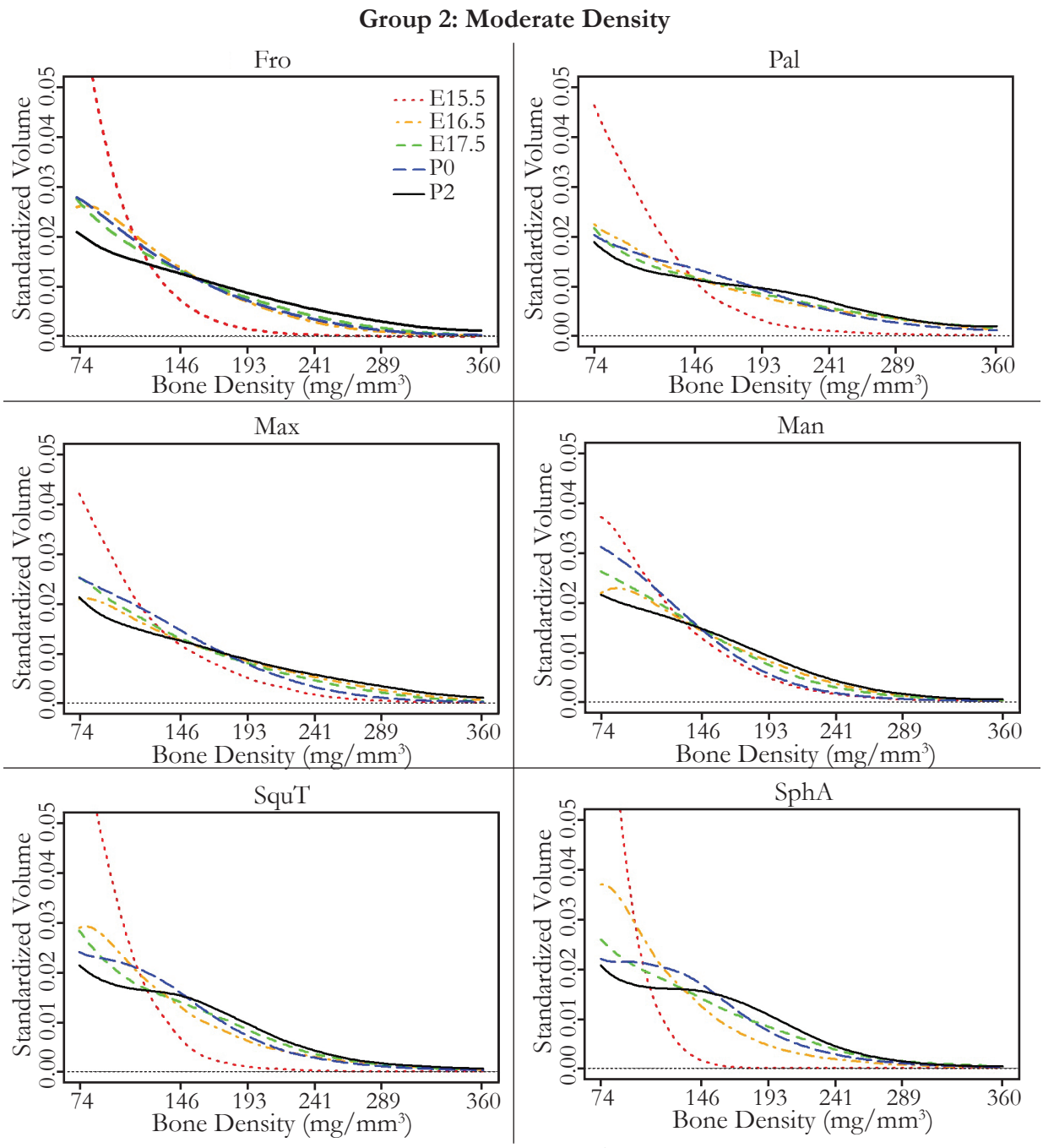

Fig 2.13 Mean standardized bone density curves for *Fgfr2*$^{+/+}$ specimens, representing bones that retain a moderate relative bone density between E16.5 and P2 (Group 2). The axis scales are standardized across plots to allow for easy comparison, but forcing high standardized volume values off the plots. Bone density is measured as mg/mm^3 partial density of hydroxyapatite. Bone abbreviations defined in Fig 2.3.

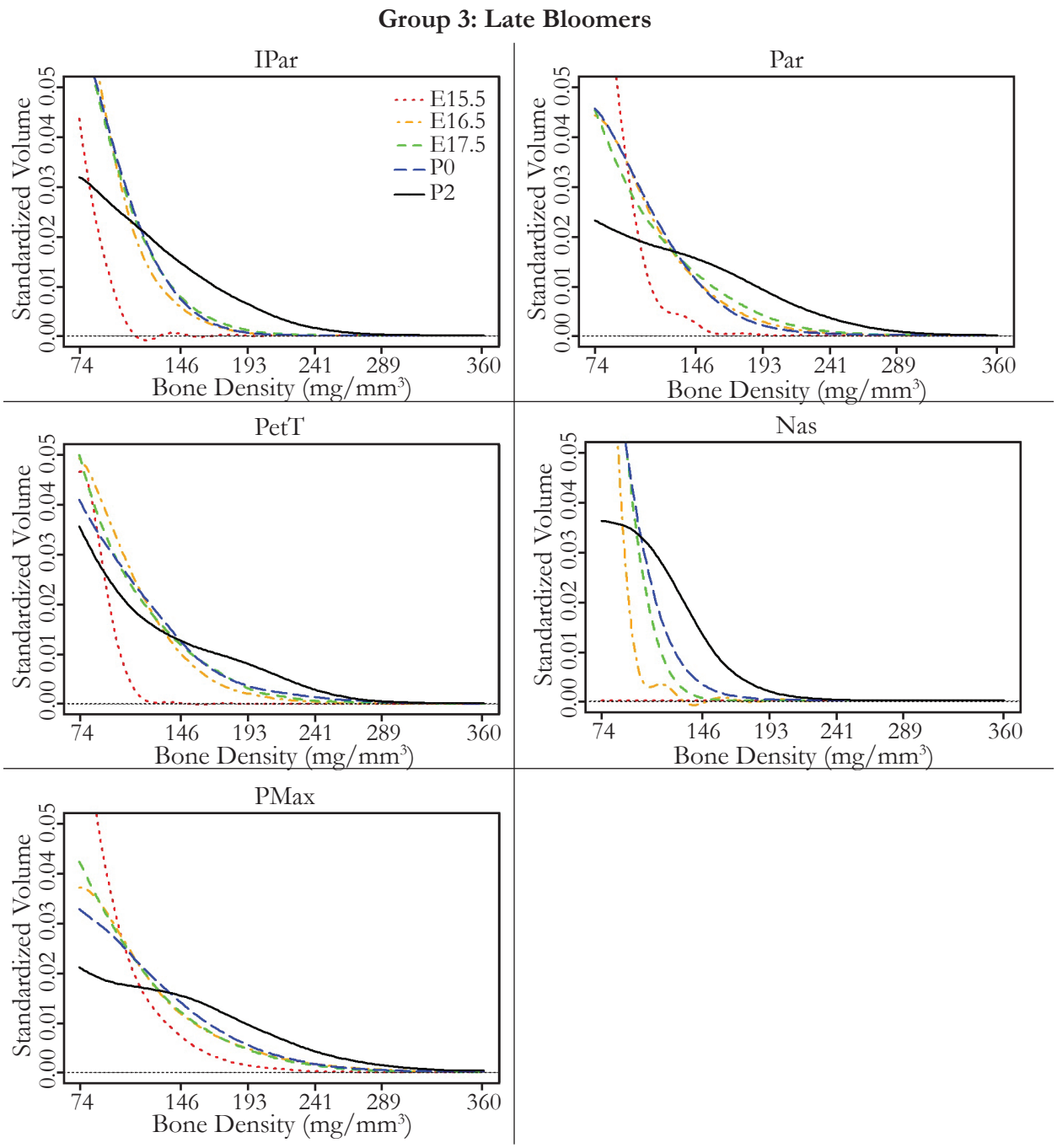

Fig 2.14 Mean standardized bone density curves for *Fgfr2*$^{+/+}$ specimens, representing bones that retain a low relative bone density until a postnatal increase in relative bone density (Group 3). The axis scales are standardized across plots to allow for easy comparison, but forcing high standardized volume values off the plots. Bone density is measured as mg/mm^3 partial density of hydroxyapatite. Bone abbreviations defined in Fig 2.3.

the interaction term. Most bones show a significant age effect for which the proportion of low density bone strongly decreases with age and the proportion of higher density bone increases with age more subtly (Figs 2.15-2.16). For the prenatal regression, IPar, Man (Fig 2.15D), PetT, and Max do not display or display weakly significant age effects. Based on the regression between P0 and P2, LatO (Fig 2.16C) does not display a significant age effect over the first postnatal days, while the other bones display generally wide, but varying ranges of bone values. Bones that typically display more obvious changes in relative density curves and more high density bone (Figs 2.11-2.14) tend to have age effect coefficients that remain significant across a wider range of values (Figs 2.15-2.16).

In all cases of a significant effect of genotype on bone maturation, the influence of the P253R mutation is similar to a reduction in the age variable; the proportion of lower density bone increases as the proportion of higher density bone decreases. Based on the prenatal regression, genotype has a significant effect on standardized density curves for Man (Fig 2.15D), Max, SquT (Fig 2.15A), and PMax, while PetT and Pal display a weakly significant genotype effect. The postnatal regression shows that genotype has a significant effect on Max, SquT, Pal, and more weakly on Man (Fig 2.16D), Fro (Fig 2.16B), PetT, and SquO during the first postnatal days. The range of higher density bone over which the genotype coefficient curve is significant varies by bone and is typically reduced when the genotype*age interaction term is included in a multiple regression. For bones that display a significant genotype effect, the relative density curves of *Fgfr2*$^{+/P253R}$ mice tend to cluster separately from the *Fgfr2*$^{+/+}$ mice for all ages at which the bone is ossified (Fig 2.17). This contrasts with bone volumes, which do not tend to differ in the same way between *Fgfr2*$^{+/P253R}$ and *Fgfr2*$^{+/+}$ across the ages (Fig 2.10).

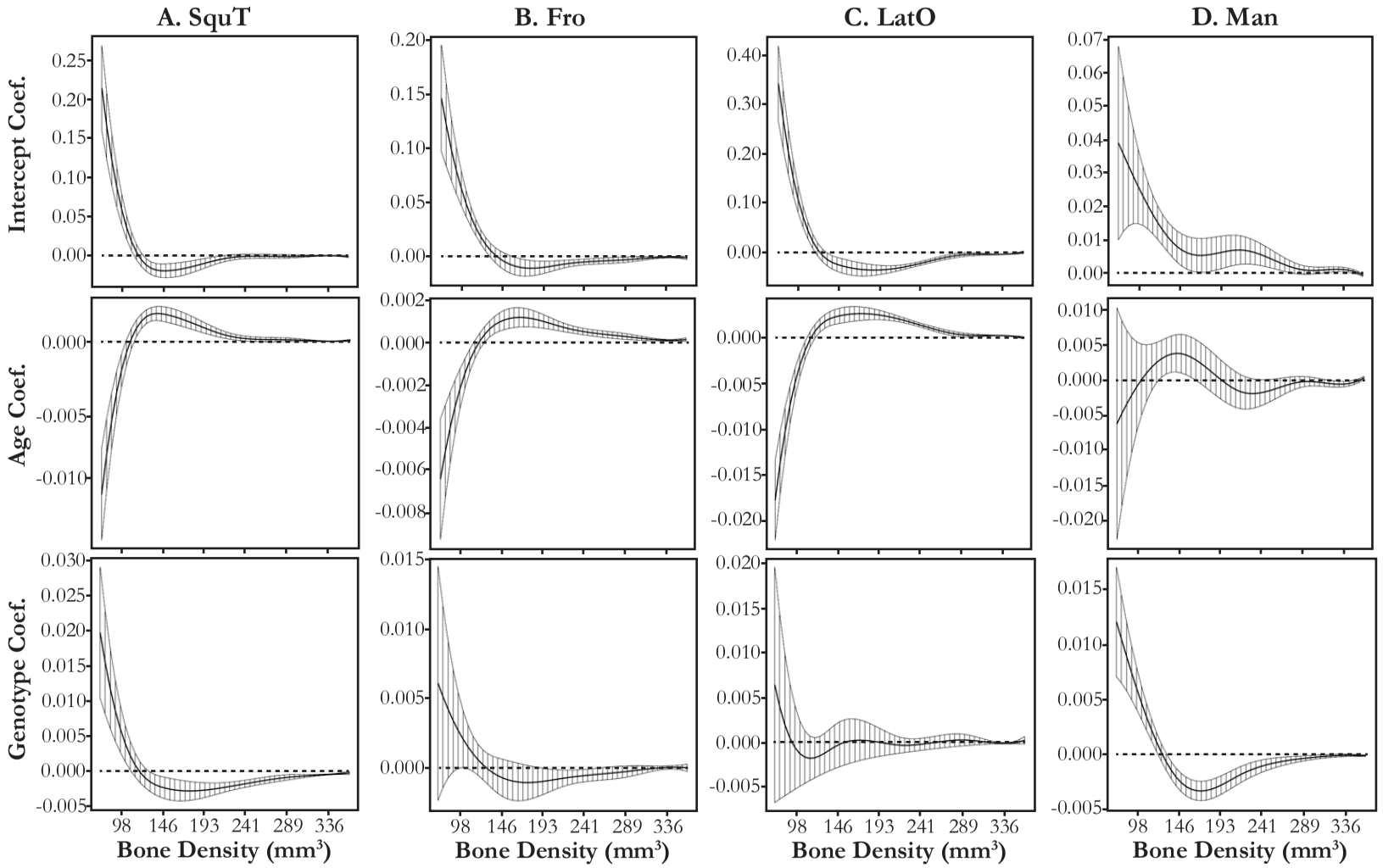

Fig 2.15 The functional intercept, age, and genotype coefficients and 95% confidence intervals from the prenatal multivariate regressions (without the interaction term) of standardized bone density curves for four bones from E15.5 to P0. (A) SquT displays a significant genotype effect between E15.5 and P0, which is opposite from the effect of increased age. This suggests that the effect of the P253R mutation on the maturation of this bone is analogous to a reduction in age. (B) Fro and (C) LatO do not display a significant genotype effect prenatally, but they do display a significant age effect over a wide range of density values. (D) Man is among a few bones that displays a weakly significant age effect during the prenatal period. However, it displays a strong effect of the P253R mutation. Bone abbreviations defined in Fig 2.3.

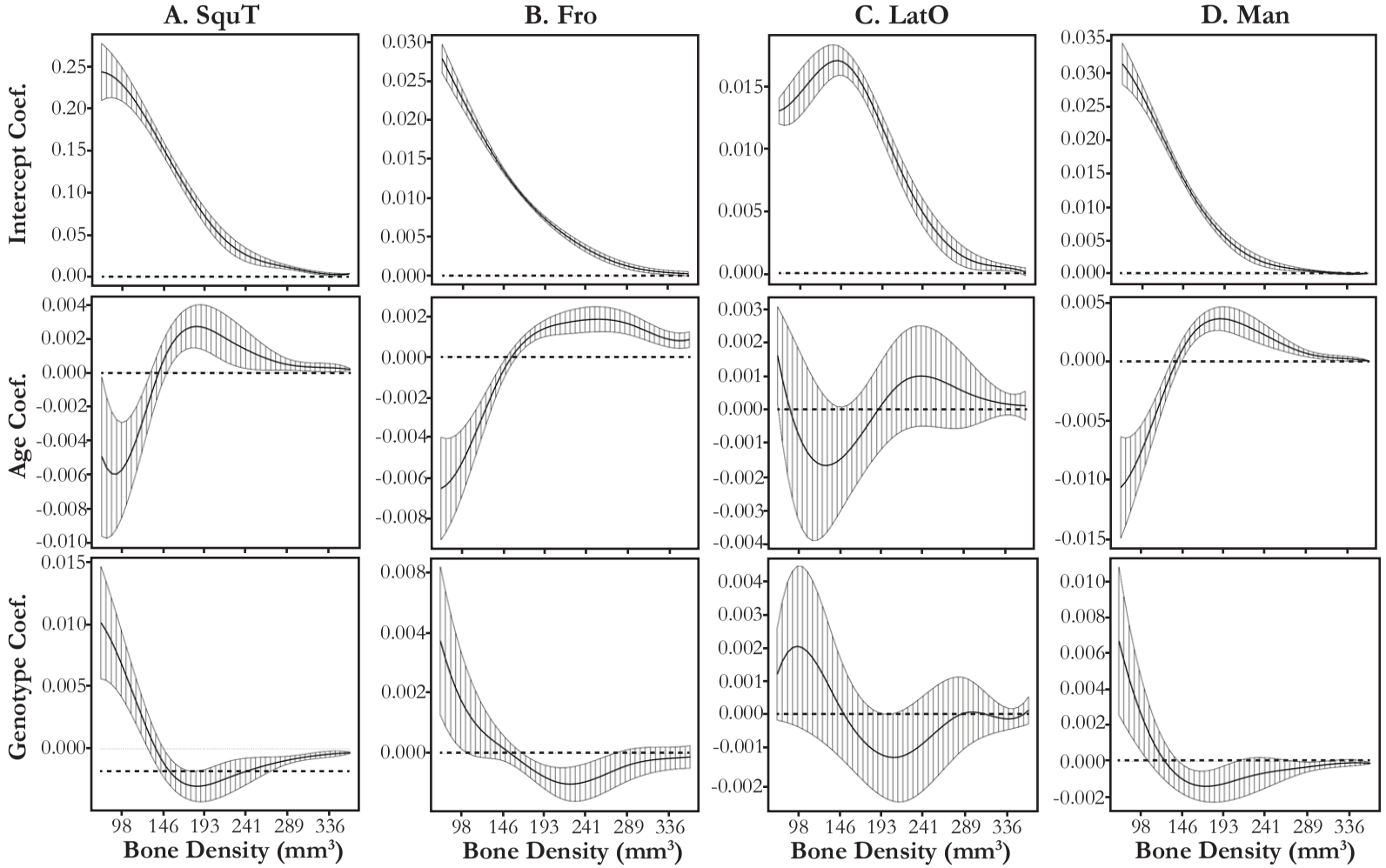

Fig 2.16 The functional intercept, age, and genotype coefficients and 95% confidence intervals from the postnatal multivariate regressions (without the interaction term) of standardized bone density curves for four bones from P0 to P2. (A) SquT and (B) Fro display significant genotype and age effects between P0 and P2, although the genotype coefficient is not significant over a wide range of bone density values. (C) LatO does not display a significant genotype or age effect postnatally. (D) Man displays a weakly significant effect of genotype and a strong effect of age during the postnatal period. For A, B, and D; the opposite nature of the age and genotype coefficient curves suggests that the effect of the P253R mutation on bone maturation is analogous to a reduction in age. Bone abbreviations defined in Fig 2.3.

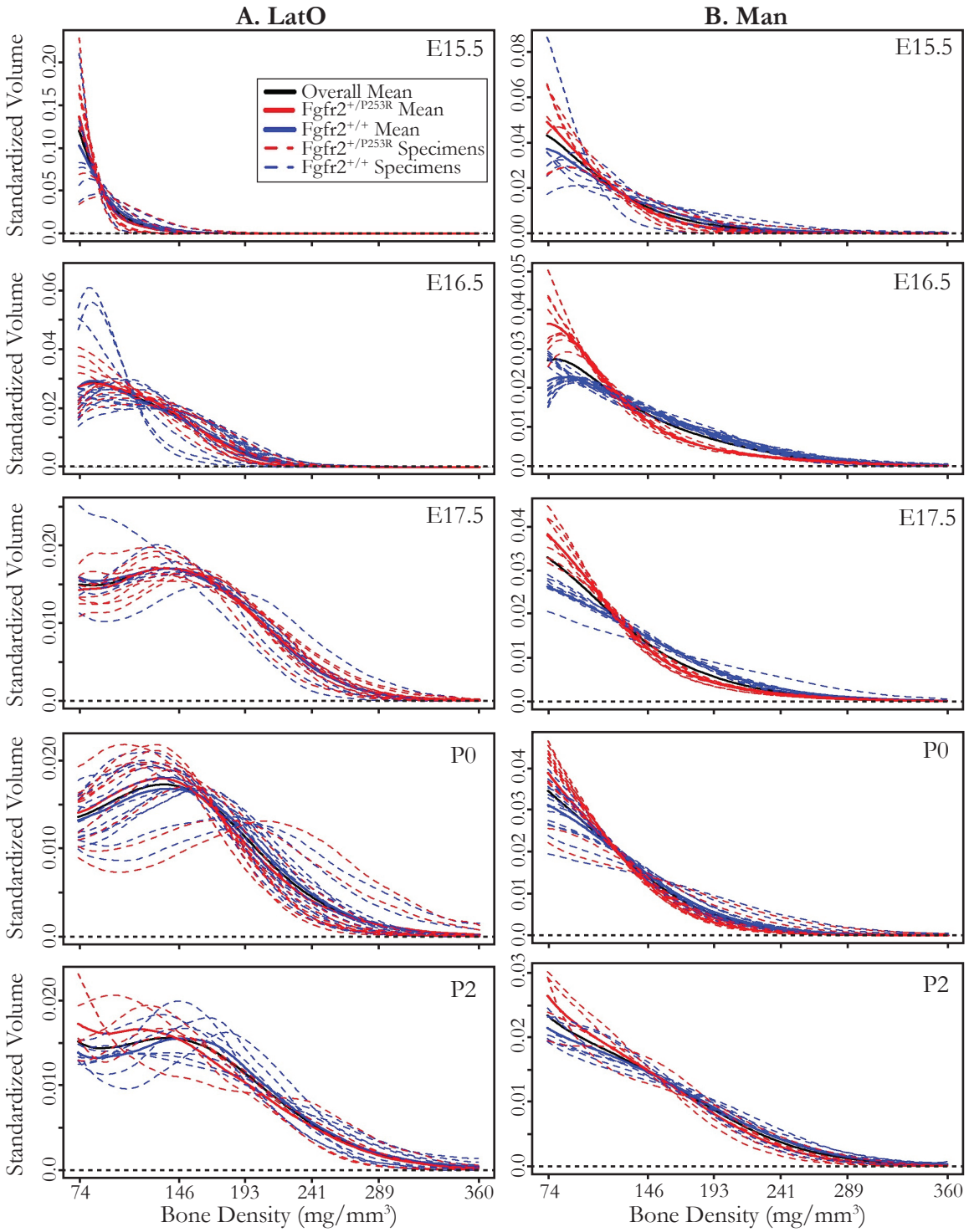

Fig 2.17 Standardized bone density curves for all specimens by genotype (*Fgfr2*$^{+/+}$: dotted blue; *Fgfr2*$^{+/P253R}$: dotted red) and age (E15.5 to P2), alongside overall mean (solid black), *Fgfr2*$^{+/+}$ mean (solid blue), and *Fgfr2*$^{+/P253R}$ mean (solid red). (A) LatO specimens do not cluster by genotype at any age. (B) Man specimens cluster by genotype at each age, but most obviously at E16.5, E17.5, and P0. This clustering is reflected in the regression results indicating significant effect of genotype on Man prenatally (Fig 2:15D) and weakly significant effect postnatally (Fig 2:16D). Bone abbreviations defined in Fig 2.3.

DISCUSSION

Method

HRCT provides direct three-dimensional representations of ossified volumes, allowing for quantification of their shape, size, relative density, and spatial association. However, measurements of bone volume and density based on phantom-calibrated HRCT images are likely to be lower than the results of other methods, including whole-mount staining and histology. This is due to lower spatial resolution and because mineralized tissue can only be identified in HRCT images after significant ossification instead of at initial calcium deposition or expression of another early bone marker that can be visualized with a staining technique. The use of nano-CT scanners can increase image resolution, while future studies comparing the density values produced from HRCT images and through other methods will improve bone density estimations. Synchrotron based CT systems also have the potential to produce more accurate bone density estimates (Nuzzo et al., 2000), but high cost and issues of access will limit their use for studies that include more than a few specimens. However, the results of the current study provide novel and valuable measurements of bone growth and maturation across the earliest periods of craniofacial ossification.

Because of relatively high levels of semi-automatic segmentation error for Pal, PSph, SphA, and SphB in P2 mutants, the results for these bones at P2 and in the postnatal regression should be accepted with caution, while the results for other P2 bones are unaffected.

Normal Craniofacial Bone Maturation and Growth

The normal pattern of bone growth and maturation illustrated in our results varies considerably within litters of mice. Two mice in the same litter may have very similar gestational ages, but noticeably different levels of craniofacial ossification. Improvements in identifying the relative developmental age of the embryonic craniofacial complex, as can be done for limb buds (Boehm et al., 2011), may

potentially control noise and increase the power of our phenotypic analyses. Differences in the genetic background of mice represent another source of variation for "normal" patterns of growth and maturation. While our mice are all on the same C57BL/6 background, they may display lower levels of bone density at a given age than mice of other backgrounds (Beamer et al., 1996; Beamer et al., 2001).

The mean standardized bone density histograms of *Fgfr2*$^{+/+}$ mice represent the relative density of bones at a given age. The changes in mean histograms from age to age provide a glimpse at the nature and speed of relative bone density change, a proxy for the process of bone maturation. Subjective investigation of these histograms revealed three patterns of bone maturation. Group 1 (Fig 2.12) displays an increase in relative bone density for each age interval from initial ossification until P2, as well as a peak in their curves that suggests relatively high levels of bone maturation. Early ossifying members of group 1 display strongly significant age coefficients from the prenatal multivariate regressions on bone density curves, although this strong age effect does not necessarily continue into the postnatal period. Each bone in this group develops through endochondral ossification and only one endochondral bone analyzed here falls in another group. Based on our results, ossification within a cartilage model may promote a quick increase in relative bone volume after initial ossification, although the pace of density increase may slow after birth.

Bones of the group 2 (Fig 2.13) sustain a weakly convex curve between E16.5 and P2, which represents moderate relative bone density without much increase, except perhaps between P0 and P2. These intramembranous bones of the face and vault maintain a stable level of bone maturation even as their volumes increase during the earliest ages of ossification (Fig 2.10). Bones of group 3 (Fig 2.14) retain a steep convex curve throughout the embryonic period, retaining low relative density until a relatively strong increase between P0 and P2. Most bones of the group ossify intramembranously

at the most anterior facial and most posterior-superior vault regions, suggesting that early increases in relative density are not required for bones at the periphery of the developing skull. Endochondral PetT from the cranial base is an exception. Additionally, not all bones fall cleanly within their respective category. PMax is assigned to group 3, but its pattern of maturation is fairly similar to group two. SphA is assigned to group 2, but matures a bit more consistently across the ages than other members of group 2.

Some bones from groups 2 and 3 display nonsignificant or weakly significant age regression coefficients during the prenatal period. This includes Man and Max, which display some of the smallest changes in density histogram curves between E15.5 and P0 (Fig 2.13). I expect that several more group 2 and 3 bones would display insignificant prenatal age effects if E15.5 was not included in our regression. However, even Man (Fig 2.16) and Max display significant age effects from postnatal regressions. Many group 2 and 3 bones display a noticeable change in mean relative density curves between P0 and P2 (Figs 2.13, 2.14), suggesting a postnatal increase in maturation for these bones, even if they do not display a strong prenatal increase in bone maturation. Data from later postnatal days are necessary to determine whether the relative density of bones from all three groups becomes similar later in development, although results from P0 and P8 ages of an associated mouse model suggest that they do (Chapter 4).

Our results show that the relative density of most endochondral bones noticeably increases after initial embryonic ossification (group 1), while intramembranous bones maintain a moderate (group 2) or low (group 3) relative density before postnatal density increases. Fundamental differences in early ossification may produce these differences between endochondral and intramembranous maturation (Chapter 1). The cartilage models of endochondral bones roughly reflect the shapes of the bones that ossify from them (Eames and Schneider, 2008). On the other hand, the proliferation of

precursor cells from mesenchymal condensations, within which intramembranous ossification begins, is necessary before the presumptive bones resemble their ossified versions (Lana-Elola et al., 2007; Yoshida et al., 2008). Perhaps this early expansion of precursors leads to a lower concentration of differentiating osteoblasts per unit volume within intramembranous bones during the earliest stages of ossification. However, lower activity levels of similar numbers of osteoblasts or increased speed of bone resorption may also explain our results.

The PetT may represent an important exception to the idea that endochondral bones mature more quickly during initial ossification. The PetT exists primarily as a relatively small ossified annulus for much of the embryonic period until a huge increase in PetT volume between P0 and P2 (Fig 2.9). In this way, it may be similar to SquO and PSph, which don't ossify until later in development, but mature very quickly once they start. If the annulus is disregarded from our measurement of the PetT, it is possible that the curves of PetT would fall in group 1, particularly if measurements after P2 were available.

Effect of the P253R Mutation

The significant differences in some bone volumes between *Fgfr2*$^{+/P253R}$ and *Fgfr2*$^{+/+}$ littermates represent relatively small changes compared to the day-to-day increases in volume associated with normal growth (Figs 2.8, 2.9). However, these differences in volume as well as those in relative density serve to better illuminate the bases of previously identified craniofacial dysmorphology in these mice and humans with Apert syndrome. The influence of the P253R mutation on bone volume appears to change across the prenatal period and then again postnatally, while the influence of genotype on relative density curves of a bone tends to be similar across ages.

Although not significant, most bones of *Fgfr2*$^{+/P253R}$ mice display lower mean volumes at E15.5, while several are significantly smaller at E16.5. Lower bone volume could be associated with reduced

expansion of bones outward or reduced bone thickness. Anecdotally, *Fgfr2*$^{+/P253R}$ mice appear to display reduced ossified extent for the bones with lower volumes at E15.5 and E16.5 (Figs 2.4, 2.6). If true, this distinction clashes with observations made at the coronal suture of *Fgfr2*$^{+/S252W}$ mice, which displayed increased osteoid deposition and more proximate bone fronts by E15.5 or E16.5 (Holmes et al., 2009). This difference might be explained by differences between the two Apert mouse models, acute regulatory shifts at the coronal suture, or the fact that HRCT images display relatively well ossified bone.

At some point around E16.5 and E17.5, cranial bone volumes of *Fgfr2*$^{+/P253R}$ mice begin to catch up with the *Fgfr2*$^{+/+}$ mice, leading to similar volumes for most bones at E17.5. By P0, the mean volumes of several bones are larger in *Fgfr2*$^{+/P253R}$ mice, including Max, which was smaller in *Fgfr2*$^{+/P253R}$ mice at E15.5 and E16.5. Although the effect of genotype on bone volume appears to differ across prenatal ages, a bone's relative maturation is affected the P253R mutation similarly across the period of embryonic ossification (Fig 2.17). The facial bones and PetT, which display significant volume differences at E16.5, also display significant or weakly significant genotype effects on relative density of *Fgfr2*$^{+/P253R}$ mice across the prenatal period. This suggests that the mutation retards bone maturation starting at initial ossification and that relative density remains reduced even as bone volumes approach or exceed normal levels.

A change in the influence of the P253R mutation on cell activity may explain the catch-up in bone volume noted for many bones by E17.5 and P0. Proliferation at the osteogenic fronts of the coronal sutures of *Fgfr2*$^{+/S252W}$ mice is reduced significantly at E16.5, although it did not differ at E13.5 or E15.5 (Holmes et al., 2009). Similarly, proliferation was reduced at E17.5 at the coronal sutures of *Fgfr2*$^{+/P253R}$ mice, but did not differ from unaffected littermates at E19 or P5 (Wang et al., 2010). Increased osteoblast differentiation has also been noted in *Fgfr2*$^{+/P253R}$ mice; between E16.5

and E17.5 (Yin et al., 2008) and between E17.5 and P5 (Wang et al., 2010). Decreased proliferation of preosteoblastic cells and increased differentiation associated with the P253R mutation may coincide with a change in normal gene expression patterns (Morriss-Kay and Wilkie, 2005) and/or the switch from an expanding population of mesenchymal progenitors to more typically described ossification outward from intramembranous bone ossification centers (Yoshida et al., 2008; Chapter 1). Assuming this regulatory shift occurs across the skull and not just at certain sutures; it may ultimately lead to increased ossification rates and be reflected in the quick volume increase that is noted for many *Fgfr2*$^{+/P253R}$ bones by E17.5 and P0. This catch-up volume increase may be associated with premature fusion of several facial sutures and midfacial hypoplasia. On the other hand, SquO, with initial ossification between E17.5 and P0 displays lower volume in *Fgfr2*$^{+/P253R}$ mice at P0. Perhaps its volume is influenced at P0 in the way that earlier ossifying bones were at E15.5 and E16.5.

Morphometric analysis indicates that *Fgfr2*$^{+/P253R}$ mice can be differentiated from *Fgfr2*$^{+/+}$ at P0 by brachiocephaly, midfacial hypoplasia, an anteriorly displaced cranial base, as well as synostosis of the coronal, maxillary-zygomatic, and premax-maxillary sutures (Wang et al., 2010; Martínez-Abadías et al., 2010; Hill et al., 2013). The bones for which volume is most strongly influenced at E15.5-E16.5 and for which relative bone density is influenced across the prenatal period include bones of the face that are associated with midfacial hypoplasia and facial suture fusion. This suggests that the developmental modifications responsible for facial dysmorphology occur during the earliest stages of ossification. Landmark based measures of bone scale suggest shorter linear scale of facial bones in *Fgfr2*$^{+/P253R}$ mice at P0 (Wang et al., 2010; Martínez-Abadías et al., 2010; Hill et al., 2013) as well as reduced growth of palate and face between E17.5 and P0 (Motch et al., 2012), while facial bones retain lower density and display similar (or higher) volumes at E17.5 or P0. The combination of these results suggests that the P253R mutation leads to changes in the locations or directions of bone growth,

rather than an overall reduction in the population of expanding bone cells. However, the reduction in relative bone density of some bones does suggest a reduction in bone cell numbers or activity per unit of ossified bone. Overall, this suggests thicker or squatter facial bones with reduced density at E17.5 and P0, which is, at least anecdotally, confirmed in our HRCT surface reconstructions (Figs 2.4-2.7).

A second shift in the influence of the P253R mutation on bone volume growth occurs postnatally. Between P0 and P2, *Fgfr2*$^{+/P253R}$ bone volumes do not increase as much as *Fgfr2*$^{+/+}$ volumes, leaving several bones significantly smaller for *Fgfr2*$^{+/P253R}$ mice at P2. Several vault bones, which did not differ significantly between embryonic *Fgfr2*$^{+/P253R}$ and *Fgfr2*$^{+/+}$ mice, have smaller volumes and/or reduced relative density curves in *Fgfr2*$^{+/P253R}$ mice. Reduced volume and relative density of vault bones may be associated with thin and hypoplastic vault bones found in human infants with Apert syndrome (Cohen Jr and Maclean, 2000). Many bones that had lower relative bone density prenatally retain significant or weakly significant density regression coefficients postnatally, although it is unclear whether this is based on continued differences in bone maturation between the genotypes or is a carry over from the prenatal period. The postnatal reduction in bone volume growth is similar to the reduction noted in the *Fgfr2*$^{+/Y394C}$ mouse model of Beare-Stevenson craniosynostosis syndrome between P0 and P8 (Percival et al., 2012). While it is plausible that this reduction is a direct regulatory effect of the P253R mutation, it may also be based on differences in feeding behavior between the genotypes. Postnatal specimens of related *Fgfr2*$^{+/S252W}$ and *Fgfr2*$^{+/Y394C}$ mouse models appeared to have less milk in their bellies than their *Fgfr2*$^{+/+}$ littermates (Personal Communication with Xueyan Zhou on 11/28/12 by email).

The smaller volumes of many *Fgfr2*$^{+/P253R}$ mouse bones at P2 appear to match the great reduction in skull size noted between P0 and P2 by previous morphometric analyses (Hill et al., 2013) including reduced growth of the palate and rostral cranial base, as well as increased relative height and

width of the neurocranium. The volumes of several neurocranial bones are reduced in *Fgfr2*$^{+/P253R}$ mice, suggesting that any neurocranial linear size increase is based on relatively wider fontanelles and sutures rather than increased ossification of the neurocranial elements. Such increased width might be associated with wide midline calvarial defects, such as that noted in some human infants with Apert syndrome (Cohen Jr and Kreiborg, 1996). High segmentation error of the palatal region in our P2 *Fgfr2*$^{+/P253R}$ sample means that we cannot comment on the mutation's effect on bone volume in this region.

The reduced *Fgfr2*$^{+/P253R}$ bone volume noted postnatally would not be expected if increased osteoblast differentiation and bone expansion continued until P5 across the skull, as occurs at the frontal suture (Wang et al., 2010). Par, which makes up one half of the coronal suture border, displays significantly lower volume at P2. It's possible that the difference in these and previous results merely reflects differences in approach or that the coronal suture represents a very specific set of regulatory circumstances that are not replicated across the rest of the developing skull. Assuming that a decrease in preosteoblastic cell proliferation and increase in differentiation occur between E16.6 and E17.5 across the skull, it is possible that postnatal populations of presumptive osteoblasts will be smaller for bones of *Fgfr2*$^{+/P253R}$ mice. A small progenitor cell population may limit the speed of bone growth and density increase via reduced potential for osteoblast differentiation, unless proliferation of preostoblasts increases to refill the population. This purely hypothetical explanation for lower postnatal bone volumes for *Fgfr2*$^{+/P253R}$ mice highlights the need for direct studies of bone cell activity in regions other than the coronal sutures of *Fgfr2* mutant mice if we are to understand the global effects of these mutations on craniofacial development from the earliest embryonic periods onward. The study of bones whose growth and maturation are significantly affected by the P253R mutation should be targeted.

Summary

Measures of bone volume and our functional analysis of relative density curves provide an excellent way to model the expected pattern of bone growth and maturation for individual bones across the earliest stages of ossification. Our results suggest that endochondral and intramembranous bones have fundamentally different patterns of bone maturation during this period. Endochondral bones appear to mature in bone density immediately following initial ossification. Intramembranous bones appear to retain a moderate or low level of bone density until the postnatal period, even as they significantly increase in volume. Further work on bone volume and relative density during the postnatal period will be required to verify that intramembranous bones display further bone maturation postnatally, even as some endochondral bones begin to slow their maturation.

The *Fgfr2* P253R mutation initially reduces the volumes and relative density of many craniofacial bones during the earliest stages of ossification, including bones of the face that display some of the most serious dysmorphology associated with Apert syndrome. A shift in the influence of the mutation on volume occurs between E16.5 and E17.5, when a previously noted decrease in osteoblast proliferation and increase in differentiation at the coronal suture may occur across the skull. The volume of most facial bones reaches or exceeds normal levels by birth, while their relative density remains significantly reduced until the postnatal period, illustrating the continued influence of early changes in ossification on the craniofacial phenotype. Between P0 and P2, the volumes and relative density of vault bones decrease as the overall relative linear scale of the skull is reduced and morphological dysmorphology grows more severe. We suggest that reduced osteoblast differentiation may account for this, although other explanations are equally plausible. Our results complement previous morphometric studies of *Fgfr2*$^{+/P253R}$ mice by providing a more nuanced understanding of the growth and maturation of the craniofacial skeletal phenotype. We have suggested several

hypotheses about the cellular bases of differences in volume and density, but studies of the effects of this mutation on cellular activity in bones located distant to the cranial vault sutures will be required to definitively connect the effects of the P253R mutation at the cellular and morphological level with associated phenotypic changes of the skull.

CHAPTER 3:
INVESTIGATION OF VASCULATURE AND SOFT TISSUE LAYERS ASSOCIATED WITH EARLY FRONTAL BONE MINERALIZATION

INTRODUCTION

Fgfr2$^{+/P253R}$ mice display significant craniofacial dysmorphology including midfacial hypoplasia, premature fusion of some craniofacial sutures, abnormal cranial vault shape (Wang et al., 2010; Martínez-Abadías et al., 2010), as well as decreased bone volume and density of some bones during early ossification (Chapter 2). Because tissue interactions are critical for craniofacial development and *Fgfr2* is highly pleiotropic, pinpointing the developmental pathways modified to produce craniofacial dysmorphology is difficult. FGFR2 plays an important regulatory role for bone cell activity during initial skeletogenesis (Iseki et al., 1999; Eswarakumar et al., 2002; Ornitz and Marie, 2002) and some *Fgfr2* mutations are associated with craniosynostosis syndromes (Cohen Jr and Maclean, 2000). However, FGFR2 is expressed in endothelial cells and some downstream pathways it activates, including p38 MAPK, are associated with angiogenesis regulation (Javerzat et al., 2002). Inhibition of FGFR2 in rat glioma cells reduces the vascularity and associated growth of resulting tumors (Auguste et al., 2001), suggesting that FGFR2 signaling plays an important role in promoting angiogenesis in some contexts. Specifically, FGFR2 has been shown to regulate cell migration but not proliferation of brain capillary derived endothelial cells (Nakamura et al., 2001), although the generalizability of this observation has been questioned (Javerzat et al., 2002). Regardless, FGFR2 appears to play a role in regulating osteogenesis and angiogenesis, which are both critical for normal bone formation and development (Chapter 1). Therefore, we hypothesize that the microvasculature associated with the mineralizing

frontal bones of *Fgfr2*$^{+/P253R}$ mice, which are less developed than those of unaffected littermates (Wang et al., 2005), will be different in anatomical network structure, density, or diameter when compared to unaffected littermates.

In order to investigate whether differences in frontal bone associated microvasculature exist, we chose to use a combined Optical Coherence Tomography (OCT) / Photoacoustic Microscopy (PAM) system on *Fgfr2*$^{+/P253R}$ mice and *Fgfr2*$^{+/+}$ littermate controls. This multimodal system produces registered images of blood vessel networks via PAM and of surrounding superficial tissue layers via OCT. By imaging specimens between embryonic day 13.5 (E13.5) and 16.5 (E16.5), a period that straddles the beginning of frontal bone ossification, we hoped to produce images of the mesenchymal condensations of the developing frontal bone, its mineralized portions, and the associated microvasculature. The major goals of this study were to 1) identify tissue layers and vasculature imaged with OCT/PAM, 2) determine the signature of frontal mesenchyme and bone within OCT images by comparison with high resolution micro-computed tomography (HRCT) images, and 3) quantify the micro-vascular network structure and its association with the developing frontal bone. Although the combined OCT/PAM imaging system did not produce as good a basis for quantitative analysis of microvasculature and developing bone as we had hoped, this study provides the basis for future attempts to study this relationship and represents an important step forward in our understanding of the development of tissues surrounding the developing frontal bone at the initiation of ossification. In particular, this study provides details on the feasibility of OCT/PAM imaging of sacrificed mouse embryos, illustrates the level of late embryonic variation of major superficial vessels of the head, and provides an initial test for differences in vascularity between *Fgfr2*$^{+/P253R}$ mice and unaffected littermates.

METHODS

Mouse Breeding

Mouse heterozygotes with neo (+/P253Rneo) (Wang et al., 2010) were mated with EIIA promoter Cre transgenic mice (EIIA-Cre, The Jackson Laboratory) to remove the neo cassette and allow heterozygous expression of the *Fgfr2* P253R mutation in all tissues from the preimplantation stage onward. Resulting litters were composed of approximately half $Fgfr2^{+/P253R}$ heterozygote mutant mice and half $Fgfr2^{+/+}$ unaffected littermate controls. Based upon timed matings and evidence of pregnancy, litters were sacrificed at prenatal days E13.5, E14.5, E15.5, and E16.5. Some of these embryos were also used in a study of craniofacial bone growth and development (Chapter 2). After sacrifice, specimens were fixed in 4% paraformaldehyde and stored in 0.01 M Phosphate Buffered Saline with sodium azide as an antibacterial agent. Care and use of mice for this study were in compliance with relevant animal welfare guidelines approved by Pennsylvania State University Animal Care and Use Committees.

The embryonic period between E13.5 and E16.5 was chosen, because it straddles the start of frontal bone ossification. This represents a period of blood vessel invasion, via angiogenesis, of a previously avascular mesenchymal condensation, coinciding with initial frontal bone mineralization (Chapter 1). Any differences in vessel morphology associated with the effects of the P253R mutation on angiogenesis are likely to be most severe during this period of mass vascular invasion.

Image Acquisition

A hybrid optical coherence tomography and photoacoustic microscopy system (OCT/PAM) in Dr. Lihong Wang's lab in the Department of Biomedical Engineering at Washington University in St. Louis, was used to simultaneously produce registered 3D images of soft tissue layers and blood vessels near the developing left frontal bone of embryos of each age (Fig 3.1). During OCT/PAM

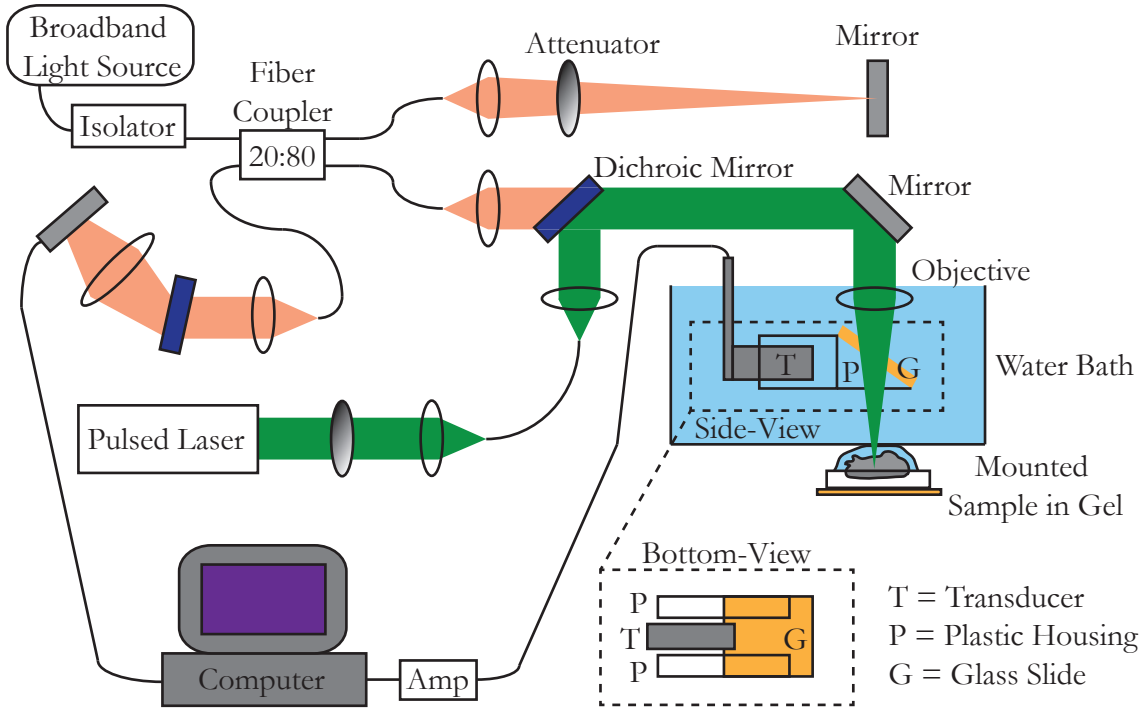

Fig 3.1 A schematic of the OCT/PAM system in Dr. Lihong Wang's lab in the Department of Biomedical Engineering at Washington University in St. Louis that was used for this study.

image acquisition, each specimen was placed on a carved agar bed so that the left frontal portion of the head was parallel with the imaging apparatus. The correctly oriented specimen was covered in ultrasound gel to prevent dehydration and to minimize optical and ultrasonic reflections during imaging (Fig 3.2A). Specimens were imaged immediately, cleaned gently with a paper towel and placed back in their PBS solution.

Materials that display strong characteristic optical absorption, including hemoglobin, produce a strong signal in PAM images, making it particularly well suited for studies of microvasculature (Zhang et al., 2006; Maslov et al., 2008). OCT images resolve soft tissue layers with different light scattering properties, producing images similar to those produced by ultrasound (Huang et al., 1991; Boppart et al., 1996; Larina et al., 2012), theoretically including distinct layers of frontal bone mesenchymal condensations and mineralizing frontal bone. OCT images provide important tissue layer context for the study of PAM imaged vasculature (Li et al., 2009). While there are other modalities that

could be used to produce images of microvasculature and soft tissue layers, OCT/PAM produces high resolution 3D images of relatively deep tissues without the need for contrast agents or the dissection of tissues. Perfusion of vascular contrast agents is difficult to achieve for mouse cranial microvasculature (Jamniczky and Hallgrímsson, 2011), particularly within mouse embryos. A major drawback of OCT/PAM for our study of sacrificed mouse embryos is that dead tissue displays a reduced signal for hemoglobin in PAM images. However, a few pilot images produced with relatively high laser fluence suggested that the OCT/PAM system would work for our purposes, although the signal of imaged vasculature is weaker in *ex vivo* specimens.

The OCT system utilized a fiber-coupled broadband light source (Superlum Broadlighter D890, Carrigtwohill, Ireland) with 890 nm center wavelength and 150 nm 3dB bandwidth. After an optical isolator (AC Photonics, Santa Clara, CA) to protect against back reflections, the light was spilt into 2 arms by a 20:80 fiber splitter (AC Photonics, Santa Clara, CA). The reference arm received 20% of the source light, which was further attenuated by a variable attenuator. The sample arm received 80% of the source light. The sample arm consisted of a dichroic mirror to combine the light sources for the OCT and PAM systems, a galvanometer scanner for fast one-directional scanning (Cambridge Technology 6220H, Lexington, MA), and an objective lens with NA 0.1. The entire sample arm apparatus was mounted on a linear translation stage (miCos GmbH, LS-65, Eschbach, Germany)

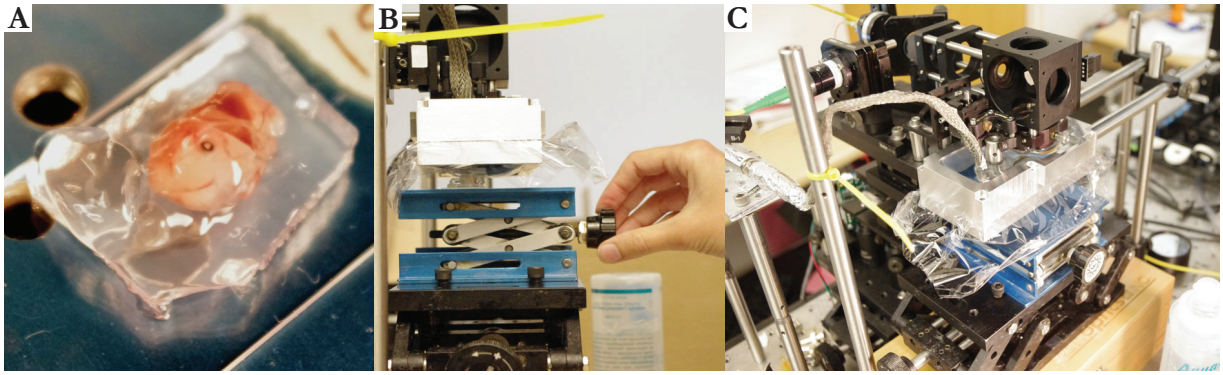

Fig 3.2 Photographs of (A) mounting a specimen on an agar bed with ultrasound gel covering it, (B) raising the mounted specimen to contact with the membrane under the water bath, and (C) the OCT/PAM imaging system.

which enabled a slow scan in the second *en face* direction. The OCT signal was detected using a custom spectrometer, consisting of a volumetric, transmissive grating (Wasatch Photonics, Logan, UT), a 2" imaging lens, and a CCD linescan camera (Atmel Aviiva M2, San Jose, CA).

The PAM system has been described previously (Rao et al., 2010). Briefly, the system utilized a pulse laser at 532 nm, 1.2 ns pulse width (Elforlight Ltd., Daventry, U.K.), which was combined with the OCT light source via a dichroic mirror in the sample arm. A piezoelectric transducer (General Electric, 25 MHz) was mounted on the sample arm apparatus inside a custom-machined plastic housing. A glass plate was glued to the housing to reflect ultrasound while transmitting light. The transducer face was shaped to exhibit a line focus. The line focus enabled fast scanning with the galvanometer scanner without compromising the confocal alignment of the laser and transducer focus. The transducer signal was amplified (Mini-Circuits ZFL-500LN, Brooklyn, NY) and digitized via a 12 bit data acquisition board (National Instruments NI-5124, Austin, TX). The objective lens associated with OCT imaging and transducer associated with PAM imaging were immersed in a water bath, enclosed on the bottom by a plastic membrane, which the ultrasound gel covered specimens contacted during imaging (Fig 3.2B-C).

The OCT/PAM system was operated at 5,000 A-Scans per second. The step size in the second *en face* direction was 5 μm. The datasets were all 800 A-Scans in the fast scanning direction and 800 B-Scans in the slow scanning direction. The *en face* field of view was 4 mm by 2.4 mm. The depth of each A-Scan was 1.54 mm in tissue. The number of points per A-scan was 700 for OCT and 200 for PAM. The system resolution was 3 μm lateral by 2.2 μm axial for OCT and 3 μm lateral by 7.7 μm axial for the PAM, with slice thicknesses of 5 μm. (Here the resolutions are given as minimal detectable spacing between two points, which is the convention for PAM. The spot diameters are approximately twice the values listed.)

Table 3.1 The number of specimens of both genotypes in this study, including resolutions of x, y, and z voxel dimensions.

	Sample Sizes		**Image Resolutions (μm)**								
			OCT			PAM			HRCT		
	Fgfr2$^{+/P253R}$	*Fgfr2*$^{+/+}$	x	y	z	x	y	z	x	y	z
E13.5	3	5	3.0	2.2	5.0	3.0	7.7	5.0			
E14.5	4	5	3.0	2.2	5.0	3.0	7.7	5.0	10.7	10.7	12.4
E15.5	5	4	3.0	2.2	5.0	3.0	7.7	5.0	10.7	10.7	12.3
E16.5	4	5	3.0	2.2	5.0	3.0	7.7	5.0			

The light power delivered to the sample for OCT was 440 μW continuous wave. The pulsed laser power for PAM was 500 μW, equivalently 100 nJ per pulse at 5 kHz. At focus, the fluence reached 300 mJ/cm^2. The safety limit for *in vivo* imaging recommended by the American National Standards Institute (ANSI) is 20 mJ/cm^2. We have shown that for imaging *in vivo* blood vessels, 8.5 mJ/cm^2 is sufficient (Rao et al., 2010). However, we have noted a significant drop in photoacoustic signal from blood vessels in fixed tissues, perhaps due to blood pooling in other areas of the body. To compensate, we used a higher fluence in these *ex vivo* experiments. We made an attempt to increase the OCT/PAM signals in our images by imaging living embryonic specimens *ex utero* as described previously (Syed et al., 2011). While a more complete vascular system was easier to distinguish within the *ex utero* images, the high density placental vascular network absorbed most of the light during imaging, precluding any deeper vessels appearing in the PAM images. Therefore, we did not further pursue this method.

After OCT/PAM imaging, high resolution micro-computed tomography (HRCT) images of mouse heads of a subset of the E14.5 and E15.5 specimens (Table 3.1) were acquired in air at the Center for Quantitative X-Ray Imaging at Pennsylvania State University (www.cqi.psu.edu) using an OMNI-X Universal HD600 industrial x-ray computed tomography system (Varian Medical Systems, Palo Alto CA). Solid hydroxyapatite phantoms (QRM GmbH, Möehrendorf, Germany) scanned with each set of skulls allowed us to linearly associate relative x-ray attenuation values with bone mineral density estimates (Fig 2.1). HRCT images were produced in order to verify tissue layer identification

in OCT images. However, processing and analysis of HRCT images was only carried out for the E15.5 specimens, because no bone was noted in the E14.5 images, although cleared specimens with alizarin red staining displays initial mineralization at this age. At E14.5, the mineralized portions of the frontal bone may be too low density to distinguish from other soft tissues in the HRCT images.

Tissue Identification

Individual craniofacial bones within E15.5 HRCT images were manually segmented using previously described methods (Chapter 2) in order to identify the location of the ossified left frontal bone within each specimen. Registration of HRCT images to OCT/PAM images was completed for E15.5 specimens using tools from Avizo 3D analysis software (Visualization Sciences Group, Burlington, MA, USA). Skin surfaces were produced from OCT and HRCT images of a specimen. Hair follicles, spread across the field of view of the OCT image, were landmarked on both surfaces to provide full and even coverage of the left frontal region of the head (Fig 3.3). The results of a three-dimensional thin plate spline warp of the HRCT landmarks to the OCT landmarks were used to

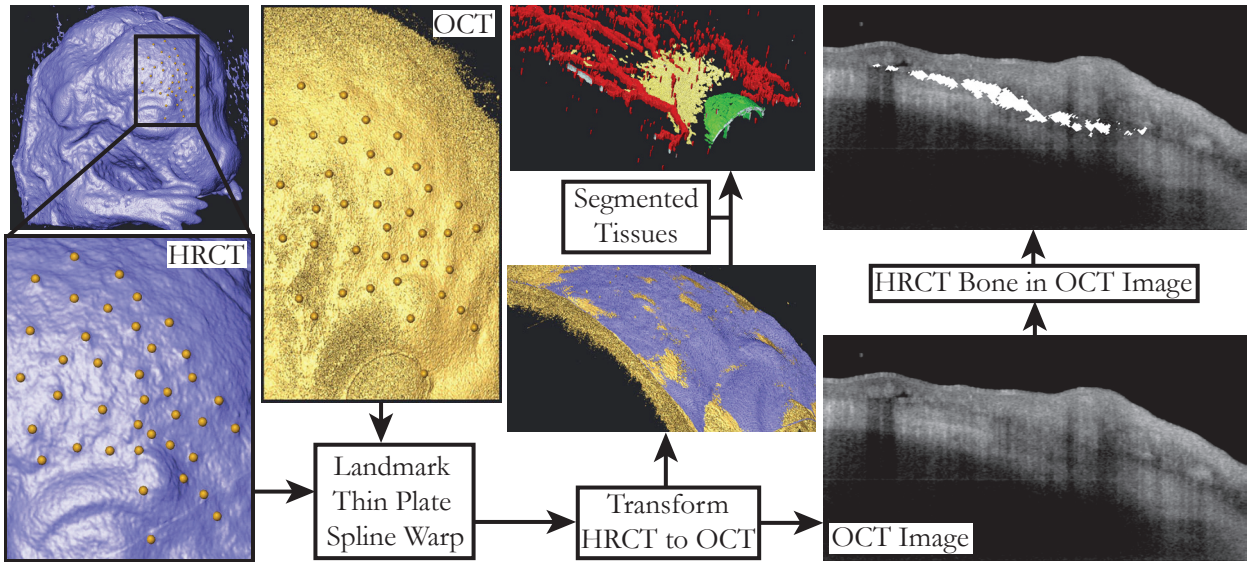

Fig 3.3 A diagram of the registration of HRCT segmented left frontal bones to OCT images of E15.5 specimens. Identical landmarks are taken on skin surfaces derived from HRCT and OCT image of a specimen. A landmark based thin plate spline warp is used to register HRCT image to OCT. The segmented left frontal bone from HRCT images can be displayed alongside tissues segmented from or visualized within the slices of OCT or PAM images.

register the HRCT image of a specimen to its OCT/PAM images.

Vasculature was segmented from the PAM images of all specimens starting with a 3D median filter to remove noise, followed by a hysteresis to threshold out the blood vessels, and finally an opening algorithm to remove some of the non-vascular speckle noise that was identified along with the blood vessels (Fig 3.4). The identities of major vascular groups in the segmented vascular networks were proposed based on consultation with published mouse atlases (Dorr et al., 2007) (Popesko et al., 1992). The total length of large vessels identified within segmented vasculature and a distribution of vessel diameters along their length were estimated from the segmented vasculature to quantify differences in gross vascularization between ages and genotypes (Fig 3.5). Volumes of less than three-thousand voxels within segmented vasculature were removed from this analysis in order to focus on positively identified large vessels. After 2D projection of the 3D segmented vessels to the *en face* plane, vessel centerlines were estimated from ridges derived from local distance maps, calculated as the shortest distance between each vascular pixel and the nearest vessel edge (Dougherty and Kunzelmann, 2007) within Fiji (Schindelin et al., 2012), an ImageJ (Schneider et al., 2012) distribution. The most serious artifacts of the ridge identifying process were removed from analysis with a minimum threshold value of 0.009 mm local distance, equivalent to an estimated vessel diameter of 0.018 mm. The remaining ridge voxels were binarized and skeletonized to thin the estimated centerlines to single pixel thickness. Total length of identified vessels within a specimen was estimated as the number of centerline pixels, while the distribution of local distances (multiplied by two) associated with centerline pixels represent the range of vessel diameters. Total vessel length, vessel diameter histograms, as well as diameter histograms standardized by total vessel length, were compared between genotypes at each age in order to test whether the identified vasculature in the *Fgfr2*$^{+/P253R}$ mice and their unaffected littermates differed. Two-sample Wilcoxon (Mann-Whitney) tests in R (R Developmental Core Team, 2008),

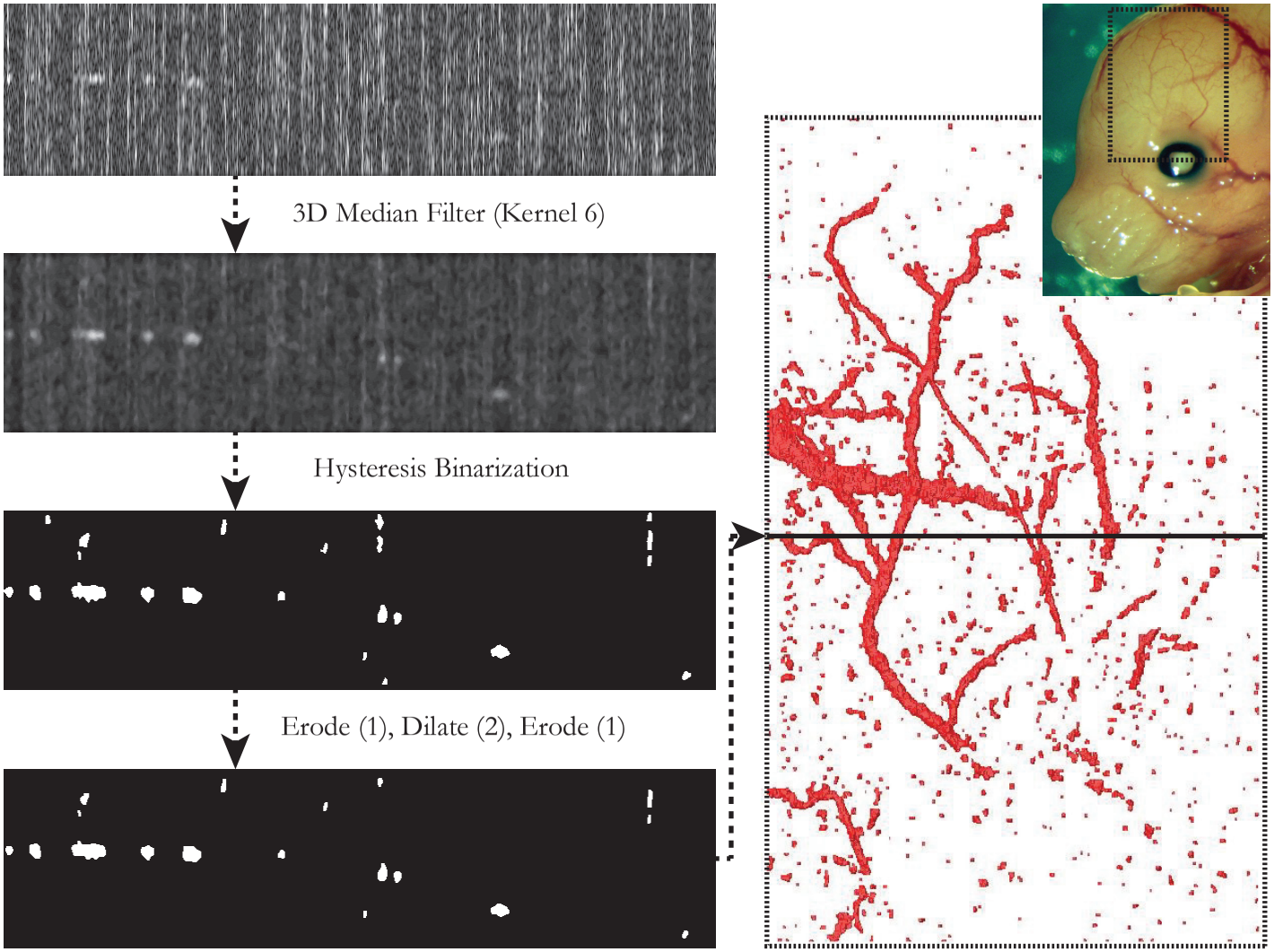

Fig 3.4 A diagram of blood vessel segmentation from PAM images. A median filter is run on the PAM image, followed by hysteresis binarization, and a conservative opening algorithm. The location of the example slice (solid line) is noted on an en face view of a surface representation of the segmented vasculature of an E15.5 specimen. Note that the PAM image is mirrored in relation to a photograph of the exterior of the same specimen (approximate FOV is illustrated with a dotted box). The contrast of the PAM original image and PAM median filtered image have both been modified to allow for better visualization in print.

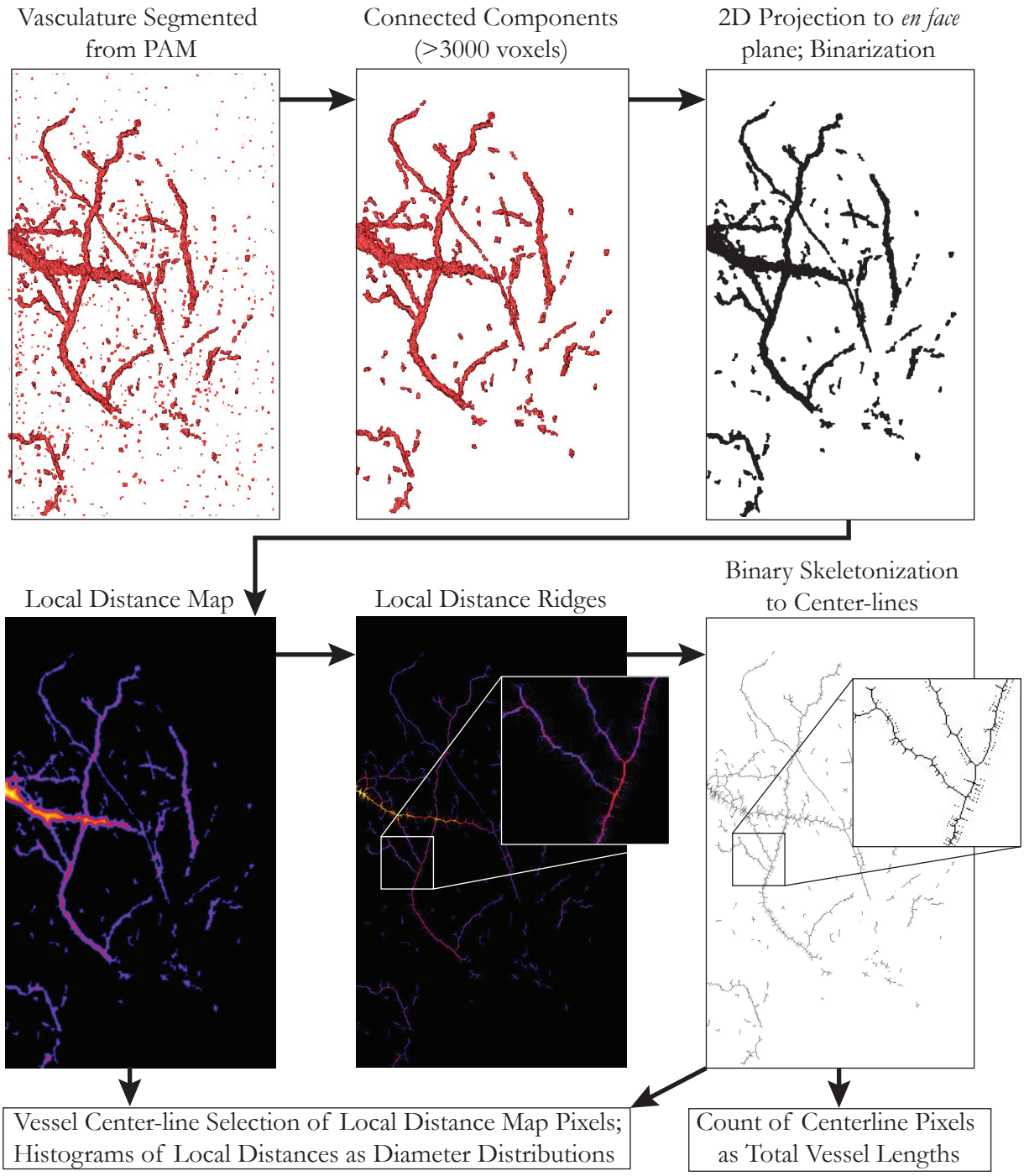

Fig 3.5 A diagram of the vessel length and diameter quantification method. Larger connected components of the PAM segmented vasculature are projected onto the 2D en face plane and binarized. Ridge lines of a local distance map are used to identify the centerlines pixels of the blood vessels. These centerline pixels are counted as a measure of total vessel length and used to select local distance measurements (multiplied by two) to produce a distribution of vessel diameters.

including Bonferroni correction for multiple testing, were used to compare the total vessel lengths between genotypes at each age.

Other soft tissue layers were identified within OCT images based on anatomical atlases, on histological sections of C57BL/6 mice, and according to the position of features within the registered images of all three types of images. The association of these tissue layers with the segmented vasculature was noted. Atlases of sectioned embryonic mice (Kaufman, 1999), embryonic mouse brains (Paxinos et al., 2007), and adult mouse anatomy (Popesko et al., 1992) provided a valuable first step. Second, the thickness of each superficial tissue was measured from sagittal histological sections of Masson's trichrome stained E13.5-E16.5 C57BL/6 mice, the background strain of the mice used in this study, and manually compared to the thickness of presumptively identified tissue layers measured from digital OCT image slices in Avizo. Third, the co-visualization of the vasculature identified from a specimen's PAM images, various tissues from OCT images, and bone identified from HRCT images helped to test the plausibility of OCT tissue layer identifications.

3D representations of the skin surface and the eye were produced from OCT images of all specimens and combined with surfaces of segmented blood vessels to allow for visualization of the depth of blood vessels and their 3D association with other tissue layers. Skin was segmented with a 3D median filter to remove noise, followed by edge detection, and a closing algorithm to produce a continuous skin surface. Eye was segmented from the results of skin edge detection, followed by a separate closing algorithm (Fig 3.6). The HRCT segmented bones within the OCT/PAM field of view were also included for E15.5 specimens. Variation in the pattern of segmented vasculature and the association of all identified tissue layers was noted for each age and comparisons were made between *Fgfr2*$^{+/P253R}$ mice and their unaffected littermates in order to identify gross effects of the P253R mutation on early soft tissue development in the region surrounding the developing frontal

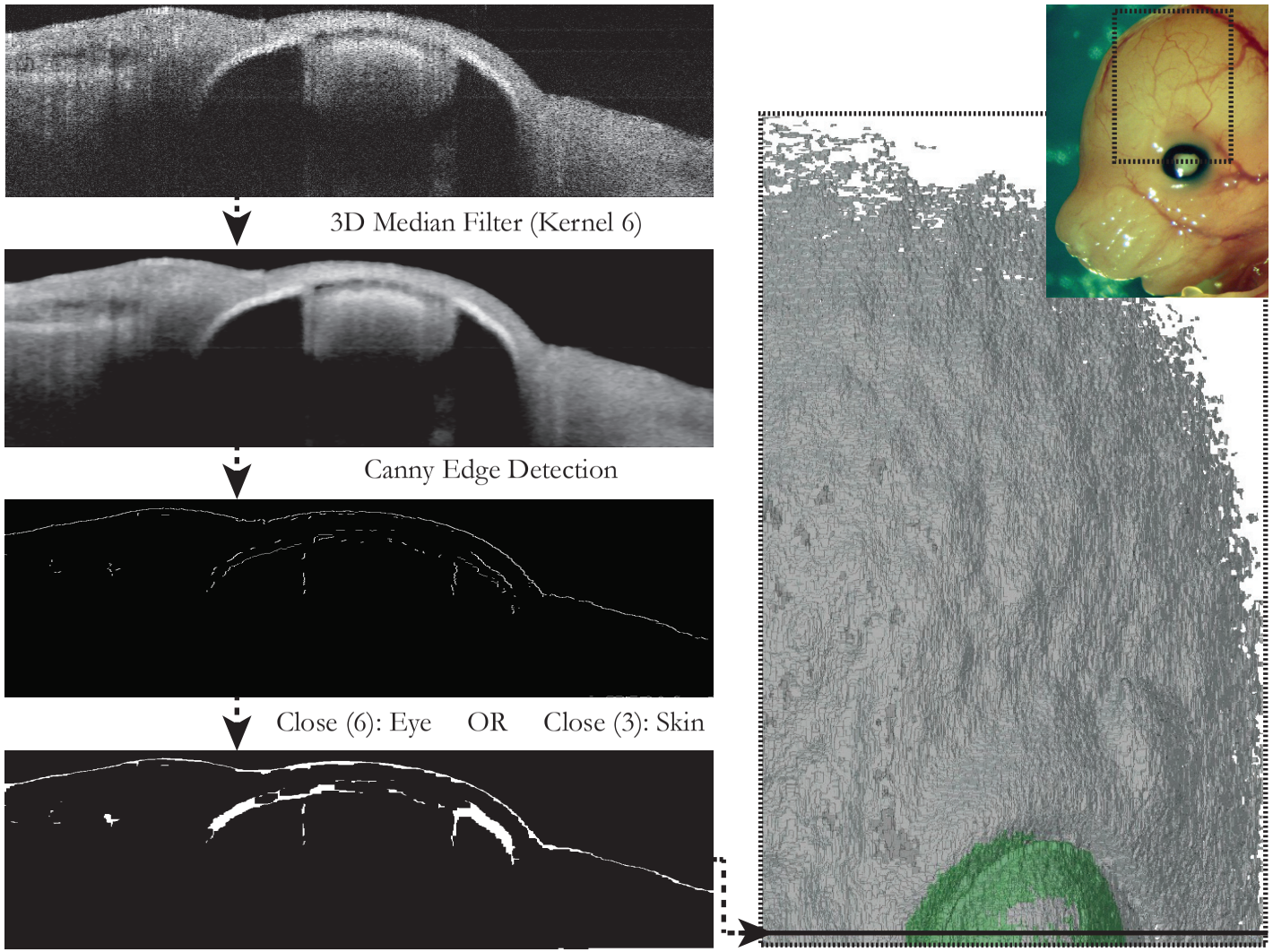

Fig 3.6 A diagram of eye and skin segmentation from OCT images. A median filter is run on the OCT image, followed by edge detection, and a closing algorithm. The location of the example slice (solid line) is noted on an en face view of a surface representation of the segmented skin and eye of an E15.5 specimen. Note that the OCT image is mirrored in relation to a photograph of the exterior of the same specimen (approximate FOV is illustrated with a dotted box). The top of all images have been cropped to allow more room for the portions of the image that contain tissue.

bone.

RESULTS

PAM Tissue Identification

The full vascular network is difficult to discern from our PAM images of a single specimen, because our method produced incomplete images of those networks. This is likely due to issues of blood pooling and blood cell breakdown that occur after sacrifice of the specimens. Therefore, the incomplete networks found in images of multiple specimens must be considered together in order to understand the typical vascular network within the frontal region of the mouse head (Fig 3.7) and the variation of this network (Figs 3.8-3.11). Three major vessel groups are identified from segmented vasculature of PAM images, based on tissue depth and their orientation within the field of view (FOV).

The first group of vessels occurs at the posterior superior portion of the OCT/PAM FOV as thick and stubby vessels traveling posterior-anteriorly at the depth of or deep to the meningeal layers. These are likely to be venous branches that feed into the transverse sinus (Dorr et al., 2007). The major member of this group, as noted in several E15.5 and E16.5 (Fig 3.10-3.11) specimens, might be the Caudal Rhinal Vein. Group 1 vessels do not appear in PAM images of E13.5 or E14.5 specimens. One or two of these vessels can be prominently found in images of many E15.5 specimens of both genotypes. However, obvious group 1 vessels are only found in *Fgfr2*$^{+/+}$ mice at E16.5.

The second group of vessels is superficial to group 1, group 3, and the developing frontal bone; traveling between a supero-posterior position of the FOV and an inferior point either anterior or posterior to the eye. If these superficial vessels originate posterior to the eye as they do in most E14.5 and E15.5 specimens (Figs 3.9-3.10), they are probably connected to the frontal artery, which is a branch of the external ophthalmic artery. While we cannot rule out the possibility that these vessels

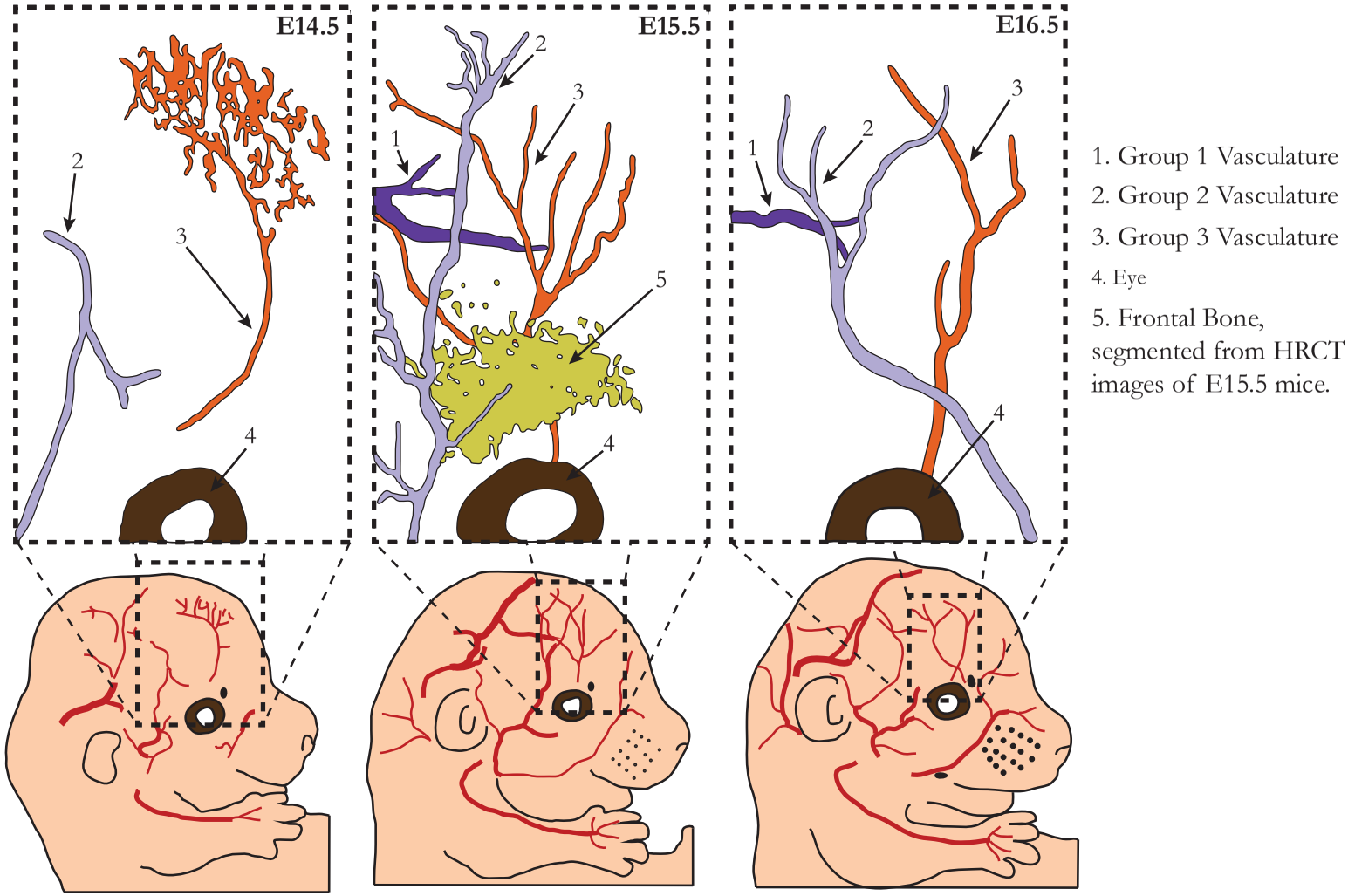

Fig 3.7 Schematic identification of the major groups of blood vessels found near the developing frontal bone in E14.5, E15.5, and E16.5 specimens (above). The eye, as segmented from OCT images, and the left frontal bone, as segmented from HRCT images of E15.5 specimens, serve to provide spatial context. The schematic drawings of embryonic heads (below) are based on images of embryos taken under a dissecting microscope, so include only relatively superficial blood vessels. The OCT/PAM field of view is equal at each age while the embryos grow larger with age. Although these drawings are based on images of the left side of the head, they are mirrored to reflect the mirrored nature of the associated OCT/PAM images.

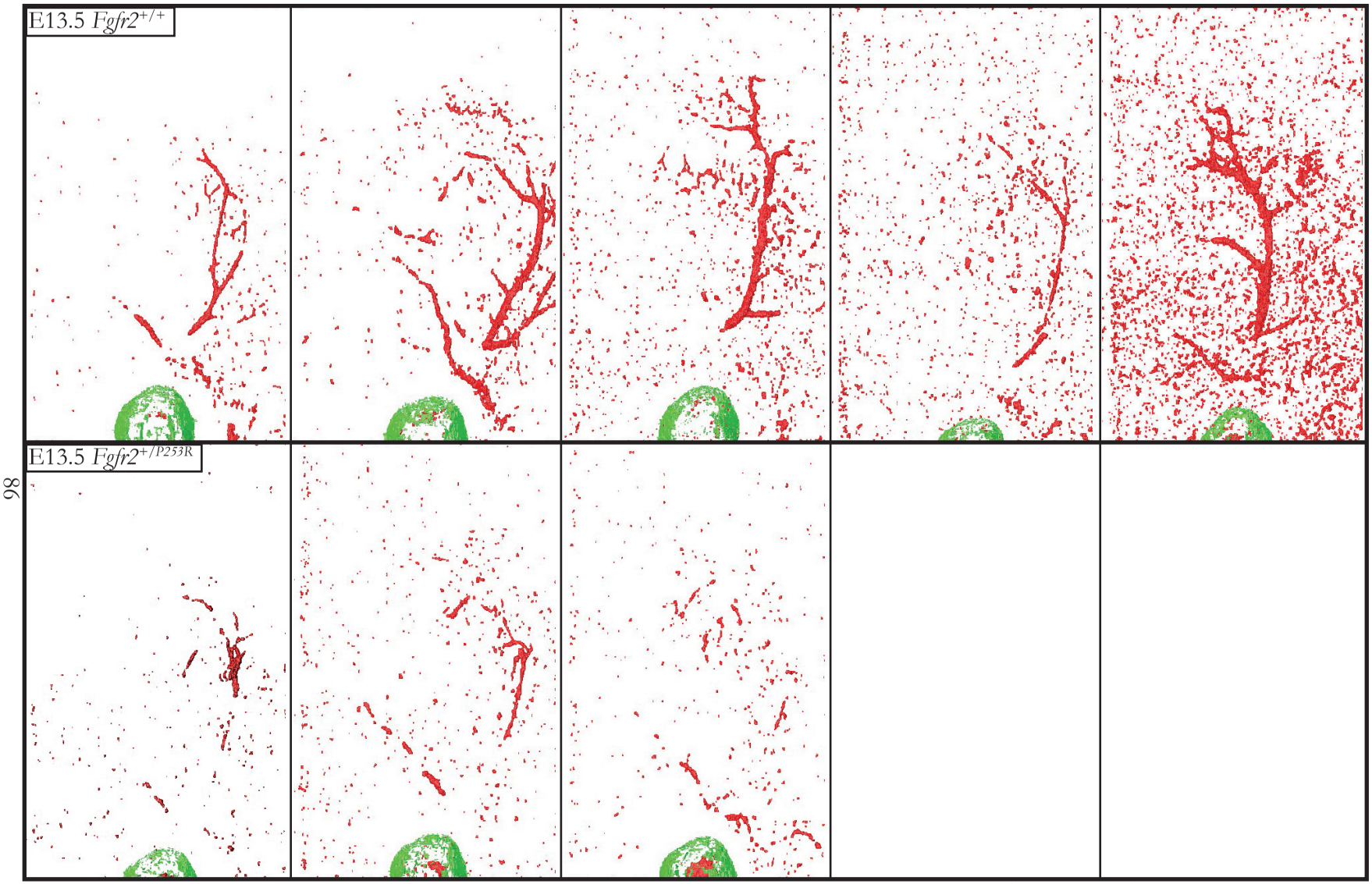

Fig 3.8 Comparison of variation in the vasculature (red) segmented from PAM images of E13.5 *Fgfr2*$^{+/+}$ and *Fgfr2*$^{+/P253R}$ mice. These images display the 3D vascular surfaces from the superficial perspective (en face) with apex of the head upwards and rostrum to the right. Eyes of each specimen (green), as segmented from associated OCT images, are displayed for reference.

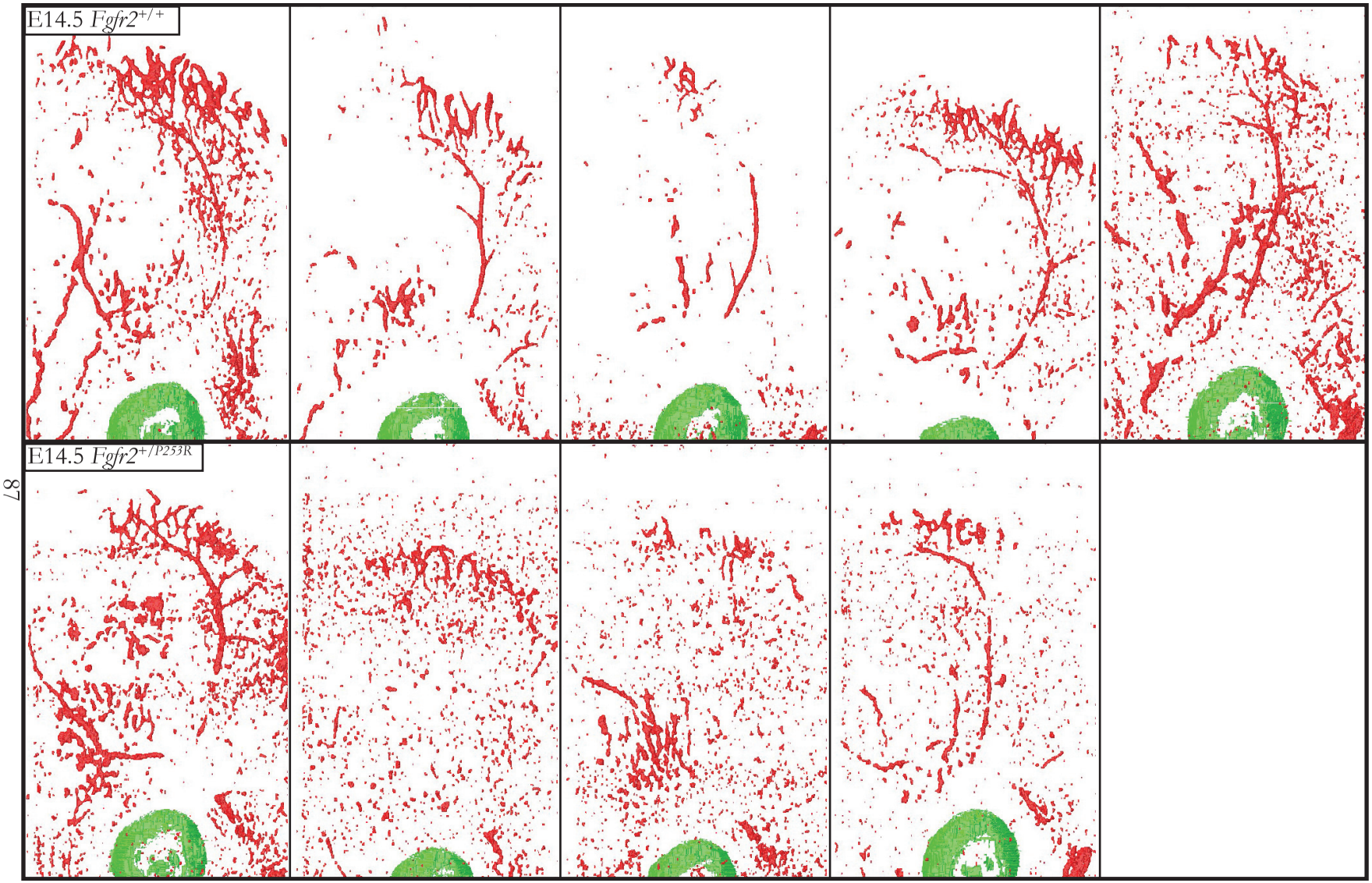

Fig 3.9 Comparison of variation in the vasculature (red) segmented from PAM images of E14.5 *Fgfr2*$^{+/+}$ and *Fgfr2*$^{+/P253R}$ mice. These images display the 3D vascular surfaces from the superficial perspective (en face) with apex of the head upwards and rostrum to the right. Eyes of each specimen (green), as segmented from associated OCT images, are displayed for reference.

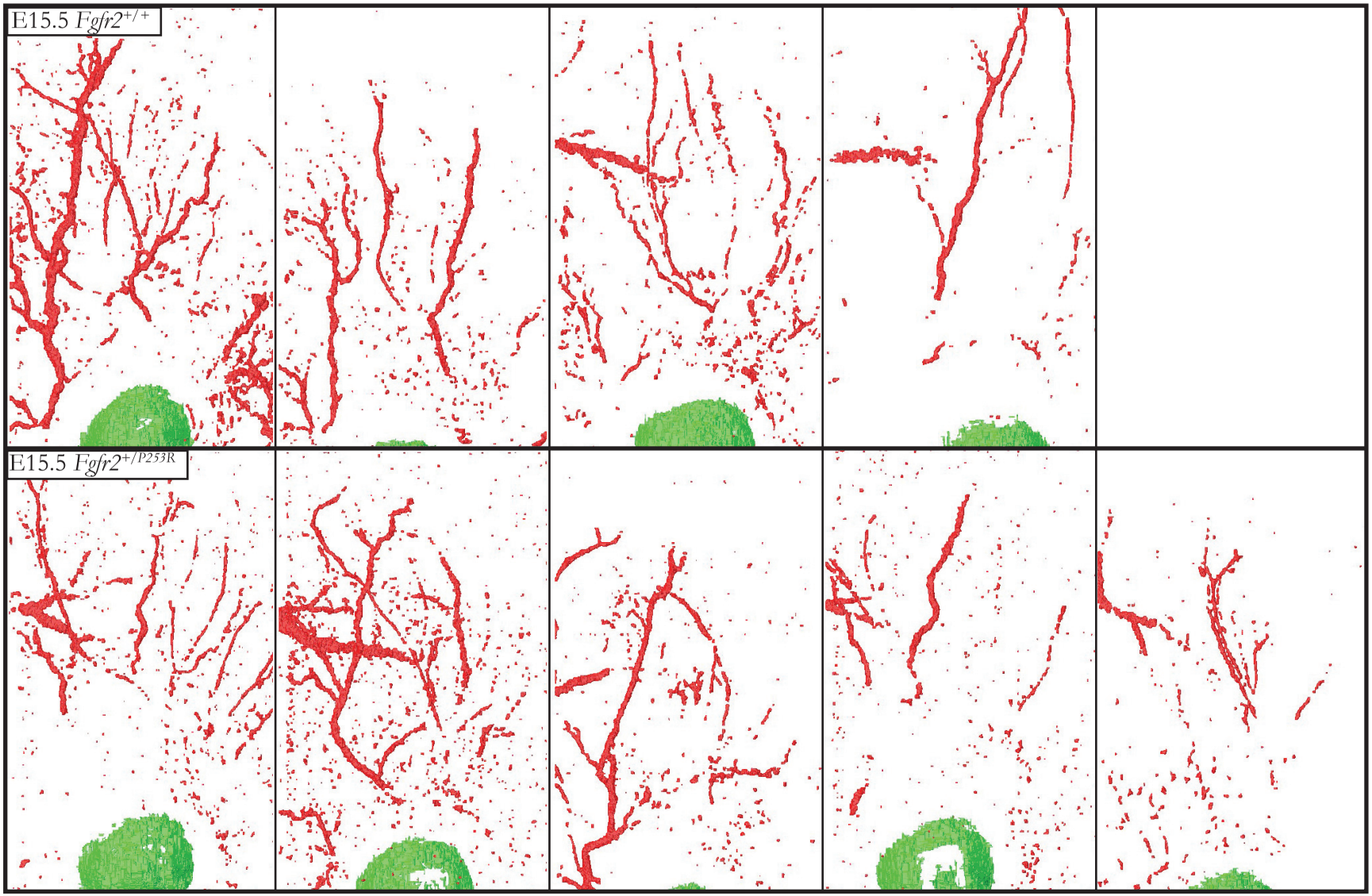

Fig 3.10 Comparison of variation in the vasculature (red) segmented from PAM images of E15.5 *Fgfr2*$^{+/+}$ and *Fgfr2*$^{+/P253R}$ mice. These images display the 3D vascular surfaces from the superficial perspective (en face) with apex of the head upwards and rostrum to the right. Eyes of each specimen (green), as segmented from associated OCT images, are displayed for reference.

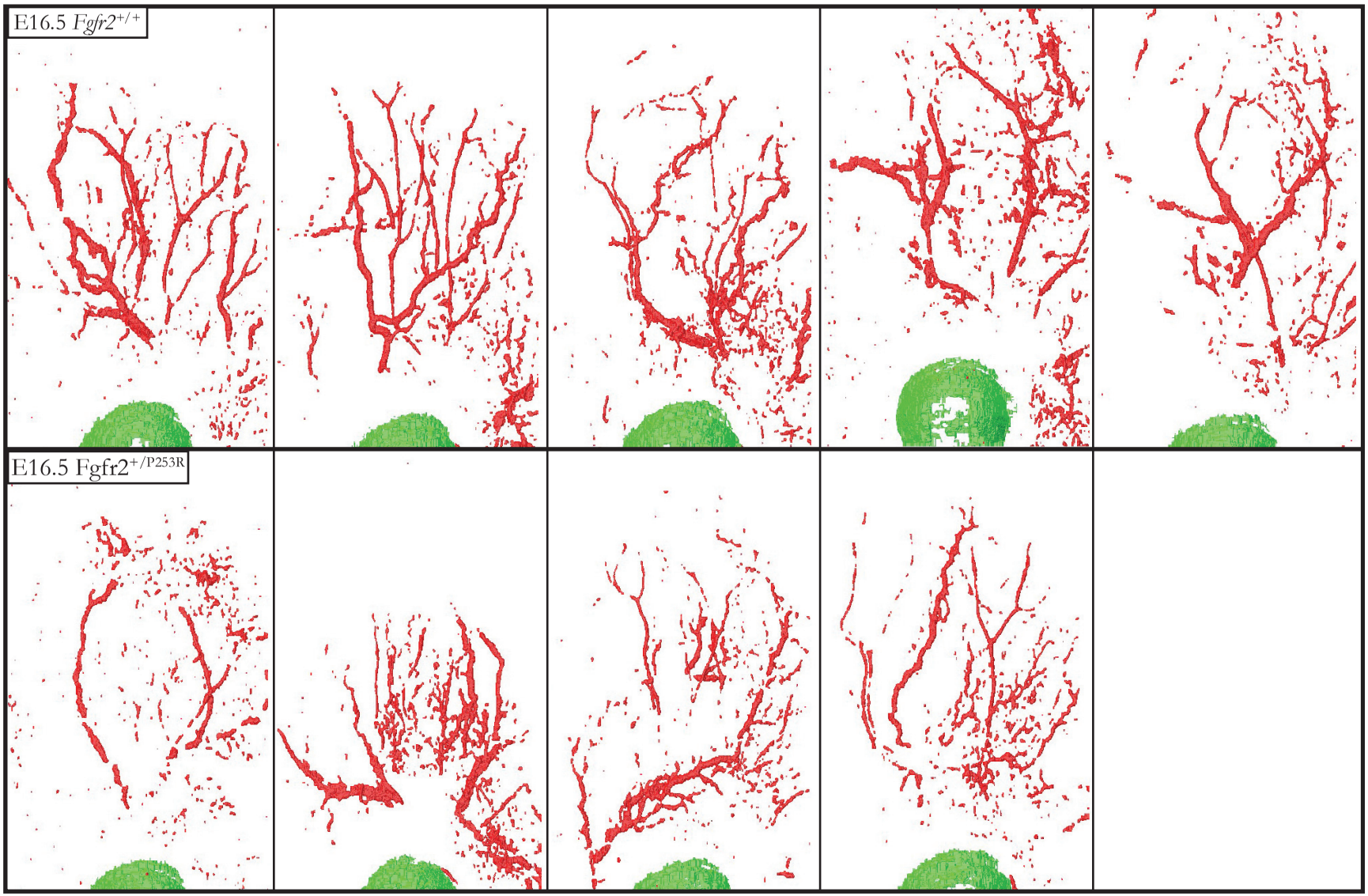

Fig 3.11 Comparison of variation in the vasculature (red) segmented from PAM images of E16.5 *Fgfr2*$^{+/+}$ and *Fgfr2*$^{+/P253R}$ mice. These images display the 3D vascular surfaces from the superficial perspective (en face) with apex of the head upwards and rostrum to the right. Eyes of each specimen (green), as segmented from associated OCT images, are displayed for reference.

might include veins which drain to the supraorbital vein and superficial temporal vein, we would then expect them to meet vessels in the eye socket, rather than travel posterior to it (Popesko et al., 1992). Group 2 vessels of several specimens, including many at E13.5 and E16.5 (Fig 3.11), appear to originate anterior to the eye, suggesting that they may be associated with the dorsal branch of the artery (or vein) of the ocular angle, which are extensions of the facial artery (or vein). Branches of the major examples of group 2 vessels tend to extend superiorly, mainly in the posterior direction. Its many branches are generally oriented in a superior-posterior direction. Examples of group 2 vessels are found in most specimens of both genotypes at all ages.

The third group primarily includes inferior-superior oriented vessels found in the central-anterior portion of the FOV, just deep to group 2 vessels and superficial to group 1. Unlike the vessels of group 2 that remain superficial across the FOV, inferior portions of group 3 vessels tend to run deep to the eye and the developing frontal bone. While group 3 may includes vessels with a number of origins, it is likely that the larger examples represent rostral, middle, or caudal branches of the medial cerebral artery, which runs superiorly along the contour of the brain from the Circle of Willis. Large group 3 vessels can be followed to the apex of the head in PAM images of E13.5 and E14.5 specimens (Figs 3.8-3.9), where they are associated with thick vascular networks, which curve posteriorly along the apex of the head as the middle cerebral artery does (Dorr et al., 2007). At E15.5 and E16.5 (Figs 3.10-3.11), group 3 vessels are not as striking as group 2 vessels and are more likely to be represented by a series of thinner vessels branching superiorly on the anterior half of the FOV.

PAM Vessel Measurements

While total vessel lengths are not significantly different between the two genotypes for any age after correction for multiple testing, relatively low p-values suggest that the PAM images of *Fgfr2*$^{+/P253R}$ mice display less vasculature than *Fgfr2*$^{+/+}$ mice at E13.5 and E16.5 (Table 3.2). The mean histogram

Table 3.2 Comparison of total vessel lengths between *Fgfr2*$^{+/+}$ and *Fgfr2*$^{+/P253R}$ mice, estimated as the total number of identified center-line pixels. The standard deviation of the total vessel lengths and the p-value from a two-sample Wilcox test of total vessel lengths between genotypes at each age are also listed. After Bonferroni correction for multiple testing, none of the p-values are significant, although the values at E13.5 and E16.5 are suggestive.

	Mean Total Vessel Length (Centerline Pixel Count)		Standard Deviation		2-sample Wilcox
Genotype	***Fgfr2*$^{+/P253R}$**	***Fgfr2*$^{+/+}$**	***Fgfr2*$^{+/P253R}$**	***Fgfr2*$^{+/+}$**	**Test p-value**
E13.5	1171	4451	2479	395	0.036
E14.5	7294	8715	3945	4824	0.905
E15.5	6008	7522	2713	4113	0.730
E16.5	6774	9499	2057	1345	0.063

values for *Fgfr2*$^{+/P253R}$ mice appear lower across the range of vessel diameters at each age, although the difference is strongest at E13.5. After standardizing these histograms by total vessel length, the means of both genotypes are almost identical and the variation between specimens is reduced (Fig 3.12). Of vessels with a diameter above our minimum threshold of 0.018 mm for this analysis, the most frequent vessel diameters in our PAM images occur around the value of 0.030 mm for both genotypes at each age. In addition to this peak, each histogram displays a long tail towards high diameter measurements.

OCT Tissue Identification

Our OCT images display major tissue layers surrounding the developing frontal bone, although the borders between layers are not always sharp. The superficial layers of the eye are easy to differentiate at the inferior edge of OCT images for each age (Figs 3.13A-B). Identifiable features of the eye include the eyelid, cornea, anterior chamber, lens, ventricular layer, and the vitreous cavity. The majority of the eye lies at a shallower depth in images of E13.5 specimens, so they also display the deep edges of the retina and the vitreous cavity. Our eye segmentation method (Fig 3.6), used for 3D tissue comparisons, identifies voxels parallel to and just deep to the cornea, including the ventricular layer of the eye and the anterior chamber. It also identifies the border of the lens and vitreous cavity, which runs perpendicular to the skin surface. This segmentation provides a comparable representation of

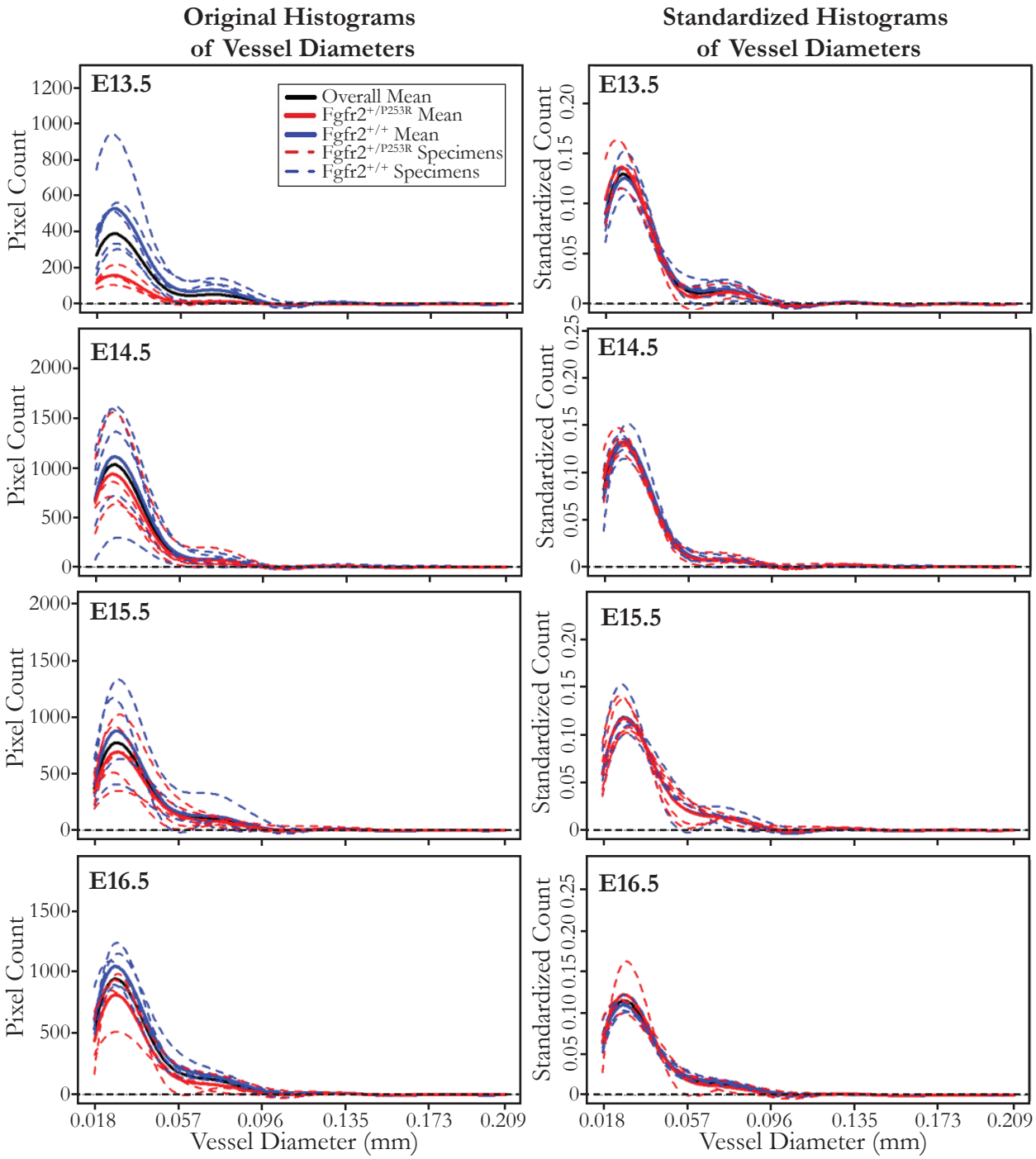

Fig 3.12 A comparison of large vessel diameter distributions of vessels segmented from PAM images for *Fgfr2*$^{+/P253R}$ mice (red) and *Fgfr2*$^{+/+}$ mice (blue) at each age. Distributions represented by cubic spline curves estimated from (left) original histograms and (right) histograms standardized by total vessel length (dashed lines). Genotype means and overall means (black) are also displayed for each age. The mean histogram curves of original histograms are always lower for *Fgfr2*$^{+/P253R}$ mice, particularly for E13.5 mice. Any differences in mean curves between genotypes disappear when the histograms are standardized.

eye position, curvature, and *en face* diameter at each age.

Superior to the eye, the deepest hyperintense (bright) layer found in E14.5-E16.5 mice is the first layer of the developing cortex (Fig 3.14). While the first cortical layer is not easily distinguishable at E13.5, other features of the brain can be identified, because more of the brain lies at a superficial depth in younger specimens. Identifiable brain features include the neopallial cortex, subventricular layer of cortex, ventricular layer of cortex, ganglionic eminence, and the ventricles (Fig 3.13C).

While the border between brain tissues and superficial tissues can be distinguished within OCT images from specimens of all ages, the number of visible superficial tissue layers increases with age, due to increased differentiation of previously indistinguishable layers and increased overall thickness of each individual layer. These soft tissue layers are easiest to distinguish about halfway through the OCT image stack at each age. This position is superior to the eye, under which the other soft tissue layers occur at a depth that OCT imaging cannot resolve. The position is also inferior to the apex of the head where superficial tissue layers tend to be less developed in embryonic specimens. Some large blood vessels can also be noted in OCT images at the same positions they are found in PAM images. These large diameter vessels appear as hyperintense patches of tissue and tend to mask deeper tissues in their shadows (Fig 3.13C and 3.14B).

A hyperintense layer is noted at the base of the superficial layers in E13.5 specimens, which probably represents a combination of the developing first cortical layer and the meningeal layers. Superficial to this is a hypointense (dark) layer, which represents loose connective tissue, including mesenchymal cells. The epidermis is noted as a very thin relatively hyperintense layer at the most superficial position. By E14.5, the deepest hyperintense layer is likely to represent the first layer of the cortex and the thin pia mater (Fig 3.14A). Superficial to this lies a thin hypointense layer, which likely represents the arachnoid mater, then another hyperintense layer of dura mater. The

arachnoid mater layer may also include subarachnoid space produced by the minor tissue dehydration that occurs during tissue preservation. Moving superficially, the thick hypointense layer of connective tissue and mesenchymal cells remains, capped by a striking hyperintense layer of epidermis. Near the location of a tactile follicle superior to the eye, a marginally more hyperintense and thicker portion of the hypointense connective tissue layer in E13.5 and E14.5 images may represent the mesenchymal condensation from which the frontal bone arises. This identification is based on comparisons to histological sections of similarly aged C57BL/6 embryos.

By E15.5, a layer of mesenchymal tissue can be more easily distinguished from superficial loose connective tissue and deeper meningeal layers (Fig 3.14B). Moving superficially from the hyperintense first layer of the developing cortex and pia mater lies a very thin hypointense layer of arachnoid mater (and subarachnoid space), a hyperintense layer of dura mater, a thin hypointense border layer, and a hyperintense layer representing mesenchymal tissue, including the mesenchymal condensation of the frontal bone. Superficial to this is a thick hypointense layer of loose connective tissue, capped by a thin hyperintense layer of epidermis, which displays a vertical texture. Based on the registration of bone volumes from HRCT images to the OCT/PAM images, the darker portions of the mesenchymal layer are likely to be regions of initial ossification. This region is proximate to the tactile follicle that was noted with the provisionally identified mesencymal condensation of the frontal bone in E13.5 and E14.5 images. Unfortunately, mineralized bone does not appear to have a distinct visual signature within OCT images. Superficial tissue layers of E16.5 images (Fig 3.14C) are thicker and more easily identifiable versions of E15.5 layers.

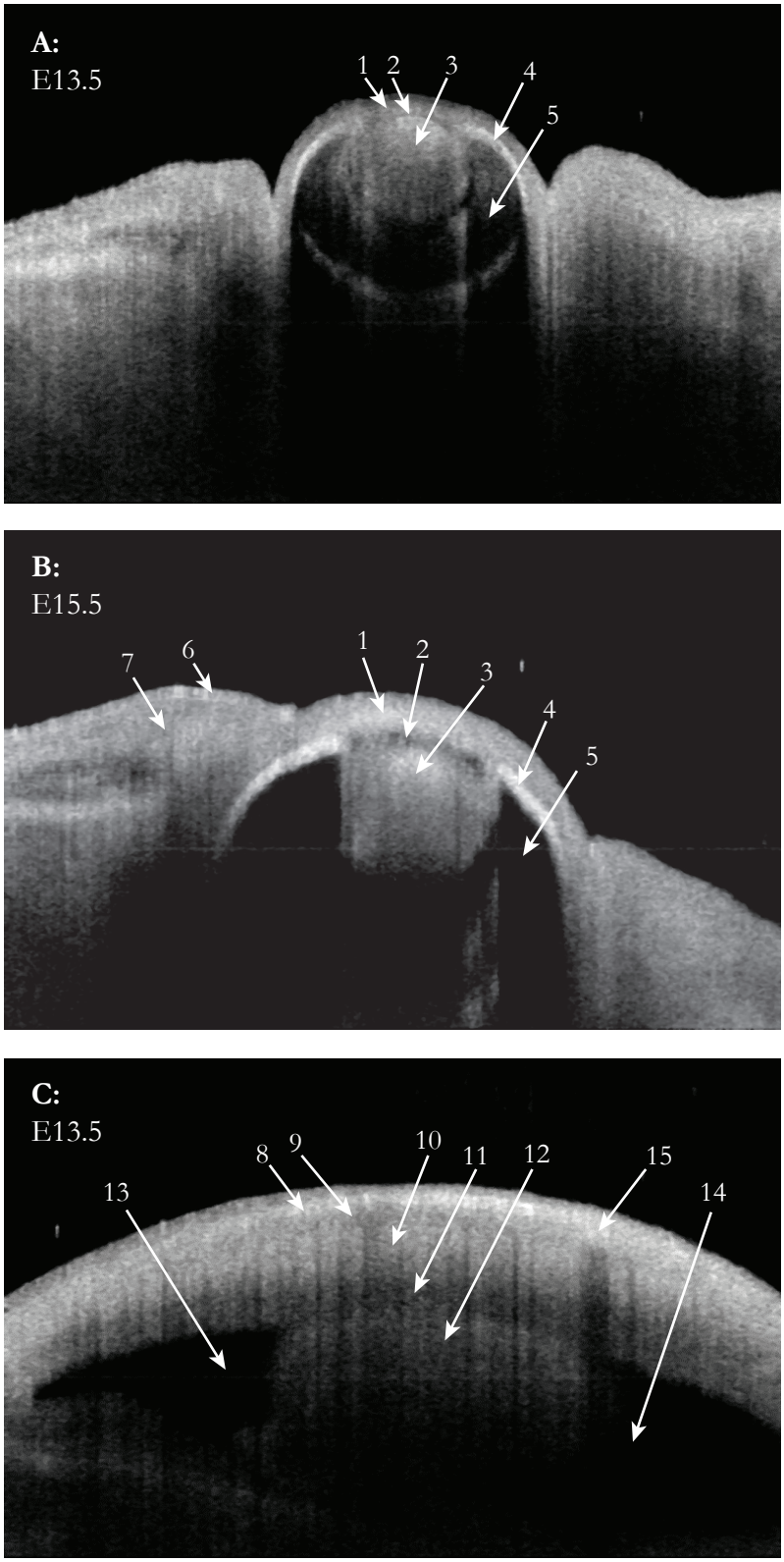

1. Cornea
2. Anterior Chamber
3. Lens
4. Ventricular Layer
5. Neuroepithelium and Vitreous Cavity
6. Epidermis
7. Loose Connective Tissue
8. Meninges and Outer Cortex
9. Neopallial Cortex
10. Subventricular Layer of the Cortex
11. Ventricular Layer of the Cortex
12. Ganglionic Eminence
13. Posterior Horn of Lateral Ventricle
14. Anterior Horn of Lateral Ventricle
15. Middle Cerebral Artery

Fig 3.13 Tissue layer identification on median filtered (kernel 3) OCT image slices of (A) the eye from an E13.5 specimen, (B) the eye from an E15.5 specimen, and (C) the brain of an E13.5 specimen. Tissue layer identifications are based on anatomical atlases (Kaufman, 1999; Paxinos et al., 2007; Popesko et al., 1992) and comparison to Masson's trichrome stained histological sections.

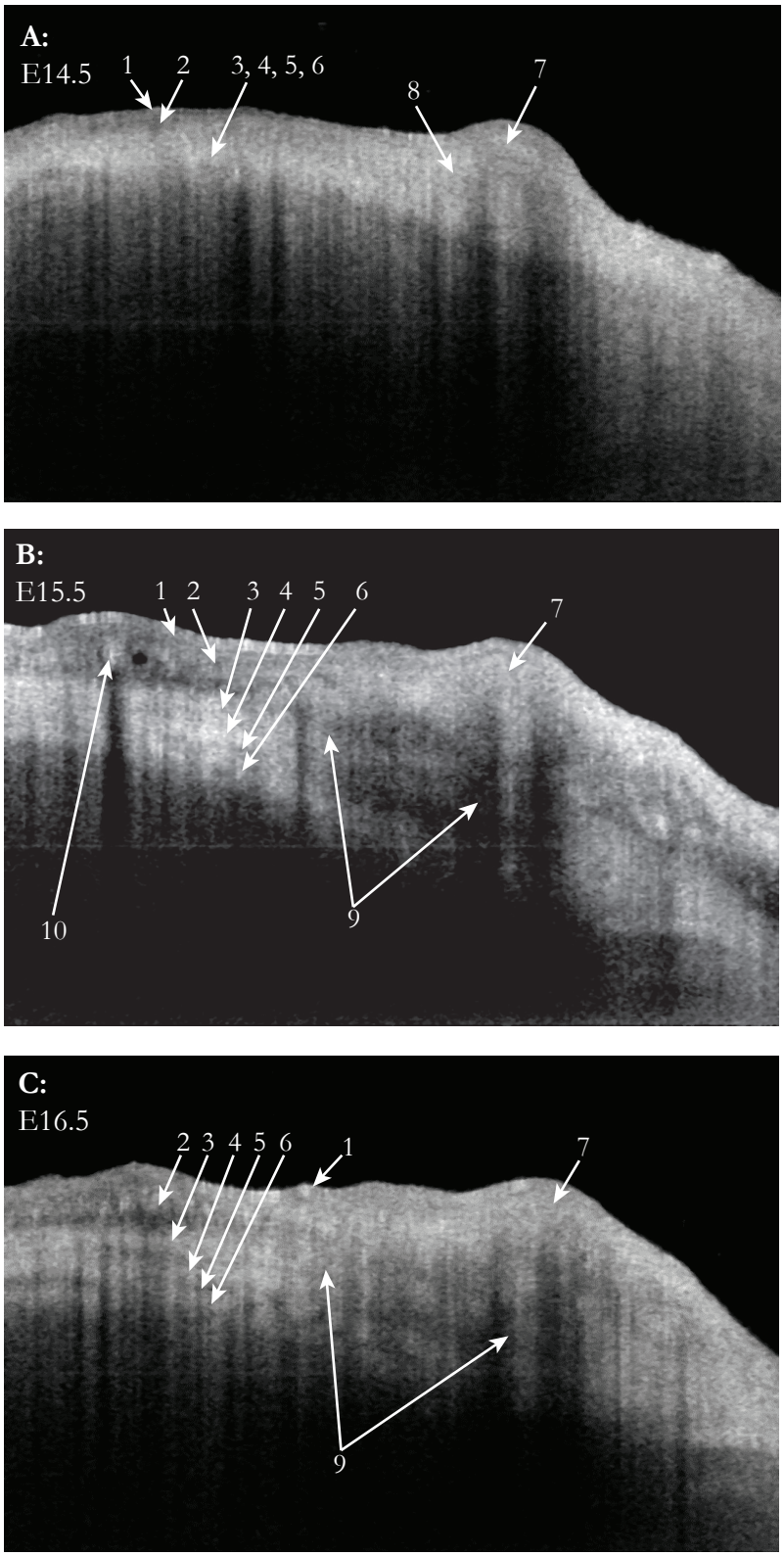

1. Epidermis
2. Loose Connective Tissue
3. Mesenchymal Condensation
4. Dura Mater
5. Arachnoid Mater and/or Subarachnoid Space
6. First Layer of the Developing Cortex
7. Developing Tactile or Sinus Follicle
8. Mesenchymal Condensation of Frontal Bone?
9. Region of Developing Frontal Bone?
10. Large Blood Vessel

Fig 3.14 Tissue layer identification on median filtered (kernel 3) OCT image slices from near the developing tactile follicle found anterior-superior to the eye from (A) E14.5, (B) E15.5, and (C) E16.5 specimens. Tissue layer identifications are based on anatomical atlases (Kaufman, 1999; Paxinos et al., 2007; Popesko et al., 1992) and comparison to histological sections of trichrome stained mice.

DISCUSSION

PAM Tissues

While the our PAM images do not provide a way to determine whether an individual vessel is arterial or venous, their depth and direction allow for the general identification of large blood vessels to be made. Although the broad microvascular networks that we hoped to study are not resolved in our PAM images, they provide important information about the locations, variation, and development of larger vessels in the region of the developing frontal bone during the period of initial osteogenesis. Although resolved vessels tend to be significantly larger than capillaries, they are smaller and more variable than commonly named vessels of the head. We identified groups of blood vessels by their probable association with larger named vessels in order to allow for comparison across specimens and ages.

Although the vasculature of the brain is well studied, few detailed studies of calvarial vasculature exist for humans or mice during the prenatal period. Human fetal calvarial bones have been shown to contain both venous and arterial vessels, which display anastomoses between fine arterial and larger venous elements (Langer, 1877; Rowbotham and Little, 1965; Brookes and Revell, 1998). The cranial meningeal arteries supply calvarial bones via nutrient arteries passing through the inner table of the bone, while pericranial arteries supply the bones through foramina close to their sutural edges. While the dural supply is commonly regarded as the primary source of blood to calvarial bones, they can survive when nourished only through existing vascular connections between the outer table of the bone and pericranial arteries (Brookes and Revell, 1998). This implies that vessels stemming from the meningeal arteries and vessels supplying tissues superficial to bone, including the external ophthalmic and facial arteries, both supply significant amount of blood to the developing frontal bone.

Unfortunately, we have been unable to positively identify any vessels that directly supply or

drain the developing frontal bone. Some members of the group 2 vessels may connect to vessels of the surrounding calvarial bones pericranially. Some members of group 2 and 3, particularly some of the smaller vessels, may be misidentified branches of meningeal vessels. The mouse equivalent of the middle meningeal vessel, the largest meningeal vessel in humans, is quite small in mice (Popesko et al., 1992), so it is likely not as important to calvarial bone supply as it is in humans. Although we were unable to overcome the limitations of the PAM/OCT for imaging dead tissues in order to identify microvasculature that is directly associated with the developing frontal bone, our PAM images provide an overview of the 3D association and development of larger blood vessels near it.

There is a large amount of variation in the branching patterns, orientation, and size of vasculature resolved within our PAM images. E13.5 and E14.5 vascular networks are more similar to each other than to E15.5 and E16.5 systems in that they do not contain group 1 vessels and their group 3 vessels are much more pronounced when compared to group 2 vessels. Group 3 vessels seem to be particularly reduced in their relative extent by E16.5 when group 2 vessels appear to encroach on regions of tissue that the group 3 vessels originally supplied. These changes suggest that there may be a significant shift in the gross vascular network of the region surrounding the developing frontal bone at the time when its ossification first occurs. However, we cannot test whether the shifts noted during this time are more significant than other shifts noted during embryonic development, because we only have images from the time period surrounding initial frontal bone ossification. Another significant point of variation is that group 2 vessels in many E13.5 and E16.5 specimens are oriented towards vessels anterior to the eye, while they are oriented towards vessels posterior to the eye in many E14.5 and E15.5 mice. However, it is important not to over interpret these differences in gross vascular morphology, because embryonic vasculature tends to be highly variable and we are working with small sample sizes. But, it would be interesting to see if the changes in gross vascular network morphology

noted between embryonic days in this study are also found by future studies of the cranial vascular system.

Total vascular length, measured as the number of centerline pixels from the segmented vasculature of each specimen, may be lower in *Fgfr2*$^{+/P253R}$ specimens than *Fgfr2*$^{+/+}$ mice, particularly at E13.5. Comparisons of vessel diameter histograms suggest that this difference occurs across the range of diameters noted in our PAM images. Lower total vascular length may be based in fewer vascular segments of resolvable diameters, shorter vascular segments of resolvable diameters, a difference in blood pooling and draining at sacrifice, or random differences within a small sample. The larger differences in total vascular length between genotypes at E13.5 suggest that differences might be more apparent earlier in the development of these large vessels, prior to initial frontal bone ossification. Measurements from mice that conditionally express the P253R mutation in endothelial cells supports the hypothesis that vessels are shorter in *Fgfr2*$^{+/P253R}$ specimens (Chapter 4), but future work is required to verify this. Total vessel length of larger diameter vessels appears to increase between E13.5 and E14.5 (Table 3.2). While vascular length probably continues to increase across the head after E14.5, relatively smaller portions of the head are imaged at each subsequent age, so the lack of change in this measure suggests a stable density of vessels per unit volume as the head grows. After the vessel diameter histograms are standardized by total vessel length, the mean histogram values for the two genotypes are very similar and display a peak at around 0.030mm. This peak does not increase between E13.5 and E16.5, suggesting that an optimal distribution of vessel diameters, in addition to vascular density, is achieved for larger vessels of the embryonic head at this time.

OCT Tissues

Although gross tissue morphology is similar within histological slices and OCT image slices, variation of voxel intensity within OCT images stem from differences in the backscattering of

tissues, rather than differences in the transmission of light through stained tissues (Boppart et al., 1996). Increased scattering occurs when there is a change in refractive index (speed of light) between adjacent materials. Refractive index changes within the resolution of our OCT imaging system appear as speckle or texture. Due to embryonic tissue heterogeneity, most tissue layers appear as speckled regions of varying intensity and texture. Regions of homogenous fluid or gas, such as the vitreous cavity of the eye, appear dark, because there is no refractive index change within that space. The image intensity of a tissue decreases with depth, because light has been scattered and absorbed by more superficial layers. Similarly, vertical artifacts occur across our OCT images, because of variation in the amount of backscattering across the FOV. Extreme vertical shadows occur deep to tissues with very high optical backscattering, like some of the large blood vessels in our images.

Superficial tissue layers are easier to differentiate within OCT images at older embryonic ages. This is due to a combination of increased tissue layer thickness and continued tissue differentiation between E13.5 to E16.5. Within histological sections, the first cortical layer of the brain becomes more obvious, because the layer deep to it increases in cell nucleus density between E13.5 and E16.5 (Kaufman, 1999), while the first layer of the cortex continues to display a relatively low density of nuclei. In OCT images, the first cortical layer becomes more hyperintense and easier to differentiate during this period as well. This relative hyperintensity may be directly related to the relative lack of large nuclei, because nuclei appear as hypointense regions within higher resolution OCT images that can pick up traits of individual organelles (Barton et al., 2007). However, the hyperintense nature of the layer could have another basis, because our moderate resolution OCT images are sensitive to both cell density and the combination of intracellular features.

The meningeal layers also become easier to differentiate from each other across the embryonic period. Previous work has shown that the three meningeal layers of pia, arachnoid, and dura

differentiate from a single meningeal layer starting at E14.5 near the initial sites of calvarial bone condensation. Then, this differentiation progresses towards the apex of the head along with the apical growth of associated calvarial bones (Vivatbutsiri et al., 2008). Supporting these observations, the meningeal layers are impossible to distinguish in our E13.5 OCT images, sometimes distinguishable in E14.5 images, and relatively easy to distinguish in E15.5 and E16.5 images. Additionally, they are easier to distinguish near the site of initial frontal bone ossification, just superior to the eye, than closer to the apex of the head. OCT imaging might allow for further noninvasive study of the meningeal layer development and maturation.

Although the eye was not the object of our interest, our combined OCT/PAM system produced OCT images that allowed many of its layers to be differentiated. OCT has been used to produce noninvasive images of eye tissues for many years (e.g. Hee et al., 1995; Boppart et al., 1996) and a number of OCT commercial imaging systems for use by opthomologists now exist (Keane et al., 2012). OCT produces high resolution cross-sectional slices of embryonic eyes within which many important layers can be differentiated. These images can be replicated *in vivo* across the life of the specimen (Boppart et al., 1996; Larina et al., 2012).

Except for neural features associated with vision (Costello et al., 2006; Kallenbach and Frederiksen, 2007), OCT has not been frequently used to image the central nervous system. This is likely because the deep location of brain tissues makes optical imaging impractical. However, many layers of the brain can be distinguished in OCT images of our E13.5 specimens. Given the small size of mouse embryos, OCT might be a useful way to measure gross volumes or thicknesses of major brain layers, including the ventricles, during embryonic brain development. Increased depth associated with lower resolution OCT images may allow the brain tissues of older embryos to be imaged as well.

Embryonic Frontal Bone in OCT

A major goal of this project was to determine the appearance of early mineralizing bone in OCT images, based on the comparison of registered OCT images and HRCT images, as well as previously produced histological slices. At E13.5 and E14.5, a thicker portion of the hypointense layer of loose connective tissue and mesenchyme, near the developing tactile follicle superior to the eye, matches the location of the mesenchymal condensation of the frontal bone in histological sections. Under close inspection, it also appears slightly more hyperintense than the rest of the connective tissue layer, perhaps reflecting the increased cellular density expected in a mesenchymal condensation.

Because the registration of HRCT images to OCT/PAM images is based on superficial skin landmarks rather than landmarks within the tissue, the registration of HRCT segmented bone to the OCT images is suboptimal, but is adequate to provide approximate bone location. At E15.5, the region near and deep to the developing tactile follicle coincides with the region across which registered HRCT images display early frontal bone ossification. Between E14.5 and E15.5, it becomes possible to distinguish a mesenchymal layer deep to the loose connective tissue layer in OCT images. By E16.5, the mesenchymal layer can be easily distinguished from other layers towards the apex of the head. These changes coincide with the known expansion of the calvarial bone mesenechymal condensations starting at E14.5 from the ossification centers towards the apex of the head (Chapter 1). Based on HRCT images, we expect the ossified portions of the frontal bone to be found curved deep around the superior half of the eye and superior to the eye at the same depth as the mesenchymal layer. Within OCT images, this corresponds with more hypointense regions of the mesenchymal layer at E15.5 and E16.5. Assuming this identification is accurate, the mineralized portions of the frontal bone are difficult to distinguish from surrounding tissues.

This result is surprising given that we expected the combination of regular collagen fibers

and higher mineral content of bone to appear different than surrounding soft tissue. Some previous attempts to image bone using OCT have also had limited success, including images of a nebulous border between more hypointense articular cartilage and slightly more hyperintense bone (Han et al., 2003) and the rough outlines of *in situ* ear ossicles (Pitris et al., 2001). However, more recently acquired OCT images clearly delineated bone trabeculae as hyperintense regions, including their lamellar structure (Kasseck et al., 2010). In our images, it is not clear why a more hypointense region of the mesenchymal layer might be associated with developing bones rather than a hyperintense portion, as seen in previous studies. Minerals replace a large volume of extracellular fluid that exists between the collagen fibers of bone matrix during bone mineralization (Heaney, 2008), so perhaps the earliest bone still contains large homogenous fluid spaces that appear as hypointense regions, while more highly mineralized adult bone appears more hyperintense. It is also possible that the decreased image intensity of the region associated with bone is caused by a shadow from the developing tactile follicle and thicker tissues surrounding the eye, which happen to be superficial to the frontal bone ossification center.

Summary

Although we were not able to map the wide microvascular network within developing superficial tissues of the head or definitively identify tissues of the developing frontal bone in our specimens, this study lays the groundwork for future studies of the association of blood vessels and developing calvarial bones. Our images and analysis illustrate the types of vessels and other soft tissues that can be resolved from OCT/PAM imaging of sacrificed embryos. The density and diameter of large blood vessels of superficial head tissues appear stable after E13.5, with major blood vessels around the developing frontal bone associated with three vascular groups. Our results suggest a relatively minor reduction in overall length of large vasculature in *Fgfr2*$^{+/P253R}$ mice when compared to *Fgfr2*$^{+/+}$, which

needs to be verified in future studies. OCT images provide the ability to distinguish many different superficial tissue layers in our embryonic specimens, which can provide a context for identifying vasculature and studying embryonic tissue layer differentiation. The use of a combined OCT/PAM imaging system allowed the identification of major tissue layers and blood vessels surrounding the developing frontal bone of sacrificed embryonic.

CHAPTER 4:
ENDOTHELIAL EXPRESSION OF THE *Fgfr2* P253R MUTATION INFLUENCES CRANIAL BONE DEVELOPMENT

INTRODUCTION

Fgfr2$^{+/P253R}$ mice display significant craniofacial dysmorphology including midfacial hypoplasia, premature fusion of some craniofacial sutures, abnormal cranial vault shape (Wang et al., 2010; Martínez-Abadías et al., 2010), as well as decreased bone volume and density of some bones during early ossification (Chapter 2). Because tissue interactions are critical for craniofacial development and *Fgfr2* is highly pleiotropic, pinpointing the developmental pathways modified to produce craniofacial dysmorphology is difficult. *Fgfr2* is known to be an important regulator of bone cell activity during initial skeletogenesis (Iseki et al., 1999; Eswarakumar et al., 2002; Ornitz and Marie, 2002) and some *Fgfr2* mutations are associated with craniosynostosis syndromes (Cohen Jr and Maclean, 2000). However, FGFR2 is part of a family of receptors whose members are also associated with regulating endothelial cells (Suhardja and Hoffman, 2003) and some of the ligands it interacts with are known angiogenesis factors (Javerzat et al., 2002). *Fgfr2* mutations may influence endothelial cell activity, because this gene is expressed in endothelial cells, including a line derived from murine brain capillaries (Kanda et al., 1996). Inhibition of FGFR2 in rat glioma cells reduces the vascularity and associated growth of resulting tumors (Auguste et al., 2001), suggesting that FGFR2 signaling plays an important role in promoting angiogenesis in some contexts. Specifically, FGFR2 has been shown to regulate cell migration but not proliferation of brain capillary endothelial cells (Nakamura et al., 2001), although the generalizability of this observation has been questioned (Javerzat et al., 2002). Regardless, it appears

that FGFR2 plays a role in regulating angiogenesis, which is critical for normal bone ossification and development (Chapter 1). Therefore, we hypothesize that at least a portion of the craniofacial skeletal dysmorphology previously noted in *Fgfr2*$^{+/P253R}$ mice is secondary to the dysregulation of angiogenesis.

Comparisons of vasculature associated with the forming frontal bone in *Fgfr2*$^{+/P253R}$ mice and their unaffected littermates between E13.5 and E16.5 suggested lower total length of large vessels, but roughly similar distributions of vessel diameters and vessel density per unit volume (Chapter 3). However, these results are suggestive at best and represent measures of the largest vessels in the region, while growing capillaries, among the smallest diameter vessels, are those that directly interact with bone forming osteoblasts (Chapter 1). Therefore, the microvasculature directly associated with the angiogenesis of developing bones has not been studied, because of sub-adequate imaging. Here, we measure the effect of conditional expression of the P253R mutation within endothelial cells on bone morphogenesis. This conditional expression should remove the direct effect of the mutation on bone cell activity, leaving only the indirect effect of its expression within vascular cells that form the basis of new vessels during angiogenesis. We hypothesize that these mice will display bone dysmorphology when compared to their unaffected littermates, although this dysmorphology will not be as severe as noted in the *Fgfr2*$^{+/P253R}$ mice.

METHODS

Sample and Imaging

Mice heterozygous for the P253R *Fgfr2* mutation with neo (+/P253Rneo) (Wang et al., 2010) were bred with Tek-cre hemizyogotes (-/+) (The Jackson Laboratory; Kisanuki et al., 2001) to remove the neo cassette within endothelial cells. This leads to litters with four possible genotypes with similar numbers (Table 4.1). Mice of the first genotype *Tek*$^{+/-}$*; Fgfr2*$^{+/P253R}$ are heterozygous for the P253R mutation and hemizygous for Tek-cre; so should express the P253R mutation in endothelial cells

Table 4.1 The number of specimens of each genotype used during Landmark based analyses (LandM) and Volume/Density analyses (Vol/Den) for P0 and P8, including the voxel size and slice thickness of associated HRCT images.

	P0		**P8**	
Genotype	LandM	Vol/Den	LandM	Vol/Den
$Tek^{-/-}$; $Fgfr2^{+/+}$	10	12	4	4
$Tek^{-/-}$; $Fgfr2^{+/P253Rneo}$	24	22	7	7
$Tek^{+/-}$; $Fgfr2^{+/P253R}$	14	9	4	4
Voxel Size	13.8 μm		19.8 μm	
Slice Thickness	15.4 μm		21.8 μm	

only. *$Tek^{-/-}$; $Fgfr2^{+/P253Rneo}$* mice are heterozygous for the P253R mutation, but lack Tek-cre, so the associated neo cassette should prevent its expression. *$Tek^{+/-}$; $Fgfr2^{+/+}$* and *$Tek^{-/-}$; $Fgfr2^{+/+}$* mice lack the P253R mutation. All except the first should not express the P253R mutation and serve equally well as littermate controls for the *$Tek^{+/-}$; $Fgfr2^{+/P253R}$* mice. Because the *$Tek^{+/-}$; $Fgfr2^{+/+}$* mice have a very similar genotype to the controls of *$Fgfr2^{+/P253R}$* mice (Chapter 2) and because they do not differ grossly from the other two control genotypes, we ignore this genotype in our analyses.

Based upon timed matings and evidence of pregnancy, litters were sacrificed at postnatal days zero (P0) and eight (P8) with inhalation anesthetics and fixed in 4% paraformaldehyde. Care and use of mice for this study were in compliance with relevant animal welfare guidelines approved by Penn State University Animal Care and Use Committee. High resolution micro-computed tomography (HRCT) images of mouse heads (Table 4.1) were acquired in air at the Center for Quantitative X-Ray Imaging at Pennsylvania State University (www.cqi.psu.edu) using an OMNI-X Universal HD600 industrial x-ray computed tomography system (Varian Medical Systems, Palo Alto CA) with source energy settings of 130kVp/0.15mA, projection time of 66.7ms with 2400 projections and 3-6 frame averaging over 360 degree rotation. Solid hydroxyapatite phantoms (QRM GmbH, Möehrendorf, Germany) scanned with each set of skulls allowed for relative x-ray attenuation values to be associated with bone mineral density estimates (Fig 2.1).

To verify that Tek-cre serves to remove neo cassettes extensively and exclusively in vascular endothelial cells, we bred Tek-cre hemizygotes (-/+) with R26 Rosa reporter homozygotes (+/+) (The Jackson Laboratory; Soriano, 1999). A few *Tek*$^{+/-}$*; Rosa*$^{+/+}$ mice and *Tek*$^{-/-}$*; Rosa*$^{+/+}$ littermates were stained with LacZ and cleared in glycerol at embryonic day 17.5 (E17.5) (Schatz et al., 2005; Kawaguchi et al., 2002). The resulting whole mount cleared and stained specimens were studied and photographed under a dissection microscope in order to determine the cells within which Tek-cre allows expression of Rosa and, by proxy, allows the expression of the P253R mutation in the *Tek*$^{+/-}$*; Fgfr2*$^{+/P253R}$ mice.

Landmark Identification and Analysis

Three-dimensional coordinate locations 25 P0 and 29 P8 anatomical landmarks (Figs 4.1, 4.2; Table 4.2) were recorded for each specimen using a custom landmarking tool in Avizo 3D analysis software (Visualization Sciences Group, Burlington MA). These biologically relevant landmarks were chosen to evenly cover the cranium and to allow for comparisons of cranial form between ages, genotypes, and with results from previous studies. Most of the landmarks have been previously defined for other studies within the Richtsmeier Lab (www.getahead.psu.edu). Landmarks were manually placed on 3D isosurface reconstructions of skulls from HRCT images, based on a minimum threshold of 62 mg/mm^3 partial density of hydroxyapatite. This minimum threshold is lower than that used in previous studies (Percival et al., 2012; Chapter 2), but was chosen to include lower density portions of developing bones in perinatal mice while still excluding the vast majority of unossified tissue. To minimize measurement error, two landmark collection trials were completed for each specimen and the average coordinates were used for subsequent analyses. Previous analyses have demonstrated the accuracy and precision of this data collection method for HRCT scans (Corner et al., 1992; Richtsmeier et al., 1995).

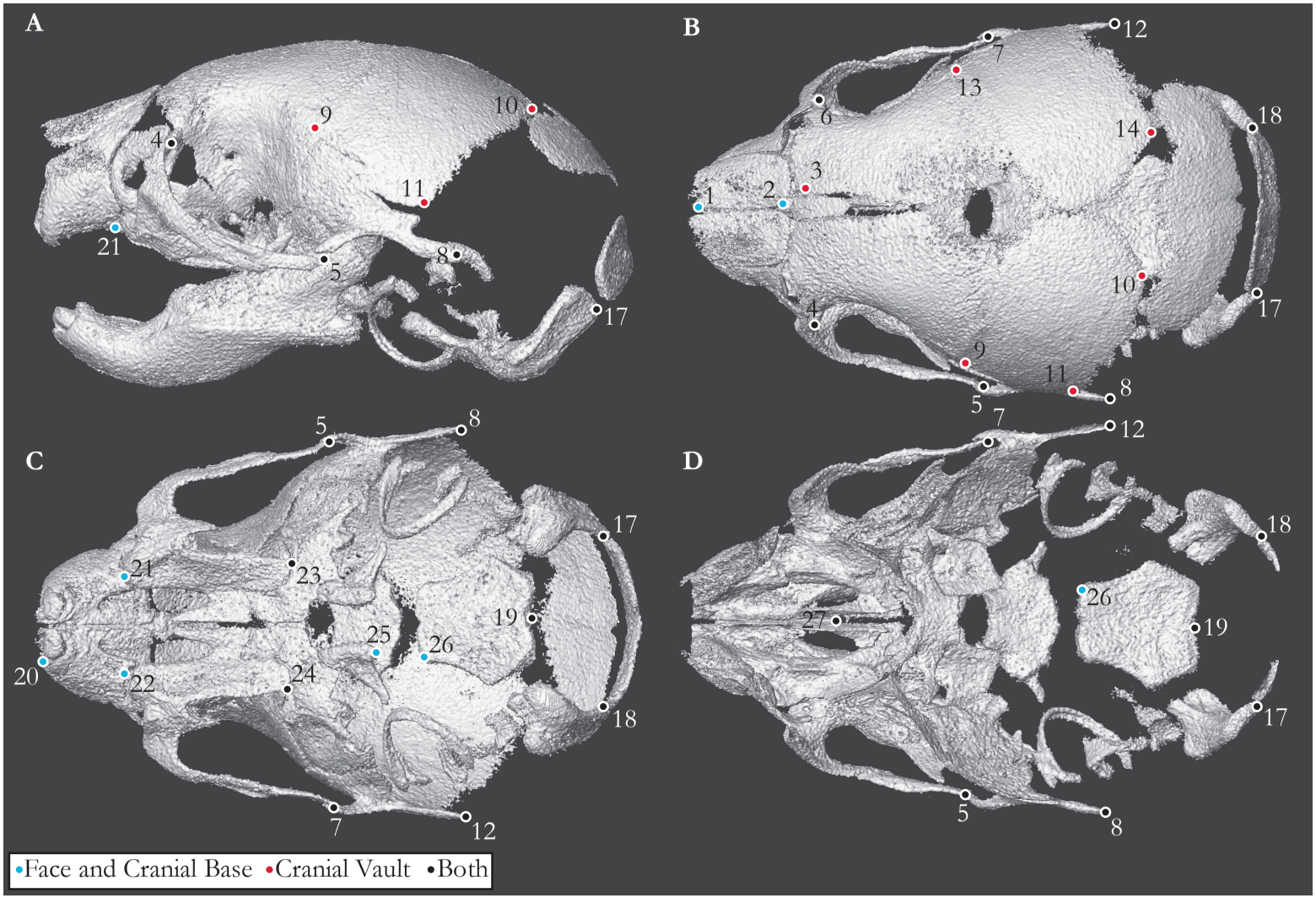

Fig 4.1 The locations of landmarks used for EDMA Form analyses of the face-cranial base (blue), the vault (red), or both (black) on surface reconstructions of an HRCT image of a P0 mouse head from the following views: (A) left lateral, (B) superior, (C) inferior with mandible removed, and (D) superior with the calotte removed. All landmarks were used for MorphoJ analyses. Landmark numbers correspond to those listed in table 4.2.

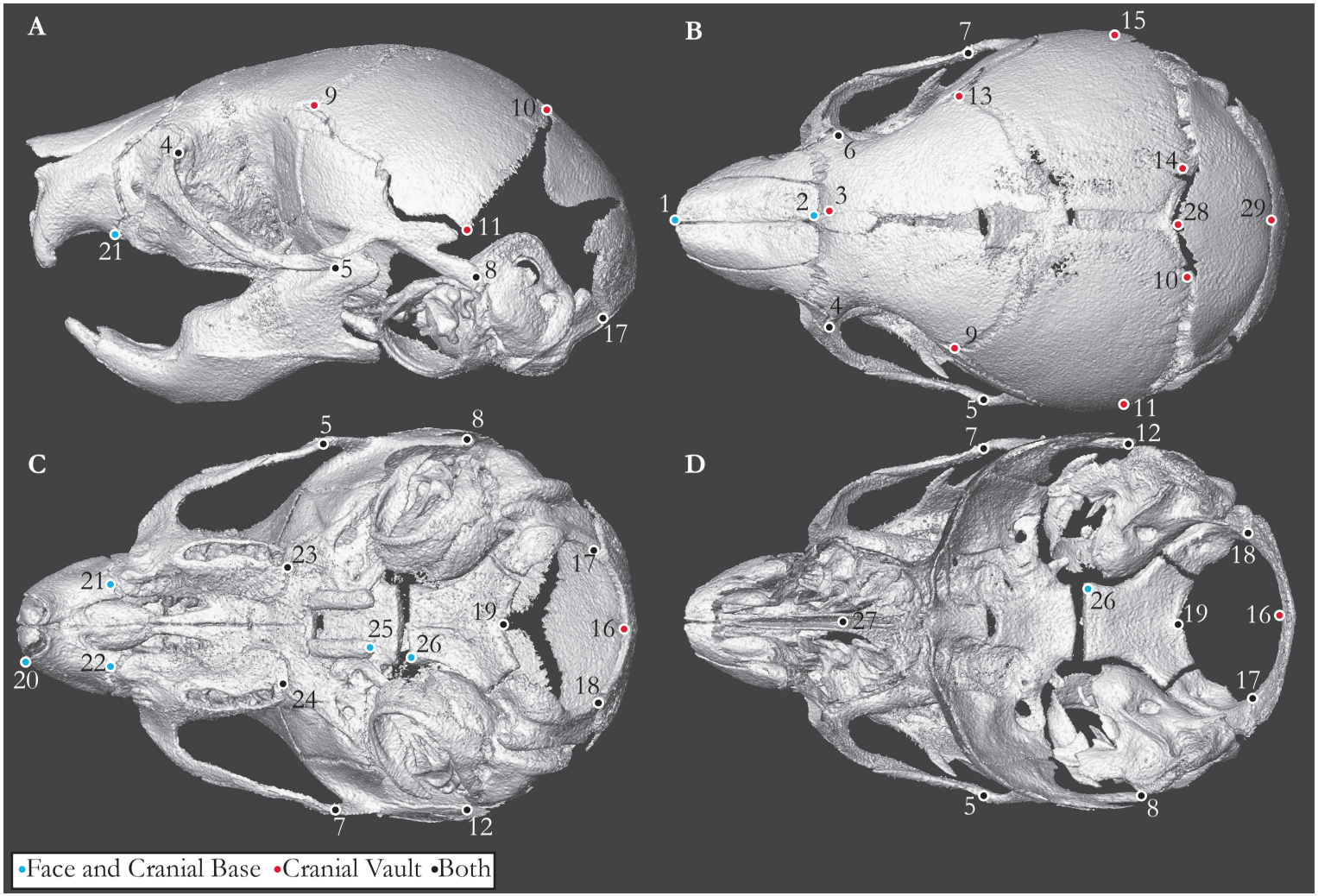

Fig 4.2 The locations of landmarks used for EDMA Form analyses of the face-cranial base (blue), the vault (red), or both (black) on surface reconstructions of an HRCT image of a P8 mouse head from the following views: (A) left lateral, (B) superior, (C) inferior with mandible removed, and (D) superior with the calotte removed. All landmarks were used for MorphoJ analyses. Landmark numbers correspond to those listed in table 4.2.

Table 4.2 Definitions for EDMA Form analysis of face-cranial base (F-B) and the cranial vault landmarks for P0 and P8 specimens. MorphoJ analyses included all landmarks simultaneously. Landmark numbers correspond to those in figs 4.1 and 4.2.

	P0		P8			
Number	**F-B**	**Vault**	**F-B**	**Vault**	**Name**	**Definition**
1	y		y		rnsla	Most antero-medial point of the right nasal bone
2	y		y		rnslp	Most postero-medial point of the right nasal bone
3		y		y	ramf	Most medio-anterior point of right frontal bone
4	y	y	y	y	lflac	Intersection of frontal process of maxilla with frontal and lacrimal bones, left side
5	y	y	y	y	lzyt	Intersection of zygoma with zygomatic process of temporal, taken on zygoma, left side
6	y	y	y	y	rflac	Intersection of frontal process of maxilla with frontal and lacrimal bones, right side
7	y	y	y	y	rzyt	Intersection of zygoma with zygomatic process of temporal, taken on zygoma, right side
8	y	y	y	y	lpsq	Most posterior point on the posterior extension of the left squamous temporal
9		y		y	lpfl	Most lateral intersection of the frontal and parietal bones, taken on the left parietal
10		y		y	lpto	Most postero-medial point on the left parietal
11		y		y	lpip	Most postero-inferior point on the left parietal
12	y	y	y	y	rpsq	Most posterior point on the posterior extension of the right squamous temporal
13		y		y	rpfl	Most lateral intersection of the frontal and parietal bones, taken on the right parietal
14		y		y	rpto	Most postero-medial point on the right parietal
15				y	rpip	Most postero-inferior point on the right parietal
16				y	opi	Mid-point on the anterior margin of the foramen magnum, taken on basioccipital
17	y	y	y	y	loci	The superior posterior point on the ectocranial surface of the left lateral occipital
18	y	y	y	y	roci	The superior posterior point on the ectocranial surface of the right lateral occipital
19	y	y	y	y	bas	Mid-point on the posterior margin of the foramen magnum, taken on squamosal occipital
20	y		y		rpmsp	Anterior superior edge of the right premaxilla at the nasal aperture
21	y		y		lpmx	Most infero-lateral point of the premaxillary-maxillary suture, taken on the left premaxilla
22	y		y		rpmx	Most infero-lateral point of the premaxillary-maxillary suture, taken on the right premaxilla
23	y	y	y	y	lmma	Posterior lateral point on the maxillary portion of the left medial alveolus
24	y	y	y	y	rmma	Posterior lateral point on the maxillary portion of the right medial alveolus
25	y		y		rptyp	Most posterior tip of the medial right pterygoid process
26	y		y		rsyn	Most antero-lateral point on corner of the right basioccipital
27	y	y	y	y	ethmp	Most posterior point on the body of the vomer
28				y	pari	The anterior midline point on the interparietal bone
29				y	paro	The midline superior point of the squamous occipital bone

Differences in skull shape were assessed using Euclidian Distance Matrix Analysis (EDMA) (Lele and Richtsmeier, 1991), which transforms 3D landmark coordinates into linear distances between landmarks for further analysis. Specimens with skulls damaged during HRCT imaging or those with abnormal asymmetrical morphology were not included in this analysis. Two subsets of landmarks with coordinates for all included specimens and with relatively low landmark placement error were analyzed separately: cranial face-base and cranial vault (Table 4.2; Figs 4.1, 4.2). Within each age category and for both landmark subsets, three pairwise EDMA Form analyses were completed to compare the three genotypes of interest. EDMA Form analysis is based on calculations of the ratio between the average linear distances of two genotypes for each possible linear distance. The null hypothesis that two genotypes display similar length for a linear distance was rejected if a 90% confidence interval, estimated from 1000 iterations of a bootstrapping algorithm, did not include the value of 1. Rejection of the null hypothesis enables localization of differences to specific landmarks and linear distances.

Centroid size, a measure of scale, of each specimen was calculated as the square root of the sum of squared distances of all landmarks from their center of gravity (e.g. Bookstein, 1996), using MorphoJ software (Klingenberg, 2011). To test whether skull scale differs between the genotypes at each age, pair-wise 2-sample Wilcoxon (Mann-Whitney) tests of centroid sizes were completed in R (R Developmental Core Team, 2008). To determine whether the relationship between skull size and skull shape differed between genotypes at each age, using MorphoJ, we performed a multivariate regression of Procrustes landmark coordinates for each landmark against the independent variable of centroid size and plotted the regression summary score against centroid size of each specimen at P0 and P8. The regression summary score represents the shape changes for which the regression against centroid scores account (Drake and Klingenberg, 2008). We explored whether the relationship between shape change and size differed among the genotypes at either age by labeling specimens by their genotype.

Bone Volume and Density Measurement

Semi-automatic segmentation (Percival et al., 2012) was performed within Avizo 3D analysis software to identify the individual craniofacial bones of each specimen, based on a minimum bone threshold of 74 mg/mm^3 partial density of hydroxyapatite; the threshold used for volume and relative density analysis of *Fgfr2*$^{+/P253R}$ mice (Chapter 2). Manually segmented P0 and P8 *Tek-cre*$^{-/-}$*; Fgfr2*$^{+/+}$ reference specimens served as the basis for the semi-automatic segmentation other specimens of the same age. Teeth were manually segmented separately for each specimen and removed from analysis in order to avoid confounding tooth with the surrounding bone. A subset of relatively large midline and left side craniofacial bones with low segmentation error were included in our analysis (Figs 4.3-4.5): interparietal (IPar), squamous occipital (SquO), lateral occipital (LatO), basi-occipital (BasO), parietal (Par), frontal including lacrimal (Fro), maxilla (Max), nasal (Nas), premaxilla (PMax), palatine including pterygoid (Pal), presphenoid (PSph), sphenoid ala (SphA), sphenoid body (SphB), petrous temporal (PetT), mandible (Man), and ethmoid (Eth). These are the same bones as used for previous analysis of *Fgfr2*$^{+/P253R}$ mice (Chapter 2), with the exception of SquT, which was not included because of high segmentation error for P8 specimens. Eth was added because it is significantly ossified by P8. Specimens with relatively high bone identification error, rather than relatively high shape deformation, were excluded from our volume/density analysis; leading to a different set of specimens analyzed than during landmark based analysis (Table 4.1).

Bone density histograms, bone volumes, and standardized bone density histograms were calculated for all bones in our analysis, as previously described (Chapter 2). The resulting histograms contain 126 values for each craniofacial element between the minimum bone density of 74 and a maximum density value of 372 mg/mm^3 partial density of hydroxyapatite. Because of image saturation for some bones, the values for the highest bone densities may include voxels of bone above

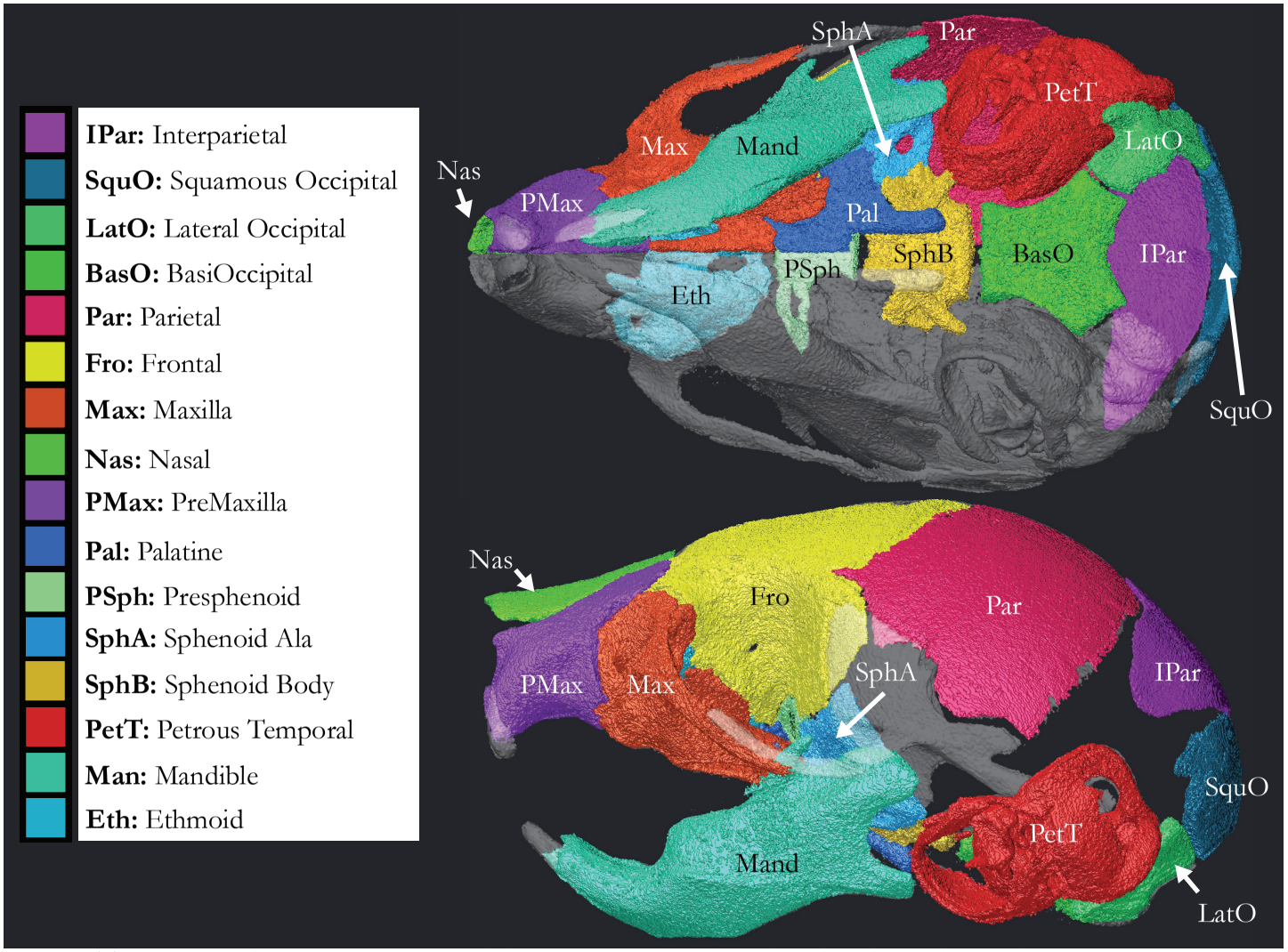

Fig 4.3 The subset of bones analyzed and their abbreviations, as identified from the surface reconstruction of a HRCT image of a P8 *Tek*$^{-/-}$; *Fgfr2*$^{+/P253Rneo}$ specimen from the inferior view (top) and the left lateral view (bottom). Bones being analyzed are brightly colored, while the rest of the skull is transparent grey. Bone abbreviations defined here are used throughout the text and figures of this chapter.

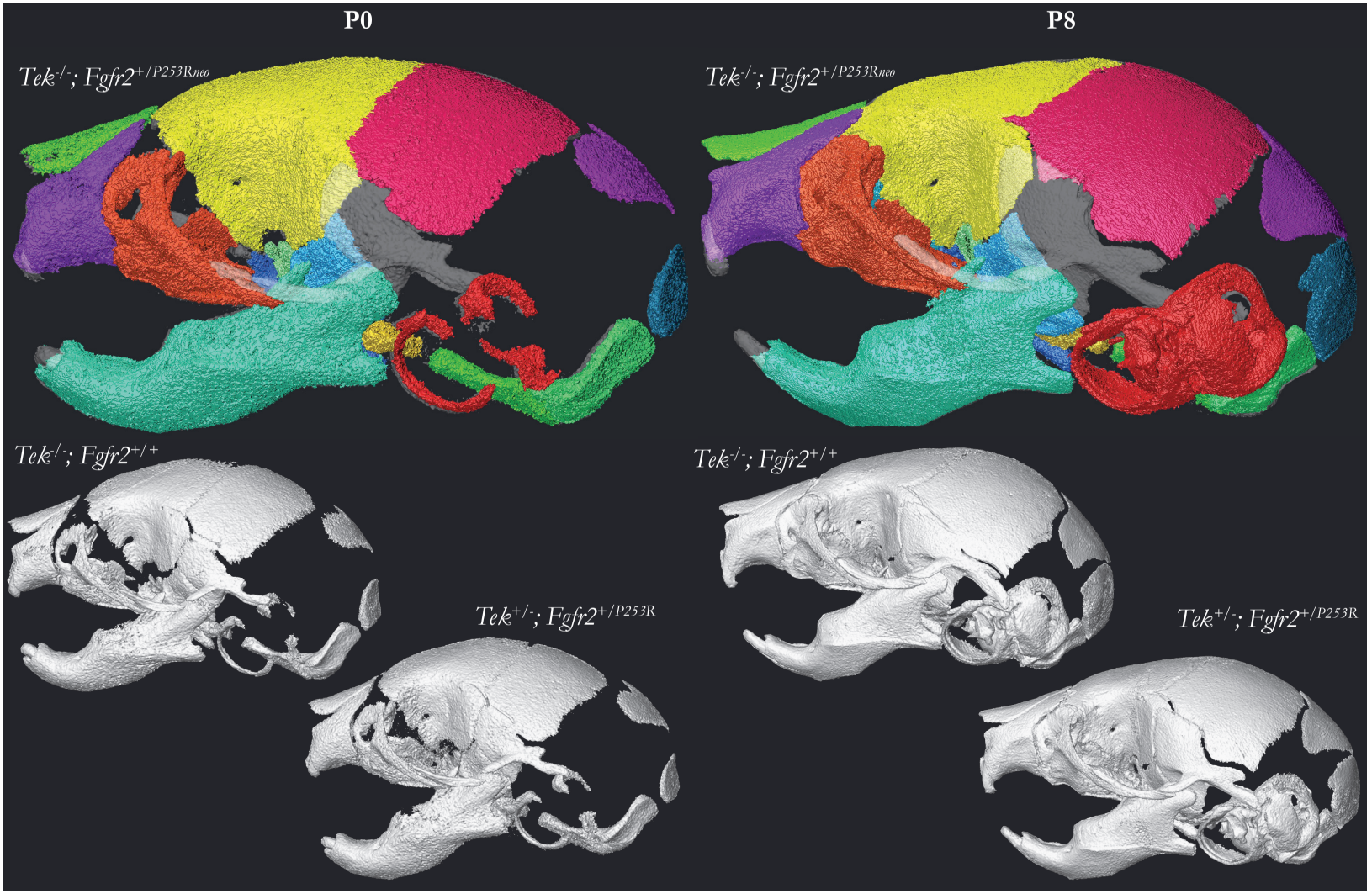

Fig 4.4 Bones of analysis identified from the left lateral view of HRCT image surface reconstructions of representative specimens of each genotype at P0 and P8. *Tek*$^{-/-}$*; Fgfr2*$^{+/P253Rneo}$ bones being analyzed are brightly colored, while the rest are transparent grey. Smaller, grey skulls of *Tek*$^{-/-}$*; Fgfr2*$^{+/+}$ and *Tek*$^{+/-}$*; Fgfr2*$^{+/P253R}$ mice are presented for comparison of cranial morphology. None of the visually identifiable dysmorphology of the *Fgfr2*$^{+/P253R}$ Apert syndrome mice is displayed by specimens of our current sample at either age. The anterior aspect of the skulls is to the left and superior is up. Images are not to scale.

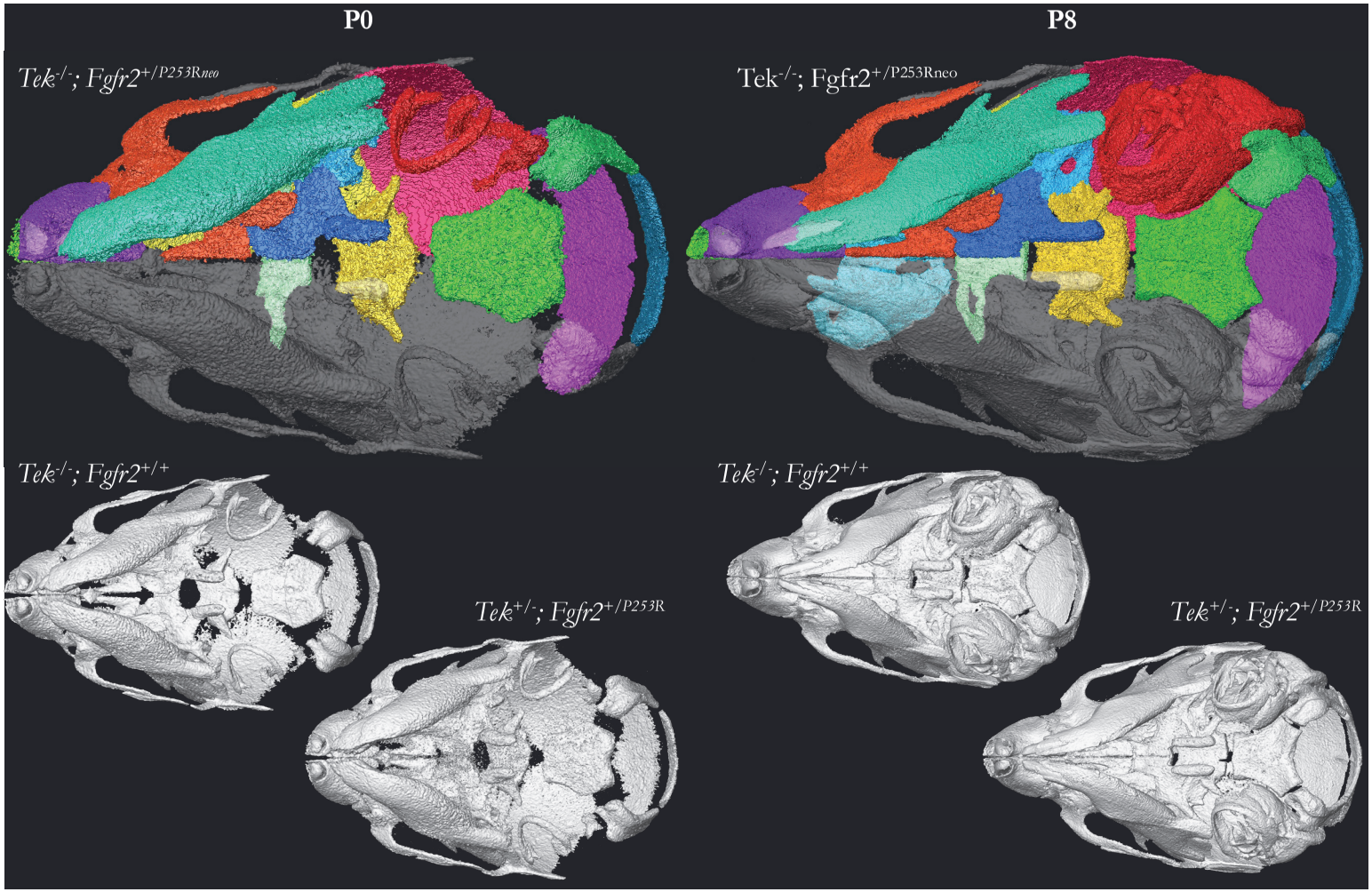

Fig 4.5 Bones of analysis identified from the inferior view of HRCT image surface of reconstructions representative specimens of each genotype at P0 and P8. *Tek*$^{-/-}$*; Fgfr2*$^{+/P253Rneo}$ bones being analyzed are brightly colored, while the rest are transparent grey. Smaller, grey skulls of *Tek*$^{-/-}$*; Fgfr2*$^{+/+}$ and *Tek*$^{+/-}$*; Fgfr2*$^{+/P253R}$ mice are presented for comparison of cranial morphology. None of the visually identifiable dysmorphology of the *Fgfr2*$^{+/P253R}$ Apert syndrome mice is displayed by specimens of our current sample at either age. The anterior aspect of the skulls is to the left and left lateral is up. Images are not to scale.

the maximum bone density. Mean total bone volumes, calculated for each age-genotype combination, serve as a proxy for bone size, while differences in volume between ages represent bone growth. Mean volumes standardized by the total bone volume of the 16 bones under study represent relative bone development for each age-genotype combination. In order to identify differences in volume between genotypes, pairwise comparisons of individual bone volumes were completed between genotypes at both ages with 2-sample Wilcoxon (Mann-Whitney) tests in R, including Bonferroni correction for multiple testing.

Relative density curves derived from standardized density histograms serve as a proxy for bone maturation. Mean curves of a combination of *Tek*$^{-/-}$*; Fgfr2*$^{+/+}$ and *Tek*$^{-/-}$*; Fgfr2*$^{+/P253Rneo}$ specimens were plotted at P0 and P8 to represent the "normal" bone maturation of each bone and to investigate whether bones cluster by patterns of bone maturation across the early postnatal period. Using the *Tek*$^{-/-}$*; Fgfr2*$^{+/+}$ as a baseline, functional data analysis was completed, using the fda package in R (Ramsay et al., 2009), to determine the influence of endothelial expression of the P253R mutation on bone maturation across the early postnatal period. Because image saturation in some bones would have a strong artificial influence on functions estimated from histograms, the five highest bone density values were discarded during functional analysis. Using the remaining 121 values from the standardized histograms, cubic spline functions were estimated for each bone using 5 knots. A functional multivariate regression was computed for each bone with two genotype dummy variables and age as a binary variable. Additionally, separate regressions that included age*genotype interaction terms were calculated, but we report only the results of the regression without interaction terms, because their inclusion did not alter the results of the analysis significantly.

$$E(y_i(d)) = \beta_0(d) + \beta_1(d)\, I_1 + \beta_2(d)\, I_2 + \beta_3(d)\, Age$$

A functional multivariate regression was computed for each bone separately for both ages in

order to investigate whether the bone maturation at one age masked weakly significant differences found in the other age.

$$E(y_i(d)) = \beta_0(d) + \beta_1(d)\, I_1 + \beta_2(d)\, I_2$$

In all of these regression models, d refers to bone density values, I_1 and I_2 are genotype identities *Tek*$^{-/-}$*; Fgfr2*$^{+/P253Rneo}$ and *Tek*$^{+/-}$*; Fgfr2*$^{+/P253R}$, respectively, and *Age* represents the postnatal age of the specimen. Because Eth does not exist as an ossified bone at P0, a regression was only completed for it during the analysis of P8 measurements. 95% confidence intervals of the resulting coefficient curves were computed to determine whether the associated covariate had a significant effect of relative bone density curves.

RESULTS

Whole mount staining of E17.5 *Tek*$^{+/-}$*; Rosa*$^{+/+}$ mice reveal staining of apparently complete vasculature, while littermates without Tek-cre displays no staining (Fig 4.6). This supports our assumption that Tek-cre expression removes neo cassettes exclusively and extensively across vascular endothelial cells, leading to heterozygous expression of the P253R *Fgfr2* mutation in endothelial cells of *Tek*$^{+/-}$*; Fgfr2*$^{+/P253R}$ mice.

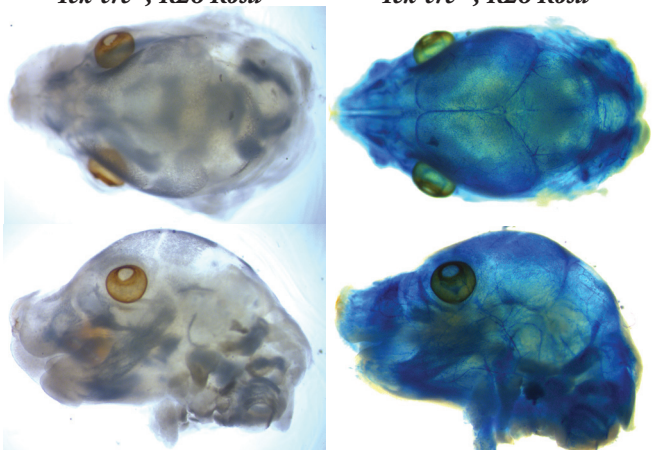

Fig 4.6 Superior (top) and left lateral (bottom) images of cleared LacZ mice stained for expression of R26 Rosa for a *Tek-cre*$^{+/-}$*; R26 Rosa*$^{+/+}$ mouse and T*ek-cre*$^{-/-}$*; R26 Rosa*$^{+/+}$ control. Staining indicates that Tek-cre successfully removed the neo cassette associated with R26 Rosa across the extensive vascular network of the *Tek-cre*$^{+/-}$*; R26 Rosa*$^{+/+}$ mouse, but within no cells of the control.

Normal Growth

The changes in individual bone volume and relative density noted in our sample have the potential to expand our understanding of the normal postnatal pattern of bone growth and maturation in mice until P8. The volumes of individual

bones at P0 (Fig 4.7), relative to overall ossified volume, are similar to those reported in our study of *Fgfr2*$^{+/P253R}$ mice (Fig 2.9). Between P0 and P8, a major shift in the relative volume of a few bones occurs. Man, which accounts for the highest volume of the skull at all previously reported ages is rivaled in size by PetT at P8. Eth, which displayed no ossified volume at P0, displays the third highest relative volume at P8.

The normal mean standardized bone density curves, which represent a combination of data from both control genotypes, indicate that each bone approaches a similar level of bone maturation by P8. Most bones increase in relative density via a reduction in slope of their relative density curves between P0 and P8. The variation of this pattern of density change is represented by Pal (Fig 4.8A), Fro (Fig 4.8B), and Man (Fig 4.8C), but Max, Par, PMax, PSph, and SphA also mature in this manner. BasO (Fig 4.8D), LatO, and SphB start with high relative densities at P0, but increase further via the movement of a peak in their curves towards higher density values. PetT (Fig 4.8E), IPar, Nas, and SquO have relatively low relative density at P0, while Eth (Fig 4.8F) has no ossified material. However, these five bones still mature into relatively dense bones by P8, although not quite as dense as the others. While the pace at which relative bone density increases differs between bones, the relative densities of all bones at P8 are similar.

Functional multivariate regressions

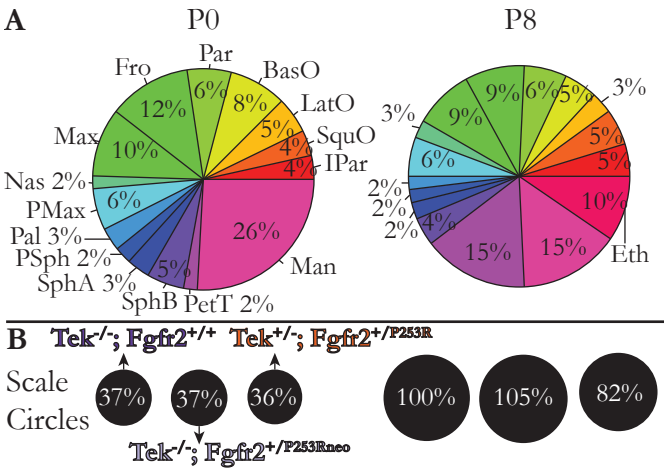

Fig 4.7 (A) Pie charts illustrating the mean relative volume of each bone under analysis compared to the mean total volume of all bones under analysis at P0 and P8. *Tek*$^{-/-}$*; Fgfr2*$^{+/+}$ values are used, because genotypes do not differ for these values. (B) Scale circles illustrating the mean total bone volume of each age-genotype category in relation to the P8 *Tek*$^{-/-}$*; Fgfr2*$^{+/+}$ value. The area of each circle is proportional to the mean total bone volumes. These values differ strongly across ages. The *235rm* also appears to differ from the two control genotypes at P8, although this difference is not significant.

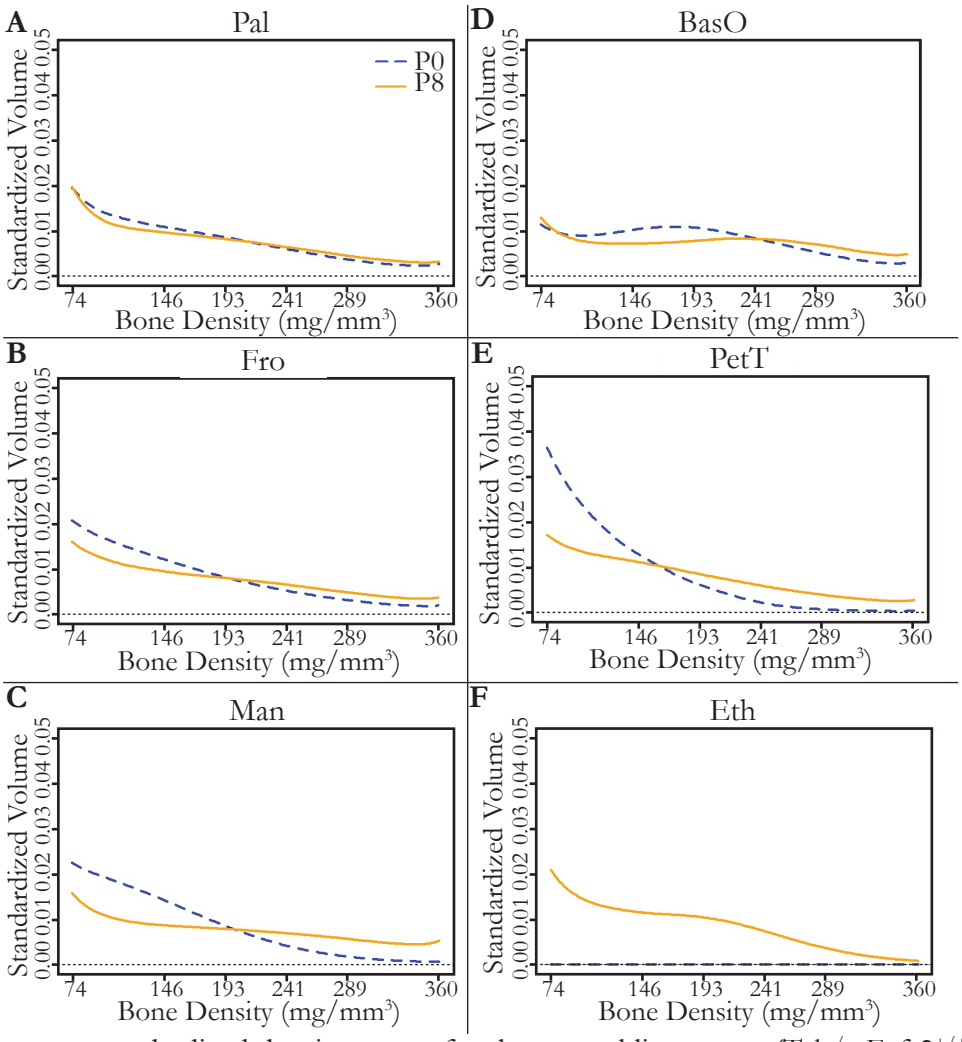

Fig 4.8 The mean standardized density curves for the control littermates ($Tek^{-/-}$; $Fgfr2^{+/+}$ and $Tek^{-/-}$; $Fgfr2^{+/P253Rneo}$) at P0 and P8 for a representative subset of bones. (A) Pal, (B) Fro, and (C) Man bone maturation represent most bones between P0 and P8; relative density increases as the relative density curves become more horizontal, leading to similar relative density curves at P8. (D) BasO represents a few endochondral bones; increasing in relative density through the movement of a peak frequency towards higher densities. (E) PetT represents bones that have low relative densities at P0, (F) is completely unossified at P0, but both reach a similar relative density to most bones by P8.

that included both ages indicated that age is a significant factor in influencing relative bone density, as measured from standardized density histogram curves. With P0 serving as the baseline, an increase in age to P8 is generally associated with a reduction in the proportion of lower density bone and an increase in the proportion of higher density bone. For bones that started at a higher relative density at P0, the age coefficient curve appears more like a sine curve (Fig 4.9A). Bones that started with a lower relative density at birth tend to display a single convex curve (Fig 4.9B). Bucking the trend, age does

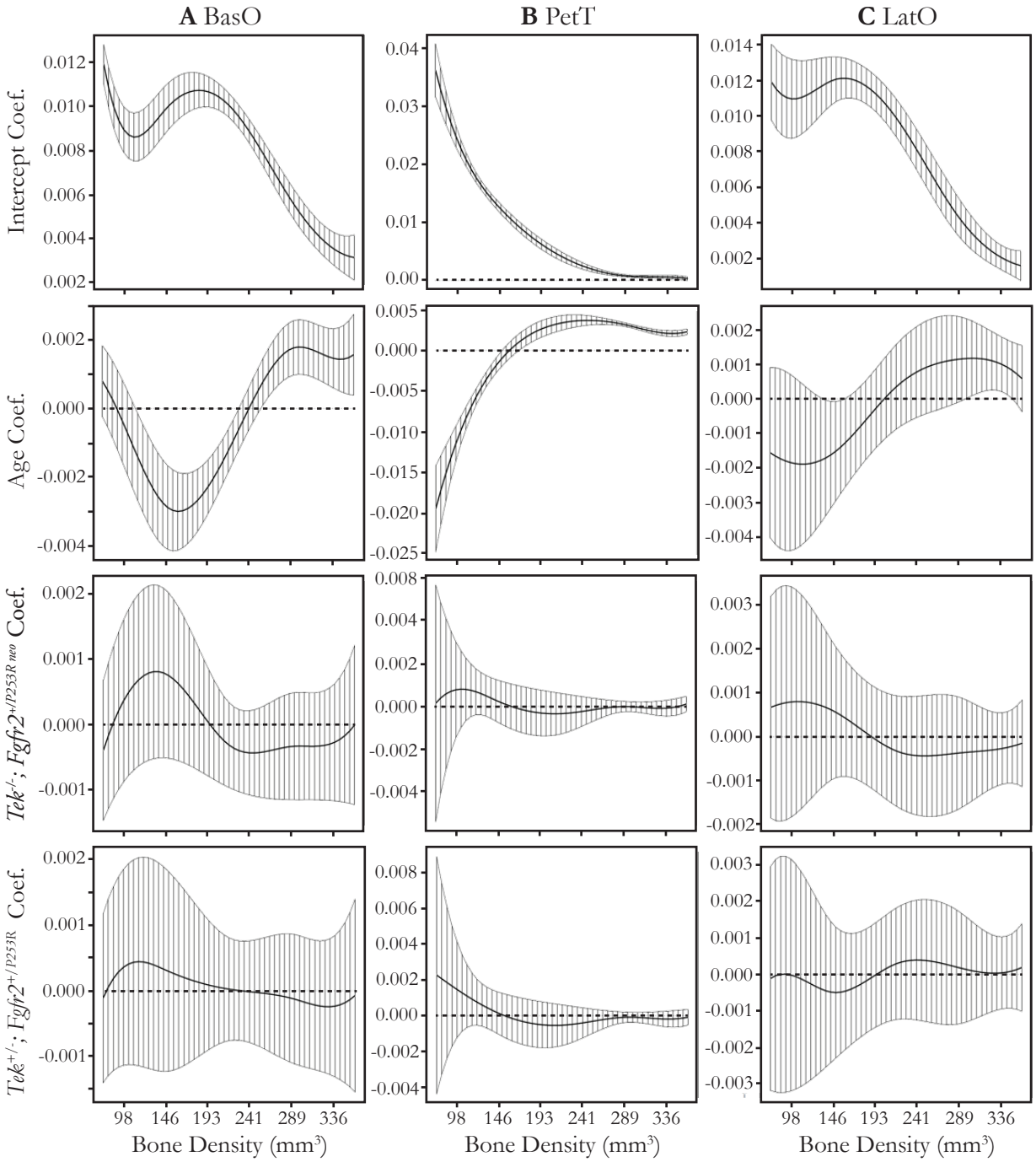

Fig 4.9 The functional intercept, age, and genotype coefficients, with 95% confidence intervals from the multivariate regressions of standardized bone density curves for three bones. The baseline for the regressions are P0 $Tek^{-/-}$; $Fgfr2^{+/+}$ mice, with identity coefficients for the other two genotypes. (A) BasO and (B) PetT both display a significant age effect, as most bones do. (C) LatO does not display a significant age effect between P0 and P8. None of the bones display a significant effect of genotype for this set of multivariate regressions.

not display a significant effect on relative bone density for LatO (Fig 4.9C) and displays a significant effect across a limited range of density values for Pal.

Tek$^{+/-}$*; Fgfr2*$^{+/P253R}$ Genotype Effect

EDMA Form analysis revealed that the two control genotypes display similar cranial dimensions at P0 and P8, based on the clustering of linear distance ratios around the value of one (Fig 4.10). Comparisons of controls and *Tek*$^{+/-}$*; Fgfr2*$^{+/P253R}$ mice, which served as the denominator of the linear distance ratios, displayed clustering of the ratio estimates above one at P0 and P8 for face-base and vault landmarks (Fig 4.10), suggesting that the *Tek*$^{+/-}$*; Fgfr2*$^{+/P253R}$ mice have shorter skull linear distance measurements. In many cases, the 90% bootstrap based confidence interval did not include the value of one, indicating a significant difference in linear distance between the two genotypes. While many of the estimated ratios that are most different from one represent height and length of the face, a similar proportion of all types of measures across the skull are significantly different. These results suggest that the linear scale of the *Tek*$^{+/-}$*; Fgfr2*$^{+/P253R}$ mice is reduced compared to the control genotypes, with no portion of the skull being more affected than others.

While the distribution of *Tek*$^{+/-}$*; Fgfr2*$^{+/P253R}$ centroid sizes, a measure of scale, represents the lower half of the control distributions, the differences in centroid size are not significant ($\alpha = 0.05$) at P0 or P8. However, the trend of a smaller skull for this genotype matches the results of the EDMA Form analysis. Based on similarities in the linear distribution of the multivariate regression summary score against centroid size (Fig 4.11), it appears that the relationship between cranial shape and size is similar across the genotypes at P0 and P8. However, the *Tek*$^{+/-}$*; Fgfr2*$^{+/P253R}$ specimens appear to be represented only by smaller specimens.

The mean overall ossified volume of *Tek*$^{+/-}$*; Fgfr2*$^{+/P253R}$ mice does not differ substantially from the control genotypes at P0, but is tantalizingly lower at P8 (Fig 4.7); although the difference is not

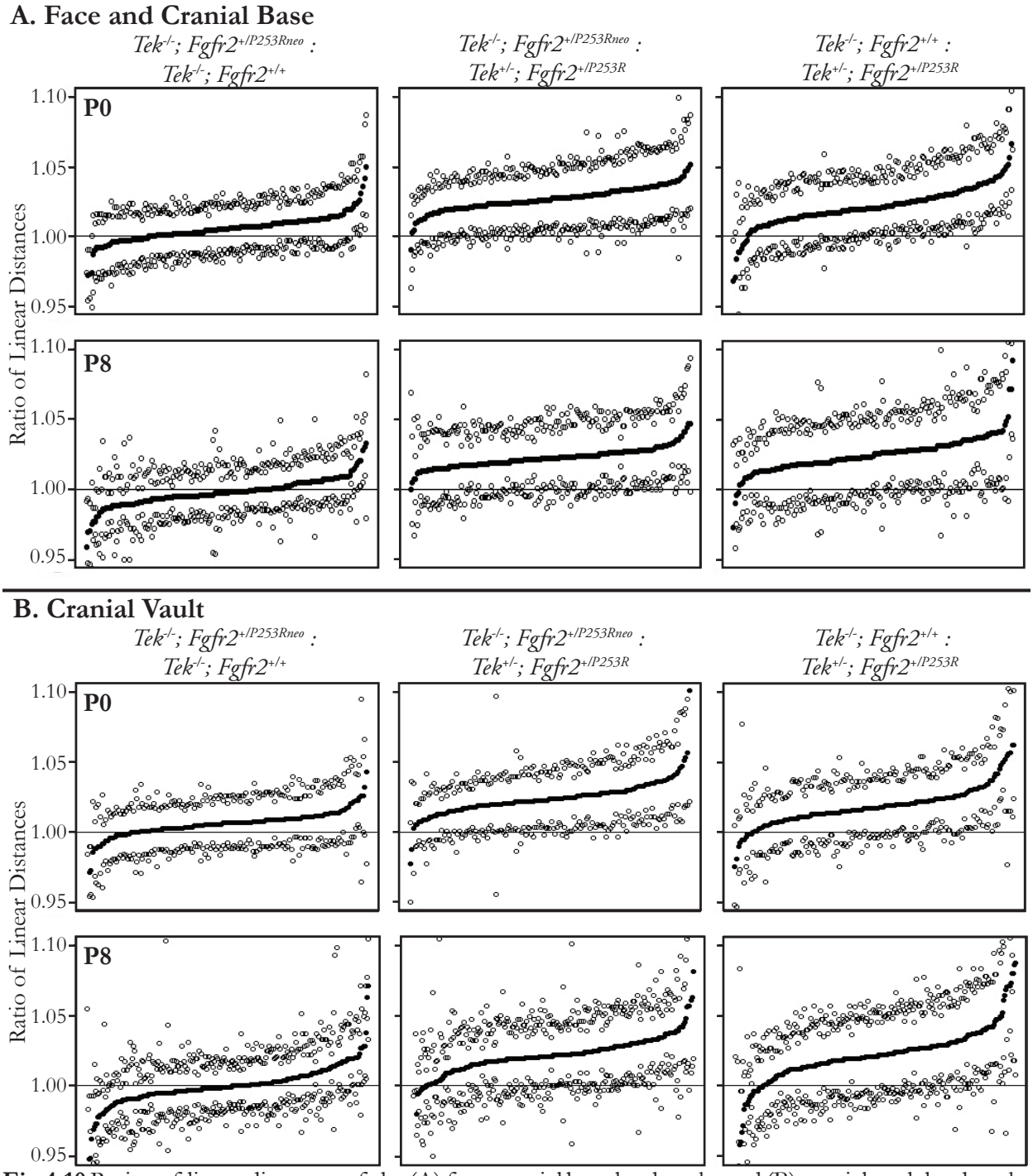

Fig 4.10 Ratios of linear distances of the (A) face-cranial base landmarks and (B) cranial vault landmarks, sorted by estimated ratio (filled circle) with 90% confidence intervals (open circles). Separate EDMA Form tests were completed for each pair of the three genotypes at P0 and P8. Note that the ratios of the two control genotypes (left) are centered around one, suggesting little differences in linear distances between the genotypes. However, the other two comparisons (center and right) show ratios drifting towards higher values, suggesting that linear distances of *Tek*$^{+/-}$*; Fgfr2*$^{+/P253R}$ (the denominator) tend to be smaller than both of the control genotypes at P0 and P8, often significantly so.

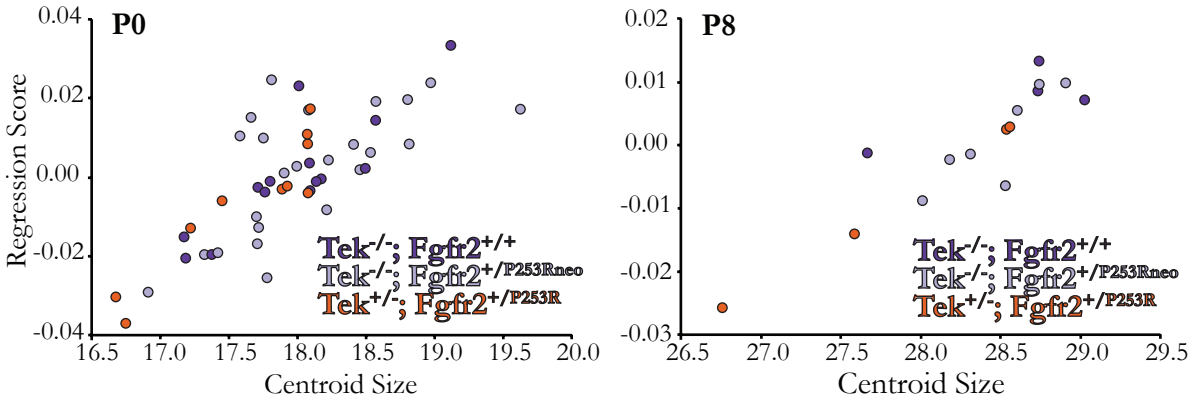

Fig 4.11 Plots of the centroid size and a regression summary score representing the landmark based skull shape accounted for by centroid size for specimens of all genotypes at P0 (left) and P8 (right). The relationship between regression score and centroid size is similar for all three genotypes, but *Tek*$^{+/-}$*; Fgfr2*$^{+/P253R}$ specimens tend to be found on the left side of both plots. This suggests that the relationship between size and shape is similar for all genotypes, but that the skulls of *Tek*$^{+/-}$*; Fgfr2*$^{+/P253R}$ mice display a smaller linear scale.

significant. Similarly, the mean volumes of each individual bone are similar across genotypes at P0, but trend lower for *Tek*$^{+/-}$*; Fgfr2*$^{+/P253R}$ mice for most bones at P8 (Fig 4.12). P8 LatO volume is significantly lower in *Tek*$^{+/-}$*; Fgfr2*$^{+/P253R}$ than in *Tek*$^{-/-}$*; Fgfr2*$^{+/P253Rneo}$, before correction for multiple testing. However, no other bone volumes are significantly different across pair-wise genotype comparisons, even though genotype differences for other bones, including PetT and SquO, appear subjectively more extreme at P8.

Functional multivariate regressions did not indicate that genotype is a significant factor in influencing relative bone density across ages or at each age individually, except for a significant difference between the two control genotypes for Par at P8. This suggests that any differences in relative bone mineral density, a proxy for bone maturation, between the *Tek*$^{+/-}$*; Fgfr2*$^{+/P253R}$ mice and controls are no more significant than the variation noted between the two control genotypes.

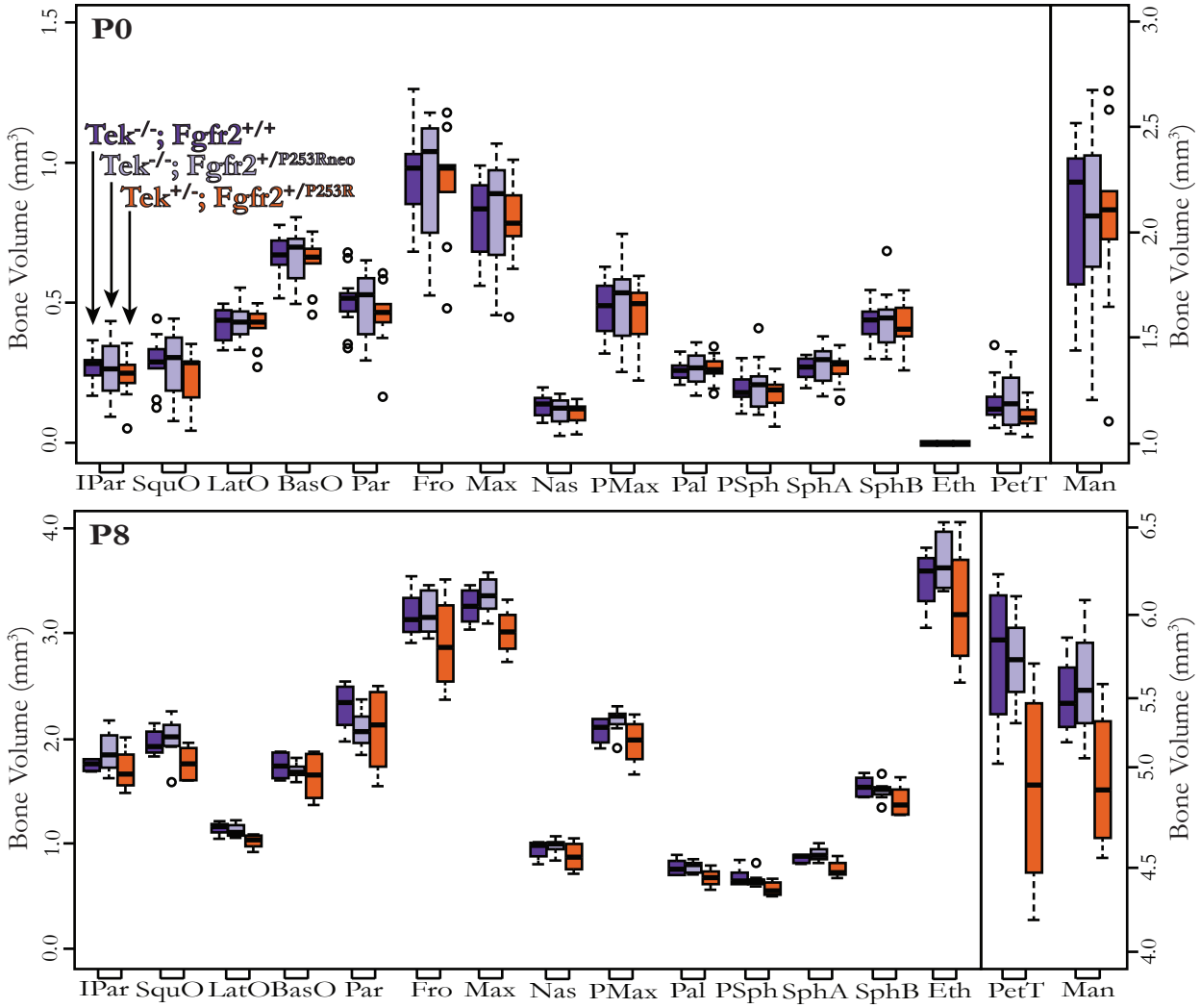

Fig 4.12 Boxplots of bone volumes by age, comparing the bone volume distributions for each bone between the three genotypes (Dark Blue: Tek$^{-/-}$; Fgfr2$^{+/+}$, Light Blue: Tek$^{-/-}$; Fgfr2$^{+/P253Rneo}$, Orange: Tek$^{+/-}$; Fgfr2$^{+/P253R}$). Dots represent outlier values that are more than 1.5 times the interquartile range from the box. The values for mandible (Man) and Petrous Temporal (PetT) may be at a different scale than the other bones within an age.

DISCUSSION

Normal Bone Growth

The mean "normal" standardized density curves for cranial bones at P0 and P8 reveal that most bones approach similar relative density levels by P8. The mean bone curves of P0 control mice are similar in nature to those measured from controls of *Fgfr2*$^{+/P253R}$ mice (Chapter 2), but display slightly higher relative density (Fig 4.8). This suggests that the early prenatal bone maturation of the

controls in this study may be ahead of the controls of *Fgfr2*$^{+/P253R}$ mice, but that both share similar patterns of bone maturation. The relative volumes of individual skull bones are similar for P0 mice in this and the previous study (Chapter 2) as well, suggesting that our measurements of volume and density serve to accurately quantify normal developmental patterns.

The three previously described groups that defined prenatal bone maturation (Chapter 2) do not serve to distinguish bones during the first week of postnatal bone maturation. While strong differences in relative bone density exist between bones at P0, these differences are reduced by P8; even for bones which display quite low density (e.g. Nas) or no bone (Eth) at birth. Data from several intermediate postnatal days are required to test the hypothesis that PetT and Eth share early ossification bone maturation patterns with other endochondral bones, as previously hypothesized (Chapter 2). But it is certain that any differences noted between the initial ossification of intramembranous and endochondral bones during the prenatal period are not evident by P8. This supports the previous hypothesis (Chapter 2) that bones with relatively low density at birth (mostly intramembranous bones) catch up to the relative density of higher density bones (most of the endochondral bones) during the early prenatal period.

Genotype Effect

Landmark based morphometric analysis, as well as volume and relative density analyses were completed on HRCT images of the heads of these mice in order to quantify any differences in skull bone morphology between the genotypes. Landmark based comparisons suggest that *Tek*$^{+/-}$*; Fgfr2*$^{+/P253R}$ mouse skulls are reduced in linear scale at P0 and P8. However, these mice lack the midfacial hypoplasia, coronal craniosynostosis, and rounded vault form of the *Fgfr2*$^{+/P253R}$ Apert syndrome mice (Figs 4.4-4.5). Given that cranial scale is reduced by P0, it is surprising that measures of bone volume are so similar between *Tek*$^{+/-}$*; Fgfr2*$^{+/P253R}$ mice and controls at birth. However, by P8, bone

volumes trend lower for *Tek*$^{+/-}$*; Fgfr2*$^{+/P253R}$ mice. Functional multivariate regressions did not indicate any significant differences in relative bone density between the genotypes at P0 or P8. However, the mean relative density curves for *Tek*$^{+/-}$*; Fgfr2*$^{+/P253R}$ mice at P8 (but not at P0) appear to represent a slightly lower density (data not shown), although the trend is not as obvious as with bone volumes. A larger sample size at P8 might reveal significant differences in volume and relative density between the genotypes.

Given the lack of gross dysmorphology noted in any of the specimens, our landmark based analysis could easily be interpreted as evidence for developmental delay of *Tek*$^{+/-}$*; Fgfr2*$^{+/P253R}$ mice along the same developmental growth trajectory as the control genotypes. However, only the landmark defined linear scale is reduced at P0, while bones contain similar amounts of similarly dense ossified material. This suggests that the endothelial expression of the P253R mutation modifies the distribution of osteoblast activity by P0, but not the number of or activity levels of those osteoblasts. We expect thicker skull bones with shorter linear extent in *Tek*$^{+/-}$*; Fgfr2*$^{+/P253R}$ mice at P0. By P8, the reduced linear scale of bones occurs alongside subjectively lower bone volumes distributions. During postnatal bone growth, the endothelial expression of the P253R mutation continues to influence the expansion of bone outward, but also begins to influence the amount of bone material produced. This suggests that the distribution of osteoblast activity and the number of osteoblasts may both be modified by P8. Further research beyond the bounds of this study is required to test these hypotheses of cellular distribution and activity.

Osteogenesis Regulated by Angiogenesis

The conditional expression of the P253R *Fgfr2* mutation within endothelial cells influences the growth and development of the craniofacial skeleton. Unlike the conditional expression of another Apert syndrome associated mutation within mesoderm derived and neural crest derived tissues

(Holmes and Basilico, 2012), the *Tek*$^{+/-}$; *Fgfr2*$^{+/P253R}$ mice do not display any of the visually obvious dysmorphology associated with Apert syndrome, including craniosynostosis and midfacial hypoplasia. However, they do display a reduction in linear scale at birth followed by reduced bone volume by P8, suggesting that the endothelial expression of the P253R mutation contributes to the abnormal dimensions noted in *Fgfr2*$^{+/P253R}$ mice (Wang et al., 2010; Martínez-Abadías et al., 2010; Chapter 2). This supports the idea that dysmorphology associated with Apert syndrome arises from the direct pleiotropic influence of the P253R mutation on multiple tissue types within the head (Aldridge et al., 2010; Percival and Richtsmeier, 2011; Martínez-Abadías et al., 2013). In this case, expression of this mutation within endothelial cells may regulate skeletal growth and development of skull bones.

While the critical importance of angiogenesis to the process of osteogenesis has been well documented in the postcranial skeleton and can be assumed to exist during cranial bone ossification (Chapter 1), the regulatory mechanisms through which angiogenesis might influence bone growth and development are not well studied. A study of the IBE endothelial cell line, derived from murine brain capillaries, suggests that FGFR2 expression in endothelial cells regulates endothelial cell motility, an important aspect of the process of angiogenesis. However, other angiogenic responses including endothelial cell proliferation and capillary tube formation do not appear to be influenced by FGFR2 signaling (Nakamura et al., 2001). While it is possible that the results of this cell-culture study are not generalizable to the process of angiogenesis across developing tissues *in vivo* (Javerzat et al., 2002), there is little evidence to suggest that endothelial FGFR2 expression does not play a similar role during angiogenesis associated with cranial bone osteogenesis.

If FGFR2 expression in endothelial cells only influences angiogenesis via dysregulation of endothelial cell motility; an *Fgfr2* mutation, like the P253R mutation, might only serve to modulate the speed of new capillary outgrowth from existing vasculature during angiogenesis. Given the importance

of the proximity of capillaries to osteoblasts during osteogenesis (Chapter 1), we hypothesize that a reduction in the motility of the endothelial cells within *Tek*$^{+/-}$; *Fgfr2*$^{+/P253R}$ mice leads to a reduction in the spatial extent of active osteoblasts within developing bones and secondarily, to reduced linear size skull bones. It is not clear whether a reduction in motility based on the P253R mutation might lead to a capillary network with shorter capillary segments between branch points, fewer capillary branches, or some other modified network structure. In any case, a reduction in the region over which the capillaries associated with ossifying bones would likely limit the linear range over which osteoblasts could successfully differentiate and produce bone. Logically, this could lead to a situation where the quality and speed of bone forming activity is unchanged, except for being limited to a smaller spatial extent. If this hypothesis is correct, we expect the capillary network associated with developing bones in our *Tek*$^{+/-}$; *Fgfr2*$^{+/P253R}$ mice to be reduced in spatial extent starting during the earliest phases of prenatal cranial ossification, followed by a similar reduction in spatial extent of osteoblast activity and mineralized tissue.

Given that signaling between tissues may play a major role in regulating cranial bone development (Percival and Richtsmeier, 2011), it is possible that the conditional expression of the P253R mutation in endothelial cells directly influences bone cells or their precursors, rather than secondarily influencing them via the dysregulation of angiogenesis. It is also possible that the endothelial expression of this mutation might influence the growth of the cranial bones via abnormal development of other vascular features across the developing specimen, perhaps because of something like reduced blood flow. Future studies on the covariation between capillary network properties and bone mineralization will be required to determine the regulatory basis of the subtle changes in cranial bone growth and development noted in our *Tek*$^{+/-}$; *Fgfr2*$^{+/P253R}$ mice.

Summary

The conditional expression of the P253R mutation within endothelial cells appears to contribute to the dysmorphogenesis associated with the *Fgfr2*$^{+/P253R}$ Apert syndrome mouse model and perhaps in producing dysmorphology of humans with Apert syndrome. This includes a reduction in linear scale of the skull at birth and a potential reduction in craniofacial bone volume later on, but not midfacial hypoplasia, premature suture fusion, or strong shape dysmorphology. Although further work is neccessary to determine the particular mechanism, this study provides evidence that dysregulation of angiogenesis may indirectly lead to craniofacial skeletal dysmorphology.

CHAPTER 5:
CONCLUSION

Although the relationship is poorly studied, angiogenesis is likely to be critical during the skeletonization of both endochondral and intramembranous craniofacial bones. The growth of blood vessels within avascular cartilage models or mesenchymal condensations is likely to provide differentiating osteoblasts with access to oxygen required for increased cellular activity, phosphate and calcium ions for bone mineralization, and a variety of other factors. Additionally, encroaching endothelial cells are one of several cell types that are part of the regulatory network associated with osteogenesis and bone remodeling. While the work of other researchers has begun to provide details about the process of intramembranous bone skeletogenesis and an outline of how angiogenesis is associated with craniofacial skeletogenesis, significant future work is required to determine the exact regulatory relationship between these developmental processes. Similar genetic factors might be associated with angiogenesis during initial craniofacial and postcranial long bone mineralization, but the regulatory basis for the expression of these factors is likely to be different; particularly within intramembranously formed calvarial bones where a thin layer of migrating mesenchymal precursor cells are unlikely to exhibit the strong hypoxia found in dense populations of epiphyseal chondrocytes.

Given the importance of angiogenesis in the formation of early craniofacial bones, we hypothesized that angiogenesis dysregulation could indirectly lead to craniofacial skeletal dysmorphology during development and in adult life. Within the palimpsest model (Gregory, 1947; Hallgrímsson et al., 2009), the process of angiogenesis can be conceptualized as one of many developmental determinants of variation in the complex trait of the craniofacial skeleton. Therefore, variation

in angiogenesis regulation could serve as the basis for some of the variation in craniofacial traits that define the primate clade and differentiate hominid species. In order to investigate the potential influence of angiogenesis on craniofacial skeletal variation, we attempted to determine whether angiogenesis dysregulation was associated with any of the dysmorphology noted in an Apert mouse model expressing the P253R mutation of *Fgfr2* (Wang et al., 2010), a gene associated with regulation of both osteogenesis and angiogenesis. Although the research described in this dissertation may not have pinpointed the cellular mechanisms underlying the connection between these two developmental processes, it has provided evidence that the process of angiogenesis is modified by this mutation and that angiogenesis dysregulation can lead to modifications in craniofacial skeletal phenotype.

The refinement of our previously published method of bone volume and relative density measurement from high resolution computed tomography images allows for the easy quantification of aspects of the craniofacial skeletal phenotype that complement more commonly used landmark based morphometric methods and allow more sophisticated hypotheses about regulatory influences on bone cell activity to be made. "Normal" patterns of bone maturation were defined by spline curves based on relative density histograms and provided evidence of a difference in the pattern of prenatal endochondral and intramembranous bone maturation, although all bones may display similar relative densities postnatally. Functional regression analysis of these curves suggested that the *Fgfr2*$^{+/P253R}$ mice display reduced relative density for many craniofacial bones across prenatal and perinatal bone maturation in a manner reminiscent of a slightly earlier developmental age. The combination of landmark based, volume, and relative density analyses led to several hypotheses about how modifications to cellular proliferation and differentiation might underlie the craniofacial dysmorphology associated with Apert syndrome. These hypotheses will need to be tested with future work on cellular activity at sites of skeletogenesis across the head.

In an attempt to directly quantify changes to the microvascular network associated with the developing frontal bone and surrounding tissues in *Fgfr2*$^{+/P253R}$ mice, images of vasculature and soft tissue layers were produced using a hybrid optical coherence tomography (OCT)/ photoacoustic microscopy (PAM) system. Image segmentation and analysis illustrated the types of large vessels that are associated with tissues surrounding the developing frontal bone, as well as the significant variation in these embryonic vessels. Preliminary analysis of total vessel lengths and vessel diameter distributions suggests that there may be a reduction in total blood vessel length within mice expressing the P253R mutation. However, because of the subadequate resolution of the OCT images and low PAM signal from dead vascular tissues, definitive identification of the mineralizing frontal bone and of the microvasculature directly associated with its vascular invasion was not possible.

Breeding a strain of mice that conditionally expressed the P253R mutation of *Fgfr2* in vascular endothelial cells (*Tek*$^{+/-}$; *Fgfr2*$^{+/P253R}$) provided another way to address the potential influence of angiogenesis dysregulation on the craniofacial complex. Phenotypic analysis indicated that *Tek*$^{+/-}$; *Fgfr2*$^{+/P253R}$ mice were reduced in overall linear scale of the skull at birth, but that their bones displayed similar volume and relative density; suggesting a reduction in the linear spatial extent of equivalent numbers of active osteoblasts. By P8, linear scale and bone volume both appear to be reduced, suggesting more severe skeletal dysmorphology later in development. Based on this analysis and a few previous studies on the endothelial expression of FGFR, we hypothesized that endothelial expression of the *Fgfr2* P253R mutation reduces the migratory capacity of endothelial cells during angiogenesis, leading to a reduced volume of mesenchymal cells across which active osteoblasts can produce bone, resulting in a skull of reduced size and normal shape.

Given our limited success in resolving microvasculature associated with angiogenesis during craniofacial skeletogenesis from OCT/PAM images, another method is required to quantify the

craniofacial vascular network structure in mice displaying dysregulated angiogenesis and "normal" controls. These measures will allow for a direct test of our most significant hypotheses about the interaction of angiogenesis and craniofacial skeletogenesis. Fluorescent based optical imaging methods may be the current best way to produce the necessary 3D images of cranial vascular networks and associated bone. Although continued study on the influence of the *Fgfr2* P253R mutation will be interesting, the use of an animal model that misexpresses a gene known to regulate more of the cellular activities of endothelial cells may produce more obvious modifications to angiogenesis and associated skeletogenesis. Finally, the methods of craniofacial skeletal phenotyping developed in association with the work contained in this dissertation might be used to more completely quantify variation during normal development across the skull and to provide specific hypotheses about the cellular bases of dysmorphology associated with known mutations. Although these methods can provide important exploratory and comparative phenotypic quantification of vasculature and bones across the skull, further histological or molecular work will be required to test resulting hypotheses about modifications in cellular activity.

The results of the work contained in this dissertation demonstrate the importance of studies that examine the relationships between multiple tissues, which can serve as the basis of variation in complex phenotypes like the craniofacial complex. Although this work only examines the relationship between two tissues, a combination of similar studies on the relationship between other tissues across developmental time is required to understand the basis on phenotypic variation noted in modern populations and across the evolutionary record. Given the fact that craniofacial features considered diagnostic for determining hominid species tend to appear by birth (Chapter 1), anthropologists must explore the embryonic bases of phenotypic variation in order to develop a more sophisticated understanding of phenotypic shifts across our evolutionary history. Hopefully we will have the

opportunity to expand on the work contained in this dissertation and it will add to an increasing understanding of how modifications to developmental systems serve as the basis of evolutionary changes.

REFERENCES

Abzhanov A, Rodda SJ, McMahon AP, and Tabin CJ. 2007. Regulation of skeletogenic differentiation in cranial dermal bone. Development 134:3133–3144.

Ahrens PB, Solursh M, and Reiter RS. 1977. Stage-related capacity for limb chondrogenesis in cell culture. Developmental biology 60:69–82.

Aiello L, and Dean C. 2002. An introduction to human evolutionary anatomy. London: Academic Press.

Al-Aql ZS, Alagl AS, Graves DT, Gerstenfeld LC, and Einhorn TA. 2008. Molecular mechanisms controlling bone formation during fracture healing and distraction osteogenesis. Journal of Dental Research 87:107–118.

Aldridge K, Hill CA, Austin JR, Percival C, Martinez-Abadias N, Neuberger T, Wang Y, Jabs EW, and Richtsmeier JT. 2010. Brain phenotypes in two FGFR2 mouse models for Apert syndrome. Developmental Dynamics 239:987–997.

Amizuka N, Hasegawa T, Oda K, Luiz de Freitas P, Hoshi K, Li M, and Ozawa H. 2012. Histology of epiphyseal cartilage calcification and endochondral ossification. Front Biosci 4:2085–2100.

Anderson J, Burns HD, Enriquez-Harris P, Wilkie AOM, and Heath JK. 1998. Apert syndrome mutations in fibroblast growth factor receptor 2 exhibit increased affinity for FGF ligand. Human Molecular Genetics 7:1475–1483.

Aronson J, Good B, Stewart C, Harrison B, and Harp J. 1990. Preliminary studies of mineralization during distraction osteogenesis. Clinical orthopaedics and related research 250:43–49.

Aronson J. 1994. Temporal and spatial increases in blood flow during distraction osteogenesis. Clinical orthopaedics and related research 301:124–131.

Athreya S. 2009. A comparative study of frontal bone morphology among Pleistocene hominin fossil groups. Journal of Human Evolution 57:786–804.

Aubin JE. 2008. Mesenchymal Stem Cells and Osteoblast Differentiation. In: Bilezikian JP, Raisz LG, Martin TJ, editors. Principles of Bone Biology. Vol. 1. 3rd ed. Academic Press. p 85–107.

Auguste P, Gürsel DB, Lemière S, Reimers D, Cuevas P, Carceller F, Di Santo JP, and Bikfalvi A. 2001. Inhibition of fibroblast growth factor/fibroblast growth factor receptor activity in glioma cells impedes tumor growth by both angiogenesis-dependent and-independent mechanisms. Cancer Research 61:1717–1726.

Baron J, Klein K, Yanovski J, Novosad J, Bacher J, Bolander M, and Cutler Jr G. 1994. Induction of growth plate cartilage ossification by basic fibroblast growth factor. Endocrinology 135:2790–2793.

Barton JK, Tang S, Lim R, and Tromberg BJ. 2007. Simultaneous optical coherence and multiphoton microscopy of skin-equivalent tissue models. Proc. of SPIE-OSA Biomedical Optics 6627.

Bates CM. 2007. Role of fibroblast growth factor receptor signaling in kidney development. Pediatric Nephrology 22:343–349.

Beals KL, Smith CL, and Dodd SM. 1984. Brain size, cranial morphology, climate, and time machines. Current Anthropology 25:301–330.

Beamer WG, Donahue LR, Rosen CJ, and Baylink DJ. 1996. Genetic variability in adult bone density among inbred strains of mice. Bone 18:397–403.

Beamer WG, Shultz KL, Donahue LR, Churchill GA, Sen S, Wergedal JR, Baylink DJ, and Rosen CJ. 2001. Quantitative trait loci for femoral and lumbar vertebral bone mineral density in C57BL/6J and C3H/HeJ inbred strains of mice. Journal of Bone and Mineral Research 16:1195–1206.

Bloom W, and Fawcett DW. 1994. A textbook of hisology. New York, NY: Chapman & Hall.

Boehm B, Rautschka M, Quintana L, Raspopovic J, Jan Ž, and Sharpe J. 2011. A landmark-free morphometric staging system for the mouse limb bud. Development 138:1227–1234.

Bolander ME. 1992. Regulation of fracture repair by growth factors. Proceedings of the Society for Experimental Biology and Medicine 200:165–170.

Bookstein FL. 1996. Biometrics, biomathematics and the morphometric synthesis. Bulletin of Mathematical Biology 58:313–365.
Boppart SA, Brezinski ME, Bouma BE, Tearney GJ, and Fujimoto JG. 1996. Investigation of developing embryonic morphology using optical coherence tomography. Developmental Biology 177:54–63.
Bouletreau PJ, Warren SM, Spector JA, Peled ZM, Gerrets RP, Greenwald JA, and Longaker MT. 2002. Hypoxia and VEGF up-regulate BMP-2 mRNA and protein expression in microvascular endothelial cells: implications for fracture healing. Plastic and Reconstructive Surgery 109:2384–2397.
Boyde A, and Shapiro IM. 1987. Morphological observations concerning the pattern of mineralization of the normal and the rachitic chick growth cartilage. Anatomy and embryology 175:457–466.
Brandi ML, and Collin-Osdoby P. 2006. Vascular biology and the skeleton. Journal of Bone and Mineral Research 21:183–192.
Bronner ME. 2012. Formation and migration of neural crest cells in the vertebrate embryo. Histochemistry and Cell Biology:1–8.
Brookes M, and Revell WJ. 1998. Blood Supply of Bone. London: Springer.
Caplan AI, Syftestad G, and Osdoby P. 1983. The development of embryonic bone and cartilage in tissue culture. Clinical orthopaedics and related research 174:243 – 263.
Carmody RN, Weintraub GS, and Wrangham RW. 2011. Energetic consequences of thermal and nonthermal food processing. Proceedings of the National Academy of Sciences 108:19199–19203.
Carroll SB, Grenier JK, and Weatherbee SD. 2001. From DNA to diversity. London, UK: Blackwell Science.
Chen L, and Deng CX. 2005. Roles of FGF signaling in skeletal development and human genetic diseases. Front Biosci 10:961–76.
Chen L, Li D, Li C, Engel A, and Deng CX. 2003. A Ser250Trp substitution in mouse fibroblast growth factor receptor 2 (Fgfr2) results in craniosynostosis. Bone 33:169–178.
Cheverud JM. 1995. Morphological integration in the saddle-back tamarin (*Saguinus fuscicollis*) cranium. The American Naturalist 145:63–89.
Cheverud JM. 1996. Quantitative genetic analysis of cranial morphology in the cotton-top (*Saguinus oedipus*) and saddle-back (*S. fuscicollis*) tamarins. Journal of Evolutionary Biology 9:5–42.
Chimal-Monroy J, and Diaz de Leon L. 1999. Expression of N-cadherin, N-CAM, fibronectin and tenascin is stimulated by TGF-beta1, beta2, beta3 and beta5 during the formation of precartilage condensations. Int J Dev Biol 43:59–67.
Choi IH, Ahn JH, Chung CY, and Cho TJ. 2000. Vascular proliferation and blood supply during distraction osteogenesis: a scanning electron microscopic observation. Journal of Orthopaedic Research 18:698–705.
Choi IH, Chung CY, Cho TJ, and Yoo WJ. 2002. Angiogenesis and mineralization during distraction osteogenesis. Journal of Korean Medical Science 17:435–447.
Cobb SN, and O'Higgins P. 2004. Hominins do not share a common postnatal facial ontogenetic shape trajectory. Journal of Experimental Zoology Part B: Molecular and Developmental Evolution 302:302–321.
Cohen Jr MM, and Kreiborg S. 1996. Suture formation, premature sutural fusion, and suture default zones in Apert syndrome. American Journal of Medical Genetics Part A 62:339–344.
Cohen Jr MM, and Maclean RE. 2000. Craniosynostosis: diagnosis, evaluation and management 2nd edition. New York: Oxford University Press.
Collin-Osdoby P. 1994. Role of vascular endothelial cells in bone biology. Journal of cellular biochemistry 55:304–309.

Colnot C, Lu C, Hu D, and Helms JA. 2004. Distinguishing the contributions of the perichondrium, cartilage, and vascular endothelium to skeletal development. Developmental Biology 269:55–69.

Cordero DR, Brugmann S, Chu Y, Bajpai R, Jame M, and Helms JA. 2011. Cranial neural crest cells on the move: Their roles in craniofacial development. American Journal of Medical Genetics Part A 155:270–279.

Corner BD, Lele S, and Richtsmeier JT. 1992. Measuring precision of three-dimensional landmark data. Journal of Quantitative Anthropology 3:347–359.

Costello F, Coupland S, Hodge W, Lorello GR, Koroluk J, Pan YI, Freedman MS, Zackon DH, and Kardon RH. 2006. Quantifying axonal loss after optic neuritis with optical coherence tomography. Annals of Neurology 59:963–969.

Cotton LM, O'Bryan MK, and Hinton BT. 2008. Cellular signaling by fibroblast growth factors (FGFs) and their receptors (FGFRs) in male reproduction. Endocrine reviews 29:193–216.

Dai J, and Rabie A. 2007. VEGF: an essential mediator of both angiogenesis and endochondral ossification. Journal of dental research 86:937–950.

De Spiegelaere W, Cornillie P, Casteleyn C, Burvenich C, and Van Den Broeck W. 2010. Detection of hypoxia inducible factors and angiogenic growth factors during foetal endochondral and intramembranous ossification. Anatomia, histologia, embryologia 39:376–384.

Dean C, Leakey MG, Reid D, Schrenk F, Schwartz GT, Stringer C, and Walker A. 2001. Growth processes in teeth distinguish modern humans from *Homo erectus* and earlier hominins. Nature 414:628–631.

Deckelbaum RA, Holmes G, Zhao Z, Tong C, Basilico C, and Loomis CA. 2012. Regulation of cranial morphogenesis and cell fate at the neural crest-mesoderm boundary by engrailed 1. Development 139:1346–1358.

Delloye C, Delefortrie G, Coutelier L, and Vincent A. 1990. Bone regenerate formation in cortical bone during distraction lengthening: an experimental study. Clinical orthopaedics and related research 250:34–42.

Depew MJ, Tucker AS, and Sharpe PT. 2002. Craniofacial development. In: Rossant J, Tam PPL, editors. Mouse development, patterning, morphogenesis, and organogenesis. San Diego: Academic Press. p 421–498.

Dietrich EM, and Antoniades K. 2012. Bone-vasculature interactions in the mandible: Is bone an angiogenic tissue? Medical Hypotheses.

Dorr A, Sled J, and Kabani N. 2007. Three-dimensional cerebral vasculature of the CBA mouse brain: a magnetic resonance imaging and micro computed tomography study. NeuroImage 35:1409–1423.

Dougherty R, and Kunzelmann KH. 2007. Computing local thickness of 3D structures with ImageJ. Microscopy and Microanalysis 13:1678–1679.

Drake AG, and Klingenberg CP. 2008. The pace of morphological change: historical transformation of skull shape in St Bernard dogs. Proceedings of the Royal Society B: Biological Sciences 275:71–76.

Drushel RF, Pechak DG, and Caplan AI. 1985. The anatomy, ultrastructure and fluid dynamics of the developing vasculature of the embryonic chick wing bud. Cell Differentiation 16:13–28.

Du X, Weng T, Sun Q, Su N, Chen Z, Qi H, Jin M, Yin L, He Q, and Chen L. 2010. Dynamic morphological changes in the skulls of mice mimicking human Apert syndrome resulting from gain-of-function mutation of FGFR2 (P253R). Journal of Anatomy 217:97–105.

Eames BF, and Helms JA. 2004. Conserved molecular program regulating cranial and appendicular skeletogenesis. Developmental Dynamics 231:4–13.

Eames BF, and Schneider RA. 2008. The genesis of cartilage size and shape during development and evolution. Development 135:3947–3958.

Eames BF, De La Fuente L, and Helms JA. 2003. Molecular ontogeny of the skeleton. Birth Defects Research Part A: Clinical and Molecular Teratology 69:93–101.
Eghbali-Fatourechi GZ, Lamsam J, Fraser D, Nagel D, Riggs BL, and Khosla S. 2005. Circulating osteoblast-lineage cells in humans. New England Journal of Medicine 352:1959–1966.
Eghbali-Fatourechi GZ, Mödder UIL, Charatcharoenwitthaya N, Sanyal A, Undale AH, Clowes JA, Tarara JE, and Khosla S. 2007. Characterization of circulating osteoblast lineage cells in humans. Bone 40:1370–1377.
Enlow D. 2000. Normal Craniofacial Growth. In: Cohen Jr MM, MacLean RE, editors. Craniosynostosis: Diagnosis, Evaluation, and Management. Second. New York: Oxford University Press. p 35–47.
Eriksen EF, Eghbali-Fatourechi GZ, and Khosla S. 2007. Remodeling and vascular spaces in bone. J Bone Miner Res 22:1–6.
Eshkar-Oren I, Viukov SV, Salameh S, Krief S, Akiyama H, Gerber HP, Ferrara N, Zelzer E, and others. 2009. The forming limb skeleton serves as a signaling center for limb vasculature patterning via regulation of Vegf. Development 136:1263–1272.
Eswarakumar VP, Monsonego-Ornan E, Pines M, Antonopoulou I, Morriss-Kay GM, and Lonai P. 2002. The IIIc alternative of Fgfr2 is a positive regulator of bone formation. Development 129:3783–3793.
Falk D. 1992. Evolution of the brain and cognition in hominids. New York: American Museum of Natural History.
Fang TD, Salim A, Xia W, Nacamuli RP, Guccione S, Song HJM, Carano RA, Filvaroff EH, Bednarski MD, Giaccia AJ, et al. 2005. Angiogenesis is required for successful bone induction during distraction osteogenesis. Journal of Bone and Mineral Research 20:1114–1124.
Fleagle JG, Gilbert CC, and Baden AL. 2010. Primate cranial diversity. American Journal of Physical Anthropology 142:565–578.
Fujikawa Y, Quinn J, Sabokbar A, McGee J, and Athanasou N. 1996. The human osteoclast precursor circulates in the monocyte fraction. Endocrinology 137:4058–4060.
Fukumoto S. 2008. Physiological regulation and disorders of phosphate metabolism-pivotal role of fibroblast growth factor 23. Internal Medicine 47:337–343.
Gerber HP, Vu TH, Ryan AM, Kowalski J, Werb Z, Ferrara N, and others. 1999. VEGF couples hypertrophic cartilage remodeling, ossification and angiogenesis during endochondral bone formation. Nature Medicine 5:623–628.
Gould SJ. 1977. Ontogeny and phylogeny. Cambridge, MA: Belknap press.
Gregory WK. 1947. The monotremes and the palimpsest theory. Bulletin of the American Museum of Natural History 88:1–52.
Hall B. 1992. Cell-cell interactions in craniofacial growth and development. In: Davidovitch Z, editor. The Biological Mechanisms of Tooth Movement and Craniofacial Adaptation. Birmingham, AL: EBSCO Media. p 261–267.
Hall BK, and Miyake T. 1992. The membranous skeleton: the role of cell condensations in vertebrate skeletogenesis. Anatomy and Embryology 186:107–124.
Hall BK, and Miyake T. 1995. Divide, accumulate, differentiate: cell condensation in skeletal development revisited. International Journal of Developmental Biology 39:881–894.
Hall BK, and Miyake T. 2000. All for one and one for all: condensations and the initiation of skeletal development. Bioessays 22:138–147.
Hall BK. 1988. The embryonic development of bone. American Scientist 76:174–181.
Hall BK. 1999. Evolutionary developmental biology. Dodrecht, The Netharlands: Kluwer Academic Publishers.
Hall BK. 2003. Evo-Devo: evolutionary developmental mechanisms. International Journal of Developmental Biology 47:491–496.

Hall BK. 2005. Bones and Cartilage: Developmental and Evolutionary Skeletal Biology. Academic Press.

Hallgrímsson B, and Lieberman DE. 2008. Mouse models and the evolutionary developmental biology of the skull. Integrative and Comparative Biology 48:373–384.

Hallgrímsson B, Jamniczky H, Young NM, Rolian C, Parsons TE, Boughner JC, and Marcucio RS. 2009. Deciphering the Palimpsest: Studying the Relationship between Morphological Integration and Phenotypic Covariation. Evolutionary Biology 36:355–376.

Han C, Chu C, Adachi N, Usas A, Fu F, Huard J, and Pan Y. 2003. Analysis of rabbit articular cartilage repair after chondrocyte implantation using optical coherence tomography. Osteoarthritis and Cartilage 11:111–121.

Hansen ES. 1993. Microvascularization, osteogenesis, and myelopoiesis in normal and pathological conditions. In: Schoutens A, Arlet J, Gardeniers JWM, Hughes SPF, editors. Bone Circulation and Vascularization in Normal and Pathological Conditions. NATO ASI Series A: Life Sciences. New York: Plenum Press. p 29–42.

Heaney RP. 2008. Calcium. In: Principles of Bone Biology. Vol. 2. 3rd ed. San Diego: Academic Press. p 1697–1710.

Hee MR, Izatt JA, Swanson EA, Huang D, Schuman JS, Lin CP, Puliafito CA, and Fujimoto JG. 1995. Optical coherence tomography of the human retina. Archives of Ophthalmology 113:325–332.

Hill CA, Martínez-Abadías N, Motch SM, Austin JR, Wang Y, Jabs EW, Richtsmeier JT, and Aldridge K. 2013. Growth of the skull and brain differ postnatally in a mouse model for Apert syndrome. American Journal of Medical Genetics Part A.

Holloway JRL. 1969. Culture: a human domain. Current Anthropology 10:395–412.

Holmes G, and Basilico C. 2012. Mesodermal expression of Fgfr2S252W is necessary and sufficient to induce craniosynostosis in a mouse model of Apert syndrome. Developmental Biology 368:283–293.

Holmes G, Rothschild G, Roy UB, Deng CX, Mansukhani A, and Basilico C. 2009. Early onset of craniosynostosis in an Apert mouse model reveals critical features of this pathology. Developmental Biology 328:273–284.

Horton WA, and Lunstrum GP. 2002. Fibroblast growth factor receptor 3 mutations in achondroplasia and related forms of dwarfism. Reviews in Endocrine & Metabolic Disorders 3:381–385.

Hou J, Kan M, McKeehan K, McBride G, Adams P, and McKeehan WL. 1991. Fibroblast growth factor receptors from liver vary in three structural domains. Science 251:665–668.

Huang D, Swanson EA, Lin CP, Schuman JS, Stinson WG, Chang W, Hee MR, Flotte T, Gregory K, Puliafito CA, et al. 1991. Optical Coherence Tomography. Science 254:1178–1181.

Hunter WL, Arsenault AL, and Hodsman AB. 1991. Rearrangement of the metaphyseal vasculature of the rat growth plate in rickets and rachitic reversal: a model of vascular arrest and angiogenesis renewed. The Anatomical record 229:453–461.

Hurley M, Naski M, and Marie P. 2008. Fibroblast growth factor (FGF) and FGF receptor families in bone. In: Principles of bone biology. Vol. 2. 3rd ed. San Diego: Academic Press. p 1103–1132.

Igarashi M, Finch PW, and Aaronson SA. 1998. Characterization of recombinant human fibroblast growth factor (FGF)-10 reveals functional similarities with keratinocyte growth factor (FGF-7). Journal of Biological Chemistry 273:13230–13235.

Iseki S, Wilkie A, and Morriss-Kay G. 1999. Fgfr1 and Fgfr2 have distinct differentiation-and proliferation-related roles in the developing mouse skull vault. Development 126:5611–5620.

Iseki S, Wilkie A, Heath J, Ishimaru T, Eto K, and Morriss-Kay G. 1997. Fgfr2 and osteopontin domains in the developing skull vault are mutually exclusive and can be altered by locally applied FGF2. Development 124:3375–3384.

Isler K, Christopher Kirk E, Miller J, Albrecht GA, Gelvin BR, and Martin RD. 2008. Endocranial volumes of primate species: scaling analyses using a comprehensive and reliable data set. Journal of human evolution 55:967–978.

Jamniczky HA, and Hallgrímsson B. 2011. Modularity in the skull and cranial vasculature of laboratory mice: implications for the evolution of complex phenotypes. Evolution & Development 13:28–37.

Javerzat S, Auguste P, and Bikfalvi A. 2002. The role of fibroblast growth factors in vascular development. Trends in molecular medicine 8:483–489.

Jeffery N, and Spoor F. 2002. Brain size and the human cranial base: a prenatal perspective. American Journal of Physical Anthropology 118:324–340.

Jiang X, Iseki S, Maxson RE, Sucov HM, and Morriss-Kay GM. 2002. Tissue Origins and Interactions in the Mammalian Skull Vault. Developmental Biology 241:106–116.

Jourdeuil K, and Franz-Odendaal TA. 2012. Vasculogenesis and the Induction of Skeletogenic Condensations in the Avian Eye. The Anatomical Record: Advances in Integrative Anatomy and Evolutionary Biology 295:691–698.

Kallenbach K, and Frederiksen J. 2007. Optical coherence tomography in optic neuritis and multiple sclerosis: a review. European Journal of Neurology 14:841–849.

Kanczler J, and Oreffo R. 2008. Osteogenesis and angiogenesis: the potential for engineering bone. European Cells and Materials 15:100–114.

Kanda S, Landgren E, Ljungström M, and Claesson-Welsh L. 1996. Fibroblast growth factor receptor 1-induced differentiation of endothelial cell line established from tsA58 large T transgenic mice. Cell growth & differentiation 7:383–395.

Karaplis AC. 2008. Embryonic Development of Bone and Regulation of Intramembranous and Endochondral Bone Formation. In: Bilezikian JP, Raisz LG, Martin TJ, editors. Principles of Bone Biology. Vol. 1. 3rd ed. Academic Press. p 53–84.

Kasseck C, Kratz M, Torcasio A, Gerhardt NC, Van Lenthe GH, Gambichler T, Hoffmann K, Jones DB, and Hofmann MR. 2010. Comparison of optical coherence tomography, microcomputed tomography, and histology at a three-dimensionally imaged trabecular bone sample. Journal of Biomedical Optics 15:046019 1–6.

Kaufman MH. 1999. The Atlas of Mouse Development. London: Academic Press.

Kawaguchi H, Nakamura K, Tabata Y, Ikada Y, Aoyama I, Anzai J, Nakamura T, Hiyama Y, and Tamura M. 2001. Acceleration of fracture healing in nonhuman primates by fibroblast growth factor-2. Journal of Clinical Endocrinology & Metabolism 86:875–880.

Kawaguchi J, Wilson V, and Mee PJ. 2002. Visualization of whole-mount skeletal expression patterns of LacZ reporters using a tissue clearing protocol. Biotechniques 32:66–70.

Kay RF, Cartmill M, and Balow M. 1998. The hypoglossal canal and the origin of human vocal behavior. Proceedings of the National Academy of Sciences 95:5417–5419.

Keane PA, Patel PJ, Liakopoulos S, Heussen FM, Sadda SR, and Tufail A. 2012. Evaluation of Age-related Macular Degeneration With Optical Coherence Tomography. Survey of Ophthalmology 57:389–414.

Kisanuki YY, Hammer RE, Miyazaki J, Williams SC, Richardson JA, and Yanagisawa M. 2001. Tie2-Cre Transgenic Mice: A New Model for Endothelial Cell-Lineage Analysis< i> in Vivo</i>. Developmental biology 230:230–242.

Klingenberg CP. 2008. Morphological integration and developmental modularity. Annual review of ecology, evolution, and systematics 39:115–132.

Klingenberg CP. 2011. MorphoJ: an integrated software package for geometric morphometrics. Molecular Ecology Resources 11:353–357.

Komaki H, Tanaka T, Chazono M, and Kikuchi T. 2006. Repair of segmental bone defects in rabbit tibiae using a complex of beta-tricalcium phosphate, type I collagen, and fibroblast growth factor-2. Biomaterials 27:5118–5126.

Koyabu D, Maier W, and Sánchez-Villagra MR. 2012. Paleontological and developmental evidence resolve the homology and dual embryonic origin of a mammalian skull bone, the interparietal. Proceedings of the National Academy of Sciences 109:14075–14080.

Kronenberg HM. 2003. Developmental regulation of the growth plate. Nature 423:332–336.

Krovitz G. 2000. Three-dimensional comparisons of craniofacial morphology and growth patterns in neanderthals and modern humans.

Kuettner KE, Pauli BU, and Hall BK. 1983. Vascularity of cartilage. In: Cartilage. Vol. 1. New York, NY: Academic Press. p 281–312.

Lahr MM. 1996. The evolution of modern human diversity: a study of cranial variation. Cambridge, UK: Cambridge University Press.

Lambert JE, Chapman CA, Wrangham RW, and Conklin-Brittain NL. 2004. Hardness of cercopithecine foods: implications for the critical function of enamel thickness in exploiting fallback foods. American Journal of Physical Anthropology 125:363–368.

Lana-Elola E, Rice R, Grigoriadis AE, and Rice DPC. 2007. Cell fate specification during calvarial bone and suture development. Developmental Biology 311:335–346.

Langer K. 1877. Über die blutgefasse der knochen des schädeldaches und der harten hirnhaut. Denkschr K K Akad Wiss Wien 37:217–240.

Larina IV, Syed SH, Sudheendran N, Overbeek PA, Dickinson ME, and Larin KV. 2012. Optical coherence tomography for live phenotypic analysis of embryonic ocular structures in mouse models. Journal of Biomedical Optics 17:081410 1–4.

Le Lièvre CS, and Le Douarin N. 1975. Mesenchymal derivatives of the neural crest: analysis of chimaeric quail and chick embryos. Journal of Embryology and Experimental Morphology 34:125–154.

Leigh SR. 2004. Brain growth, life history, and cognition in primate and human evolution. American Journal of Primatology 62:139–164.

Lele S, and Richtsmeier JT. 1991. Euclidean distance matrix analysis: a coordinate-free approach for comparing biological shapes using landmark data. American Journal of Physical Anthropology 86:415–427.

Levin M, Ewald AJ, McMahon M, Werb Z, and Mostov K. 2007. A model of intussusceptive angiogenesis. In: Chadwick DJ, Goode J, editors. Vascular Development. Chichster, UK: John Wiley and Sons. p 37–45.

Lewinson D, and Silbermann M. 1992. Chondroclasts and endothelial cells collaborate in the process of cartilage resorption. The Anatomical Record 233:504–514.

Li L, Maslov K, Ku G, and Wang LV. 2009. Three-dimensional combined photoacoustic and optical coherence microscopy for in vivo microcirculation studies. Optics Express 17:16450–16455.

Lieberman DE, Hallgrímsson B, Liu W, Parsons TE, and Jamniczky HA. 2008. Spatial packing, cranial base angulation, and craniofacial shape variation in the mammalian skull: testing a new model using mice. Journal of Anatomy 212:720–735.

Lieberman DE, McBratney BM, and Krovitz G. 2002. The evolution and development of cranial form in *Homo sapiens*. Proceedings of the National Academy of Science 99:1134–1139.

Lieberman DE, Ross CF, and Ravosa MJ. 2000. The primate cranial base: ontogeny, function, and integration. American Journal of Physical Anthropology 113:117–169.

Lieberman DE. 2008. Some speculations about the selective basis for modern human craniofacial form. Evol Anthropol 17:55–68.

Liu Y, Tang Z, Kundu RK, Wu L, Luo W, Zhu D, Sangiorgi F, Snead ML, and Maxson Jr RE. 1999. Msx2 Gene Dosage Influences the Number of Proliferative Osteogenic Cells in Growth Centers of the Developing Murine Skull: A Possible Mechanism for MSX2-Mediated Craniosynostosis in Humans. Developmental Biology 205:206–274.

Liu Z, Lavine KJ, Hung IH, and Ornitz DM. 2007. FGF18 is required for early chondrocyte proliferation, hypertrophy and vascular invasion of the growth plate. Developmental biology 302:80–91.

Lovejoy CO, McCollum MA, Reno PL, and Rosenman BA. 2003. Developmental Biology and Human Evolution. Annual Review of Anthropology 32:85–109.

Mackie E, Ahmed Y, Tatarczuch L, Chen KS, and Mirams M. 2008. Endochondral ossification: how cartilage is converted into bone in the developing skeleton. The international journal of biochemistry & cell biology 40:46–62.

Mackie EJ, Tatarczuch L, and Mirams M. 2011. The skeleton: a multi-functional complex organ. The growth plate chondrocyte and endochondral ossification. Journal of Endocrinology 211:109–121.

MacLarnon AM, and Hewitt GP. 1999. The evolution of human speech: The role of enhanced breathing control. American Journal of Physical Anthropology 109:341–363.

Marks SC, and Odgren PR. 2002. Structure and development of the skeleton. In: Bilezikian JP, Raisz LG, Rodan GA, editors. Principles of bone biology. San Diego: Academic Press. p 3–16.

Martínez-Abadías N, Motch SM, Pankratz TL, Wang Y, Aldridge K, Jabs EW, and Richtsmeier JT. 2013. Tissue-specific responses to aberrant FGF signaling in complex head phenotypes. Developmental Dynamics 242:8094.

Martínez-Abadías N, Paschetta C, De Azevedo S, Esparza M, and González-José R. 2009. Developmental and genetic constraints on neurocranial globularity: insights from analyses of deformed skulls and quantitative genetics. Evolutionary Biology 36:37–56.

Martínez-Abadías N, Percival C, Aldridge K, Hill C, Ryan T, Sirivunnabood S, Wang Y, Jabs E, and Richtsmeier J. 2010. Beyond the closed suture in Apert mouse models: evidence of primary effects of FGFR2 signaling on facial shape at P0. Developmental Dynamics 239:3058–3071.

Maslov K, Zhang HF, Hu S, and Wang LV. 2008. Optical-resolution photoacoustic microscopy for in vivo imaging of single capillaries. Optics Letters 33:929–931.

Matsumoto T, Kawamoto A, Kuroda R, Ishikawa M, Mifune Y, Iwasaki H, Miwa M, Horii M, Hayashi S, Oyamada A, et al. 2006. Therapeutic potential of vasculogenesis and osteogenesis promoted by peripheral blood CD34-positive cells for functional bone healing. The American journal of pathology 169:1440–1457.

McBratney-Owen B, Iseki S, Bamforth SD, Olsen BR, and Morriss-Kay GM. 2008. Development and tissue origins of the mammalian cranial base. Developmental Biology 322:121–132.

Menegaz RA, Sublett SV, Figueroa SD, Hoffman TJ, Ravosa MJ, and Aldridge K. 2010. Evidence for the influence of diet on cranial form and robusticity. The Anatomical Record: Advances in Integrative Anatomy and Evolutionary Biology 293:630–641.

Merrill AE, Bochukova EG, Brugger SM, Ishii M, Pilz DT, Wall SA, Lyons KM, Wilkie AOM, and Maxson Jr RE. 2006. Cell mixing at a neural crest-mesoderm boundary and deficient ephrin-Eph signaling in the pathogenesis of craniosynostosis. Human molecular genetics 15:1319–1328.

Mitteroecker P, Bookstein F, and Badyaev A. 2008. The evolutionary role of modularity and integration in the hominoid cranium. Evolution 62:943–958.

Morriss-Kay GM, and Wilkie AOM. 2005. Growth of the normal skull vault and its alteration in craniosynostosis: insights from human genetics and experimental studies. Journal of Anatomy 207:637–653.

Motch SM, Pankratz T, Percival CJ, Jabs EW, and Richtsmeier JT. 2012. Development of the skull in Fgfr2+/P253R and Fgfr2+/S252W mouse models for Apert syndrome in late embryogenesis.
Murray PDF. 1985. Bones: a study of the development and structure of the vertebrate skeleton. Cambridge, UK: Cambridge University Press.
Nagata M, Nuckolls GH, Wang X, Shum L, Seki Y, Kawase T, Takahashi K, Nonaka K, Takahashi I, Noman AA, et al. 2011. The primary site of the acrocephalic feature in Apert syndrome is a dwarf cranial base with accelerated chondrocytic differentiation due to aberrant activation of the FGFR2 signaling. Bone 48:847–856.
Nakamura H, Yukita A, Ninomiya T, Hosoya A, Hiraga T, and Ozawa H. 2010. Localization of Thy-1–positive cells in the perichondrium during endochondral ossification. Journal of Histochemistry & Cytochemistry 58:455–462.
Nakamura T, Mochizuki Y, Kanetake H, and Kanda S. 2001. Signals via FGF receptor 2 regulate migration of endothelial cells. Biochemical and biophysical research communications 289:801–806.
Noden DM, and Trainor PA. 2005. Relations and interactions between cranial mesoderm and neural crest populations. Journal of anatomy 207:575–601.
Nuzzo S, Peyrin F, Martin-Badosa E, Lafage-Proust MH, and Boivin G. 2000. Assessment of bone mineral content from 3D synchrotron radiation microtomography images. In: Nuclear Science Symposium Conference Record, 2000 IEEE. Vol. 3. . p 19–2.
Olson EC, and Miller RL. 1958. Morphological Integration.
Opperman LA, and Rawlins JT. 2005. The Extracellular Matrix Environment in Suture Morphogenesis and Growth. Cells Tissues Organs 181:127–135.
Opperman LA. 2000. Cranial sutures as intramembranous bone growth sites. Developmental Dynamics 219:472–485.
Ornitz DM, and Marie PJ. 2002. FGF signaling pathways in endochondral and intramembranous bone development and human genetic disease. Genes & Development 16:1446–1465.
Ornitz DM, Xu J, Colvin JS, McEwen DG, MacArthur CA, Coulier F, Gao G, and Goldfarb M. 1996. Receptor specificity of the fibroblast growth factor family. Journal of Biological Chemistry 271:15292–15297.
Orr-Urtreger A, Bedford MT, Burakova T, Arman E, Zimmer Y, Yayon A, Givol D, and Lonai P. 1993. Developmental localization of the splicing alternatives of fibroblast growth factor receptor-2 (FGFR2). Developmental Biology 158:475–486.
Parfitt A. 2000. The mechanism of coupling: a role for the vasculature. Bone 26:319–323.
Parfitt A. 2001. The bone remodeling compartment: a circulatory function for bone lining cells. Journal of Bone and Mineral Research 16:1583–1585.
Passos-Bueno MR, Sertié AL, Jehee FS, Fanganiello R, and Yeh E. 2008. Genetics of craniosynostosis: genes, syndromes, mutations and genotype-phenotype correlations. In: Rice DP, editor. Craniofacial sutures: development, disease and treatment. Vol. 12. Basel: Karger. p 107–143.
Paxinos G, Halliday G, Watson C, Koutcherov Y, and Wang H. 2007. Atlas of the Developing Mouse Brain: At E17. 5, PO, and P6. 1st ed. London, UK: Academic Pr.
Percival C, and Richtsmeier JT. 2011. The epigenetics of dysmorphology: Craniosynostosis as an example. In: Hallgrímsson B, Hall BK, editors. Epigenetics: linking genotype and phenotype in development and evolution. San Fransisco: University of California Press.
Percival CJ, Wang Y, Zhou X, Jabs EW, and Richtsmeier JT. 2012. The effect of a Beare-Stevenson syndrome Fgfr2 Y394C mutation on early craniofacial bone volume and relative bone mineral density in mice. Journal of Anatomy 221:434–442.
Pitris C, Saunders KT, Fujimoto JG, and Brezinski ME. 2001. High-resolution imaging of the middle ear with optical coherence tomography: a feasibility study. Archives of Otolaryngology—Head & Neck Surgery 127:637–642.

Plavcan JM. 2001. Sexual dimorphism in primate evolution. American Journal of Physical Anthropology 116:25–53.
Ponce de León MS, and Zollikofer CPE. 2001. Neanderthal cranial ontogeny and its implications for late hominid diversity. Nature 412:534–538.
Popesko P, Rajtová V, and Horák J. 1992. The Colour Atlas of Anatomy of Small Laboratory Animals. London, UK: Saunders.
Pugh CW, and Ratcliffe PJ. 2003. Regulation of angiogenesis by hypoxia: role of the HIF system. Nature medicine 9:677–684.
R Developmental Core Team. 2008. R: A language and environment for statistical computing. Vienna, Austria: R Foundation for Statistical Computing. Available from: http://www.R-project.org
Raff RA. 1996. The shape of life: genes, development, and the evolution of animal form. Chicago, IL: University of Chicago Press.
Ramsay JO, Hooker G, and Graves S. 2009. Functional Data Analysis with R and MATLAB. New York, NY: Springer.
Rao B, Li L, Maslov K, and Wang L. 2010. Hybrid-scanning optical-resolution photoacoustic microscopy for in vivo vasculature imaging. Optics letters 35:1521–1523.
Ravosa MJ, Lopez EK, Menegaz RA, Stock SR, Stack MS, and Hamrick MW. 2008. Adaptive plasticity in the mammalian masticatory complex: you are what, and how, you eat. In: Vinyard CJ, Ravosa MJ, Wall CE, editors. Primate Craniofacial Function and Biology. Developments in Primatology: Progress and Prospects. New York, NY: Springer. p 293–328.
Ravosa MJ, Noble VE, Hylander WL, Johnson KR, and Kowalski EM. 2000. Masticatory stress, orbital orientation and the evolution of the primate postorbital bar. Journal of Human Evolution 38:667–693.
Reeves RH, Baxter LL, and Richtsmeier JT. 2001. Too much of a good thing: mechanisms of gene action in Down syndrome. TRENDS in Genetics 17:83–88.
Reno PL, McCollum MA, Cohn MJ, Meindl RS, Hamrick M, and Lovejoy CO. 2008. Patterns of correlation and covariation of anthropoid distal forelimb segments correspond to Hoxd expression territories. Journal of Experimental Zoology (Mol Dev Evol) 310:240–258.
Rice D, Aberg T, Chan Y, Tang Z, Kettunen PJ, Pakarinen L, Maxson R, and Thesleff I. 2000. Integration of FGF and TWIST in calvarial bone and suture development. Development 127:1845–1855.
Rice R, Rice DPC, Olsen BR, and Thesleff I. 2003. Progression of calvarial bone development requires Foxc1 regulation of Msx2 and Alx4. Developmental Biology 262:75–87.
Richtsmeier JT, Aldridge K, DeLeon VB, Panchal J, Kane AA, Marsh JL, Yan P, and Cole III TM. 2006. Phenotypic integration of neurocranium and brain. Journal of Experimental Zoology. Part B, Molecular and Developmental Evolution 306:360–378.
Richtsmeier JT, and Walker A. 1993. A morphometric study of facial growth. The Nariokotome *Homo erectus* skeleton. Cambridge, MA: Harvard University Press. p:391–410.
Richtsmeier JT, Paik CH, Elfert PC, Cole III TM, and Dahlman HR. 1995. Precision, repeatability, and validation of the localization of cranial landmarks using computed tomography scans. Cleft Palate Craniofacial Journal 32:217–217.
Robinson ML. 2006. An essential role for FGF receptor signaling in lens development. In: Seminars in cell & developmental biology. Vol. 17. . p 726–740.
Robson SL, and Wood B. 2008. Hominin life history: reconstruction and evolution. Journal of Anatomy 212:394–425.
Roseman CC, Kenny-Hunt JP, and Cheverud JM. 2009. Phenotypic integration without modularity: testing hypotheses about the distribution of pleiotropic quantitative trait loci in a continuous space. Evolutionary Biology 36:282–291.

Ross CF, and Ravosa MJ. 1993. Basicranial flexion, relative brain size, and facial kyphosis in nonhuman primates. American Journal of Physical Anthropology 91:305–305.

Ross CF. 1995. Allometric and functional influences on primate orbit orientation and the origins of the Anthropoidea. Journal of Human Evolution 29:201–227.

Rowbotham G, and Little E. 1965. New concepts on the aetiology and vascularization of meningiomata; the mechanisms of migraine; the chemical processes of the cerebrospinal fluid; and the formation of collections of blood or fluid in the subdural space. British Journal of Surgery 52:21–24.

Saadeh PB, Mehrara BJ, Steinbrech DS, Spector JA, Greenwald JA, Chin GS, Ueno H, Gittes GK, and Longaker MT. 2000. Mechanisms of fibroblast growth factor-2 modulation of vascular endothelial growth factor expression by osteoblastic cells. Endocrinology 141:2075–2083.

Saarimäki-Vire J, Peltopuro P, Lahti L, Naserke T, Blak AA, Weisenhorn DMV, Yu K, Ornitz DM, Wurst W, and Partanen J. 2007. Fibroblast growth factor receptors cooperate to regulate neural progenitor properties in the developing midbrain and hindbrain. The Journal of Neuroscience 27:8581–8592.

Schatz O, Golenser E, and Ben-Arie N. 2005. Clearing and photography of whole mount X-gal stained mouse embryos. BioTechniques 39:650–656.

Schindelin J, Arganda-Carreras I, Frise E, Kaynig V, Longair M, Pietzsch T, Preibisch S, Rueden C, Saalfeld S, Schmid B, et al. 2012. Fiji: an open-source platform for biological-image analysis. Nature Methods 9:676–682.

Schipani E, Lanske B, Hunzelman J, Luz A, Kovacs C, Lee K, Pirro A, Kronenberg H, and Jüppner H. 1997. Targeted expression of constitutively active receptors for parathyroid hormone and parathyroid hormone-related peptide delays endochondral bone formation and rescues mice that lack parathyroid hormone-related peptide. Proceedings of the National Academy of Sciences 94:13689.

Schneider CA, Rasband WS, and Eliceiri KW. 2012. NIH Image to ImageJ: 25 years of image analysis. Nature Methods 9:671–675.

Schwartz JH, and Tattersall I. 2003. The Human Fossil Record: Craniodental morphology of genus Homo (Africa and Asia). John Wiley and Sons.

Serrat MA, King D, and Lovejoy CO. 2008. Temperature regulates limb length in homeotherms by directly modulating cartilage growth. Proceedings of the National Academy of Sciences 105:19348–19353.

Shapiro IM, Golub EE, Chance B, Piddington C, Oshima O, Tuncay OC, and Haselgrove JC. 1988. Linkage between energy status of perivascular cells and mineralization of the chick growth cartilage. Developmental Biology 129:372–379.

Sherwood CC, Subiaul F, and Zawidzki TW. 2008. A natural history of the human mind: tracing evolutionary changes in brain and cognition. Journal of Anatomy 212:426–454.

Shi DL, Launay C, Fromentoux V, Feige JJ, and Boucaut JC. 1994. Expression of fibroblast growth factor receptor-2 splice variants is developmentally and tissue-specifically regulated in the amphibian embryo. Developmental Biology 164:173–182.

Sims NA, Clément-Lacroix P, Da Ponte F, Bouali Y, Binart N, Moriggl R, Goffin V, Coschigano K, Gaillard-Kelly M, Kopchick J, et al. 2000. Bone homeostasis in growth hormone receptor-null mice is restored by IGF-I but independent of Stat5. Journal of Clinical Investigation 106:1095–1103.

Smith SL. 2004. Skeletal age, dental age, and the maturation of KNM-WT 15000. American Journal of Physical Anthropology 125:105–120.

Solursh M, Ahrens PB, and Reiter RS. 1978. A tissue culture analysis of the steps in limb chondrogenesis. In Vitro Cellular & Developmental Biology-Plant 14:51–61.

Sorescu GP, Sykes M, Weiss D, Platt MO, Saha A, Hwang J, Boyd N, Boo YC, Vega JD, Taylor WR, et al. 2003. Bone morphogenic protein 4 produced in endothelial cells by oscillatory shear stress stimulates an inflammatory response. Journal of Biological Chemistry 278:31128–31135.

Soriano P. 1999. Generalized lacZ expression with the ROSA26 Cre reporter strain. Nature Genetics 21:70–71.

Spoor F, Garland T, Krovitz G, Ryan TM, Silcox MT, and Walker A. 2007. The primate semicircular canal system and locomotion. Proceedings of the National Academy of Sciences 104:10808–10812.

Streeten EA, and Brandi ML. 1990. Biology of bone endothelial cells. Bone and mineral 10:85–94.

Suhardja A, and Hoffman H. 2003. Role of growth factors and their receptors in proliferation of microvascular endothelial cells. Microscopy research and technique 60:70–75.

Suwa G, Kono RT, Simpson SW, Asfaw B, Lovejoy CO, and White TD. 2009. Paleobiological implications of the Ardipithecus ramidus dentition. Science 326:69.

Syed SH, Larin KV, Dickinson ME, and Larina IV. 2011. Optical coherence tomography for high-resolution imaging of mouse development in utero. Journal of Biomedical Optics 16:046004 1–6.

Takai S, Tokuda H, Hanai Y, Harada A, Yasuda E, Matsushima-Nishiwaki R, Kato H, Ogura S, Ohta T, and Kozawa O. 2007. Negative Regulation by p70 S6 Kinase of FGF-2–Stimulated VEGF Release Through Stress-Activated Protein Kinase/c-Jun N-Terminal Kinase in Osteoblasts. Journal of Bone and Mineral Research 22:337–346.

Takimoto A, Nishizaki Y, Hiraki Y, and Shukunami C. 2009. Differential actions of VEGF-A isoforms on perichondrial angiogenesis during endochondral bone formation. Developmental Biology 332:196–211.

Tavares ALP, Garcia EL, Kuhn K, Woods CM, Williams T, and Clouthier DE. 2012. Ectodermal-derived Endothelin1 is required for patterning the distal and intermediate domains of the mouse mandibular arch. Developmental Biology.

Thiriet M. 2008. Biology and Mechanics of Blood Flows. Springer.

Thoma R. 1913. Untersuchungen über das schädelwachstum und seine störungen. 2. Das fetale wachstum. Virchows Archiv für pathologische Anatomie und Physiologie und für klinische Medizin 212:1.

Thompson TJ, Owens PD, and Wilson DJ. 1989. Intramembranous osteogenesis and angiogenesis in the chick embryo. J Anat 166:55–65.

Tillier AM. 1995. Neanderthal ontogeny: A new source for critical analysis. Anthropologie 33:63–68.

Ting M-C, Wu NL, Roybal PG, Sun J, Liu L, Yen Y, and Maxson RE. 2009. EphA4 as an effector of Twist1 in the guidance of osteogenic precursor cells during calvarial bone growth and in craniosynostosis. Development 136:855–864.

Towler DA. 2008. Vascular Endothelial Growth Factor and Osteogenic-Angiogenic Coupling. In: Bilezikian JP, Raisz LG, Martin TJ, editors. Principles of Bone Biology. Vol. 2. 3rd ed. Academic Press. p 1133–1144.

Trueb B. 2011. Biology of FGFRL1, the fifth fibroblast growth factor receptor. Cellular and Molecular Life Sciences 68:951–964.

Trueta J. 1963. The role of the vessels in osteogenesis. Journal of Bone and Joint Surgery-British Volume 45:402–418.

Usami K, Mizuno H, Okada K, Narita Y, Aoki M, Kondo T, Mizuno D, Mase J, Nishiguchi H, Kagami H, et al. 2009. Composite implantation of mesenchymal stem cells with endothelial progenitor cells enhances tissue-engineered bone formation. Journal of Biomedical Materials Research Part A 90:730–741.

Vivatbutsiri P, Ichinose S, Hytönen M, Sainio K, Eto K, and Iseki S. 2008. Impaired meningeal development in association with apical expansion of calvarial bone osteogenesis in the Foxc1 mutant. Journal of Anatomy 212:603–611.

Von Schroeder H, Veillette C, Payandeh J, Qureshi A, and Heersche J. 2003. Endothelin-1 promotes osteoprogenitor proliferation and differentiation in fetal rat calvarial cell cultures. Bone 33:673–684.

Wang Y, Sun M, Uhlhorn VL, Zhou X, Peter I, Martinez-Abadias N, Hill CA, Percival C, Richtsmeier JT, Huso DL, et al. 2010. Activation of p38 MAPK pathway in the skull abnormalities of Apert syndrome Fgfr2+/P253R mice. BMC Developmental Biology 10:20 pages long (pdf download).

Wang Y, Wan C, Deng L, Liu X, Cao X, Gilbert SR, Bouxsein ML, Faugere M, Guldberg RE, Gerstenfeld LC, et al. 2007. The hypoxia-inducible factor alpha pathway couples angiogenesis to osteogenesis during skeletal development. Journal of Clinical Investigation 117:1616–1626.

Wang Y, Xiao R, Yang F, Karim BO, Iacovelli AJ, Cai J, Lerner CP, Richtsmeier JT, Leszl JM, and Hill CA. 2005. Abnormalities in cartilage and bone development in the Apert syndrome FGFR2+/S252W mouse. Development 132:3537–3548.

Warburton D, Schwarz M, Tefft D, Flores-Delgado G, Anderson KD, and Cardoso WV. 2000. The molecular basis of lung morphogenesis. Mechanisms of development 92:55–82.

Weaver TD. 2009. The meaning of Neandertal skeletal morphology. Proceedings of the National Academy of Sciences 106:16028–16033.

Werner S, Duan D, De Vries C, Peters K, Johnson D, and Williams L. 1992. Differential splicing in the extracellular region of fibroblast growth factor receptor 1 generates receptor variants with different ligand-binding specificities. Molecular and cellular biology 12:82–88.

Wilkie AO. 1997. Craniosynostosis: genes and mechanisms. Human molecular genetics 6:1647–1656.

Xu X, Weinstein M, Li C, and Deng CX. 1999. Fibroblast growth factor receptors (FGFRs) and their roles in limb development. Cell and tissue research 296:33–43.

Yamaguchi A, Komori T, and Suda T. 2000. Regulation of osteoblast differentiation mediated by bone morphogenetic proteins, hedgehogs, and Cbfa1. Endocrine Reviews 21:393–411.

Yin L, Du X, Li C, Xu X, Chen Z, Su N, Zhao L, Qi H, Li F, and Xue J. 2008. A Pro253Arg mutation in fibroblast growth factor receptor 2 (Fgfr2) causes skeleton malformation mimicking human Apert syndrome by affecting both chondrogenesis and osteogenesis. Bone.

Yin M, and Pacifici M. 2001. Vascular regression is required for mesenchymal condensation and chondrogenesis in the developing limb. Developmental Dynamics 222:522–533.

Yoshida T, Vivatbutsiri P, Morriss-Kay G, Saga Y, and Iseki S. 2008. Cell lineage in mammalian craniofacial mesenchyme. Mechanisms of Development 125:797–808.

Young NM, and Devlin MJ. 2012. Finding our inner animal: Understanding human evolutionary variation via experimental model systems.

Yu JC, Lucas JH, Fryberg K, and Borke JL. 2001. Extrinsic tension results in FGF-2 release, membrane permeability change, and intracellular Ca++ increase in immature cranial sutures. Journal of Craniofacial Surgery 12:391–398.

Yu K, Herr AB, Waksman G, and Ornitz DM. 2000. Loss of fibroblast growth factor receptor 2 ligand-binding specificity in Apert syndrome. Proceedings of the National Academy of Science 97:14536–14541.

Zelzer E, and Olsen BR. 2004. Multiple roles of vascular endothelial growth factor (VEGF) in skeletal development, growth, and repair. Current topics in developmental biology 65:169–187.

Zelzer E, McLean W, Ng YS, Fukai N, Reginato AM, Lovejoy S, D'Amore PA, and Olsen BR. 2002. Skeletal defects in VEGF120/120 mice reveal multiple roles for VEGF in skeletogenesis. Development 129:1893–1904.

Zernik J, Twarog K, and Upholt WB. 1990. Regulation of alkaline phosphatase and alpha2 (I) procollagen synthesis during early intramembranous bone formation in the rat mandible. Differentiation 44:207–215.

Zhang HF, Maslov K, Stoica G, and Wang LV. 2006. Functional photoacoustic microscopy for high-resolution and noninvasive in vivo imaging. Nature Biotechnology 24:848–851.

Zollikofer CPE, and Ponce de León MS. 2010. The evolution of hominin ontogenies. Seminars in Cell & Developmental Biology 21:441–452.

Zumpano MP, and Richtsmeier JT. 2003. Growth-related shape changes in the fetal craniofacial complex of humans (*Homo sapiens*) and pigtailed macaques (*Macaca nemestrina*): a 3D-CT comparative analysis. American Journal of Physical Anthropology 120:339–351.

VITA: CHRISTOPHER J. PERCIVAL

Education

PhD 2013, The Pennsylvania State University, Anthropology
M.A. 2009, The Pennsylvania State University, Anthropology
B.S. 2006, Rutgers College, Rutgers University, Evolutionary Anthropology

Areas of Interest

Craniofacial Development and Evolution, Intramembranous Ossification, Evolutionary Developmental Biology, 3D Imaging and Analysis, Skeletal Phenotype Quantification

Publications

2012 Percival CJ, Wang Y, Zhou X, Jabs EW, Richtsmeier JT, The effect of a Beare-Stevenson Syndrome Fgfr2 Y394C mutation on early craniofacial bone volume and relative bone mineral density in mice, Journal of Anatomy. 221:434-442.

2012 Wang Y, Zhou X, Oberoi K, Phelps R, Couwenhoven R, Sun M, Rezza A, Percival CJ, Friedenthal J, Krejci P, Richtsmeier JT, Huso DL, Rendl M, Jabs EW, p38 inhibition ameliorates skin and skull abnormalities in Fgfr2 Beare-Stevenson mice, Journal of Clinical Investigation. 122(6):2153-2164.

2011 Percival CJ, Richtsmeier JT, The epigenetics of dysmorphology: Craniosynostosis as an example. In: B. Hallgrímsson and B.K. Hall eds., Epigenetics: linking genotype and phenotype in development and evolution. San Francisco: University of California Press.

2011 Xia J, Guo Z, Maslov K, Aguirre A, Zhu Q, Percival C, Wang LV, Three-dimensional photoacoustic tomography based on the focal-line concept. Journal of Biomedical Optics. 16(9).

2010 Martínez-Abadías N, Percival C, Aldridge K, Hill C, Ryan T, Sirivunnabood S, Wang Y, Jabs E, Richtsmeier J, Beyond the closed suture in Apert mouse models: evidence of primary effects of FGFR2 signaling on facial shape at P0. Developmental Dynamics. 239:3058-3071.

2010 Wang Y, Sun M, Uhlhorn VL, Zhou X, Peter I, Martinez-Abadias N, Hill CA, Percival C, Richtsmeier JT, Huso DL, Jabs EW, Activation of p38 MAPK pathway in the skull abnormalities of Apert syndrome Fgfr2+/P253R mice. BMC Developmental Biology.

2010 Aldridge K, Hill CA, Austin JR, Percival C, Martinez-Abadias N, Neuberger T, Wang Y, Jabs EW, Richtsmeier JT, Brain phenotypes in two FGFR2 mouse models for Apert symdrome. Developmental Dynamics 239:987-997.

Honors and Awards

2013 Alumni Association Dissertation Award, Penn State Alumni Association
2011 genesis Excellence in Craniofacial Research Award (Student Poster award), Society of Craniofacial Genetics and Developmental Biology
2011 William S. Pollitzer Student Travel Award, American Association of Physical Anthropologists
2010 Matson-Benson Award, Anthropology Dept, Penn State University
2009 College of Liberal Arts Summer Scholarship, Penn State University
2006 Henry Rutgers Scholar with High Honors, Rutgers College Honors Thesis Program, Thesis: A Study of GIS Techniques in the Analysis of Ancient Environments at Koobi Fora
2006 Tuevo Airola Memorial Award in Environmental Geomatics, Center for Remote Sensing and Spatial Analysis, Rutgers University

Research Experience

2013-2008 Research Assistant, Richtsmeier Morphometrics Lab, Penn State University
2007-2006 Member, Richtsmeier Morphometrics Lab, Penn State University

For a full Vita, please contact the author via cjpercival@gmail.com